

ABSTRACT

Title of Document: **COMBINATORIAL EXPERIMENTS
USING A SPATIALLY PROGRAMMABLE
CHEMICAL VAPOR DEPOSITION
SYSTEM**

Ramaswamy Sreenivasan, Doctor of Philosophy,
2007

Directed By: Professor Raymond A. Adomaitis,
Department of Chemical and Biomolecular
Engineering

A CVD reactor concept featuring a segmented design allows individual regions of a wafer to be exposed to different precursor concentrations simultaneously during a run resulting in different thickness profiles on the wafer and a thickness gradient at the boundaries between segment regions. Different recipes were cycled through each of the segments in a sequence of deposition experiments to develop a model relating precursor concentration to film thickness in each segment region. As a demonstration of spatial programmability, the system was re-programmed using this model to produce uniform thickness amongst the segments; inter-segment uniformity approaching 0.48 % (thickness standard deviation) was demonstrated.

In a subsequent study, segmented CVD reactor designs enabling spatial control of across-wafer gas phase composition were evaluated for depositing graded films suitable for combinatorial studies. Specifically two reactor designs were evaluated with experiments and response surface model (RSM) based analysis to quantify the reactor performance in terms of film thickness uniformity, sensitivity to adjustable reactor operating conditions, range of thickness over which uniformity could be achieved and each reactor's ability to control the thickness gradient across the wafer surface. Design features distinguishing the two reactor systems and their influence on gradient control versus deposition rate performance are summarized. Response Surface (RS) models relating wafer state properties to process recipes are shown to be effective tools to quantify, qualify and compare different reactor designs.

COMBINATORIAL EXPERIMENTS USING A SPATIALLY PROGRAMMABLE
CHEMICAL VAPOR DEPOSITION SYSTEM

By

Ramaswamy Sreenivasan

Dissertation submitted to the Faculty of the Graduate School of the
University of Maryland, College Park, in partial fulfillment
of the requirements for the degree of
Doctor of Philosophy
2007

Advisory Committee:

Professor Raymond A. Adomaitis, Chair

Professor Panagiotis Dimitrakopoulos

Professor Theodosia Gougousi

Professor Gary W. Rubloff

Professor Evangelos Zafiriou

© Copyright by
Ramaswamy Sreenivasan
2007

Dedication

To my Father:

A perspicacious engineer with great hands-on skills (magical hands)

and

My Mother:

For her unconditional love and encouragement.

Acknowledgements

I am deeply grateful to Professor Raymond A. Adomaitis, my thesis advisor for his mentoring and guidance throughout my research here at UMD. It is from him I have certainly learnt a lot about the right attitude towards scientific research. His approach to breaking down any complex problem through systematic reductionism into its simple parts has helped me tremendously in tackling several issues during the course of my research. He has also greatly influenced my teaching and writing skills. I am also deeply thankful for his guidance in MATLAB numerical techniques and his MATLAB code which I used extensively for my simulations in this research.

I thank Dr. Gary Rubloff for his introducing me to the fascinating field of microelectronics when I came here for my master's degree and his continuing guidance during my Ph.D.

I thank Dr. Evangelhos Zafiriou for his valuable guidance in the field of process control in semiconductor manufacturing when I came here for my master's degree and his continuing guidance during my Ph.D. especially regarding model identification for the reactor used in this research work.

I would also like to acknowledge Mr. Russ Wood at the Physics Machine Shop for his expert guidance while machining parts that were important components to my research.

I thank all our research group members at LAMP: Laurent Henn-Lecordier, Erin Robertson, Parag Banerjee, Ernie Cleveland, Yuhong Cai and Wei Lei for their many insights and comments through out this research project.

Table of Contents

Dedication	ii
Acknowledgements	iii
Table of Contents	iv
List of Tables	vii
List of Figures.....	viii
Chapter 1: Introduction	1
1.1 Equipment Improvement and Innovation	1
1.2 Process Improvement and Innovation	3
1.3 Metrology Improvement and Innovation	3
1.4 Innovation at the Device Level	4
1.5 Combinatorial New Materials Research	5
1.6. Improvements in IT and Knowledge Management	6
Chapter 2: A Demonstration of Spatially Programmable Chemical Vapor Deposition: Model-Based Uniformity/Non-uniformity Control	8
2.1. Introduction.....	8
2.2. Conventional CVD reactor design:	8
2.3. Earlier work in design improvements:	9
2.4. Programmable reactor and showerhead design	12
2.4.1. Gas transport mechanisms	13
2.4.2. Modes of reactor operation	18

2.4.3. Prototype reactor experimental system	19
2.5. Demonstration of programmability	21
2.5.1. Wafer cleaning and reactor conditioning	21
2.5.2. Deliberate non-uniformity experiments for model building	22
2.5.3. Ex-situ metrology	24
2.5.4. Building a model between the W film thickness and the flow rate of H ₂	28
2.5.5. Inferences from the deliberate non-uniformity experiments	28
2.5.6. Reprogramming the process for uniformity	31
2.5.7. Inferences from the re-programmed uniformity experiments	33
2.5.8. Effect of showerhead-wafer gap size on programmability	37
2.6. Segment-to-segment interaction analysis in the programmable reactor	41
2.7. Chapter summary	44
Chapter 3: Demonstration of gradient control	46
3.1. Introduction	46
3.2. Modeling for design A	47
3.2.1. The response surface approach:	48
3.2.2. Derivation of the model form:	49
3.2.3. Data set to build RSM for design A:	52
3.2.4. RS model identification and validation for design A	54
3.3. Performance analysis for design A:	56
3.3.1. Sensitivity of film thickness profile to gas flow rate and gap:	56
3.3.2. Range of segment to segment uniformity	59
3.3.3. Gradient control performance	63

Chapter 4: The mini reactor (Design B)	70
4.1. Disadvantages of design A	70
4.2. Modeling for design B	73
4.2.1. Data set to build RSM for design A:	73
4.2.2. RS model identification and validation for design B	73
4.3. Performance analysis for design B:	76
4.3.1. Sensitivity to gap size	76
4.3.2. Range of segment to segment uniformity	76
4.3.3. Gradient control performance	79
Chapter 5: Conclusions and Future Work	92
5.1. Conclusions and inferences:	92
5.2. Future work	93
5.2.1. From an equipment perspective:	93
5.2.2. From a materials perspective:	94
5.2.2. From a process perspective:	94
5.2.3. Combinatorial ALD for nano-laminates and nano-composites:	99
Appendix A: Title of related online videos	103
Bibliography	104

List of Tables

Table 1: Recipes and results for deliberate non-uniformity experiments.	23
Table 2: Programmed uniformity results for W32 - W41	34
Table 3: Wafers 1 to 25 were used to deposit films from the above recipes (varying flow rates and showerhead-wafer gaps sizes) for generating the data to obtain the RS model for reactor design A. $WF_6:H_2$ flow ratio in each segment is 1:4. Ar flow in each segment is $60-(H_2 \text{ flow}+ WF_6 \text{ flow})$ sccm	53
Table 4: Wafers 1 to 28 were used to deposit films from the above recipes (varying flow rates and showerhead-wafer gaps sizes) for generating the data to obtain the RS model for deign B. $WF_6:H_2$ flow ratio in each segment is 1:4. Ar flow in each segment is $60-(H_2 \text{ flow}+ WF_6 \text{ flow})$ sccm	74
Table 5: Design A vs. Design B comparison table	90

List of Figures

Figure 1: Research endeavors in the semiconductor industry.	2
Figure 2: Conventional CVD vs. SP-CVD.	9
Figure 3: SP-CVD reactor at LAMP lab.	15
Figure 4: Gas delivery system for SP-CVD.	16
Figure 5: Schematic diagram of the SP-CVD reactor system.	17
Figure 6: The flow sheet illustration programmed non-uniformity and uniformity experiments.	19
Figure 7: Accurate interpretation of 4PP metrology data using a numerical quadrature technique.	24
Figure 8: Wafer profiles (deliberate Non-uniformity DOEs)	27
Figure 9: Plot showing linear models for each segment. The vertical error bars range from the minimum thickness to the maximum thickness obtained for that particular flow recipe (From Table1). The solid black line is the new set point. This line intersects the linear models and this point of intersection when projected on to the x axis gives us the new recipe (WF_6 and H_2 flowrates). The square markers denote the average thickness in each segment for wafers W32 to W41 processed using the segment-to-segment uniformity recipe.	30
Figure 10: This figure illustrates the three linear models in one plot. The horizontal error bars on the averaged uniform profiles under each segment represent the range of WF_6 flow rates that would have resulted in the same uniformity producing recipe	

needed for the set point of 660 nm, due to the 1sccm resolution of the mass flow controllers used to control the precursor mass flow rates..... 32

Figure 11: A plot of the programmed uniformity results shown in Table 2..... 35

Figure 12: Averaged profiles 36

Figure 13: 3mm vs. 1mm data: Linear models 39

Figure 14: Schematic of the SP-CVD reactor assembly 40

Figure 15: Sensitivity (nm/sccm H₂) with respect to H₂ flow to segment 1 (left), segment 2 (center), and segment 3 (right). 44

Figure 16: True wafer maps (data) of wafers No.6, No.8 and No.23 (Table 1), and averaged profiles of 10 wafers processed with the same recipe, obtained from 4 point probe measurements and numerically interpolated in MATLAB are shown in the top row. The interpolated data are compared to the maps predicted by the RS model shown in the second row. The third row compares the average thickness for each segment through bar charts. The recipe is written in the format:

$$\left[\sqrt{H_2 \text{ flow(sccm) in } S1}, \sqrt{H_2 \text{ flow(sccm) in } S2}, \sqrt{H_2 \text{ flow(sccm) in } S3} \quad \text{gap} \right]$$
..... 55

Figure 17: Sensitivity of the reactor to recipe and gap size as predicted by the RS model for design A. The greater the redness of the plot within a segment, the more sensitive that segment is to H₂ flow in that segment. As gap size increases, sensitivity to H₂ flow decreases because with increasing gap, the precursor gases ‘escape’ into the external volume of the chamber..... 58

Figure 18: The range of uniformity control possible for the design A as predicted by the RS model. This plot conveys that this reactor design could be used to deposit uniform films ranging from 0 to 800 nm using gap sizes ranging from 0 to 3 mm, with

WF₆ flow rates ranging from 0 to 12 sccm in each segment (limited by the MFCs) and H₂ flow rates in each segment ranging from 0 to 48 sccm (to maintain the stoichiometric ratio of 1:4 WF₆:H₂). Ar flow in each segment is 60-(H₂ flow+ WF₆flow) sccm. 62

Figure 19: Gradient control for design A for three cases of δ_m values (-1, 0 and 1). The value of the minimized objective function O_v at the end of the optimization routine is shown below the plots in each case. W_{avg} , W_m and O_v in nm. 66

Figure 20: Evaluation of gradient control across segments 1 and 3 as a function of δ_m using the RS model for design A. 69

Figure 21: Schematic front view of Design B and photograph of bottom view of mini reactor lid. When the segments are lowered, the lid is stopped by the wall of the mini chamber while the segments continue to be lowered to the desired segment-wafer gap. This design renders a chamber with a reduced volume and overcomes drawbacks of design A..... 72

Figure 22: True wafer maps (data) of wafers No.2, No.11, No.13 and No.22 (Table 2), obtained from 4 point probe measurements and numerically interpolated in MATLAB are shown in the top row. They are compared with the predicted maps by the RS model for the same shown in the second row. The third row compares the average thickness for each segment through bar charts. The recipe is written in the format:

$[\sqrt{H_2 \text{ flow(sccm) in } S1}, \sqrt{H_2 \text{ flow(sccm) in } S2}, \sqrt{H_2 \text{ flow(sccm) in } S3} \text{ gap}]$ 75

Figure 23: Sensitivity of the reactor to recipe and gap size as predicted by the RS model for design B. The greater the redness of the plot of the plot within a segment the more sensitive that segment is to H₂ flow in that segment. As gap size increases,

sensitivity to H₂ flow does not decrease as in design A because the mini reactor design minimizes the gases escaping into the larger chamber volume..... 77

Figure 24: The range of uniformity control possible for the design A vs. design B as predicted by the RS model. This plot indicates that design B could be used to deposit uniform films ranging from 0 to 1800 nm using gap sizes ranging from 0 to 2.5 mm, with WF₆ flow rates ranging from 0 to 12 sccm in each segment (limited by the MFCs) and H₂ flow rates in each segment ranging from 0 to 48 sccm (to maintain the stoichiometric ratio of 1:4 WF₆:H₂). Ar flow in each segment is 60-(H₂ flow+ WF₆flow) sccm. 78

Figure 25 Gradient control for design B for three cases of δ_m values (-1, 0 and 1). The value of the minimized objective function O_v at the end of the optimization routine is shown below the plots in each case. W_{avg} , W_m and O_v in nm. 80

Figure 26: Evaluation of gradient control across segments 1 and 3 as a function of δ_m using the RS model for design B. 81

Figure 27: Design A vs. Design B Comparison for $W_m = 200$ nm and $W_{avg} = 300$ nm. 82

Figure 28: Design A vs. Design B Comparison for $W_m = 200$ nm and $W_{avg} = 700$ nm. 83

Figure 29: Design A vs. Design B Comparison for $W_m = 300$ nm and $W_{avg} = 300$ nm. 84

Figure 30: Design A vs. Design B Comparison for $W_m = 300$ nm and $W_{avg} = 700$ nm. 85

Figure 31: Design A vs. Design B Comparison for $W_m = 500$ nm and $W_{avg} = 700$ nm.	86
Figure 32: Design A vs. Design B Comparison for $W_m = 700$ nm and $W_{avg} = 700$ nm.	87
Figure 33: Design A vs. Design B Comparison for $W_m = 500$ nm and $W_{avg} = 2000$ nm.	88
Figure 34: Design A vs. Design B Comparison for $W_m = 1500$ nm and $W_{avg} = 2000$ nm.	89
Figure 35: An example of combinatorial ALD.....	96
Figure 36: Combinatorial CVD/ALD strategies.	98

Chapter 1: Introduction

Moore's law is a mantra in the semiconductor industry that needs no introduction. Any attempt here to mention the law and its inferences and implications in the next decade would be redundant. There are plenty of pertinent references which discuss this insightful prognostication [1]. The question that one needs to address is "How are we going to keep up with it over the next decade and maybe even later?" Looking at the goals laid down by the ITRS [2] (International Technology Roadmap for Semiconductors), it is tempting to come up with a simplified overview depicted in Figure 1 that mentions the endeavors that the industry, universities and other research institutions are actively pursuing worldwide to keep up with the targets laid down by the ITRS and overcome bottlenecks like lithography resolution limits, gate oxide tunneling effects (that limits transistor scaling) etc. It is important to keep in mind that Moore's law will be effective only if the cost per component (be it DRAM, SRAM, Microprocessor or ASIC) manufactured at every subsequent technology node continues to drop. It is worthwhile to look at these directions of research in a little greater detail for a more complete introduction to the reader of this thesis.

1.1 Equipment Improvement and Innovation

This effort entails research efforts to improve scalability, extendibility, throughput, Mean time to repair (MTTR), Mean Time Between Failures (MTBF), tool reproducibility, ease of integration, Cost of Ownership (COO) etc of equipment as we move from one technology node to the next. This area would benefit from advances

in the field of MEMS and NEMS as both these research areas focus on miniaturization of actuators, mass flow controllers, valves, heaters which are all very critical in semiconductor equipment [3]. Our research group would like to add the concept of “programmability” as an important contributing factor to this research subset. The experiments discussed in this research address this topic.

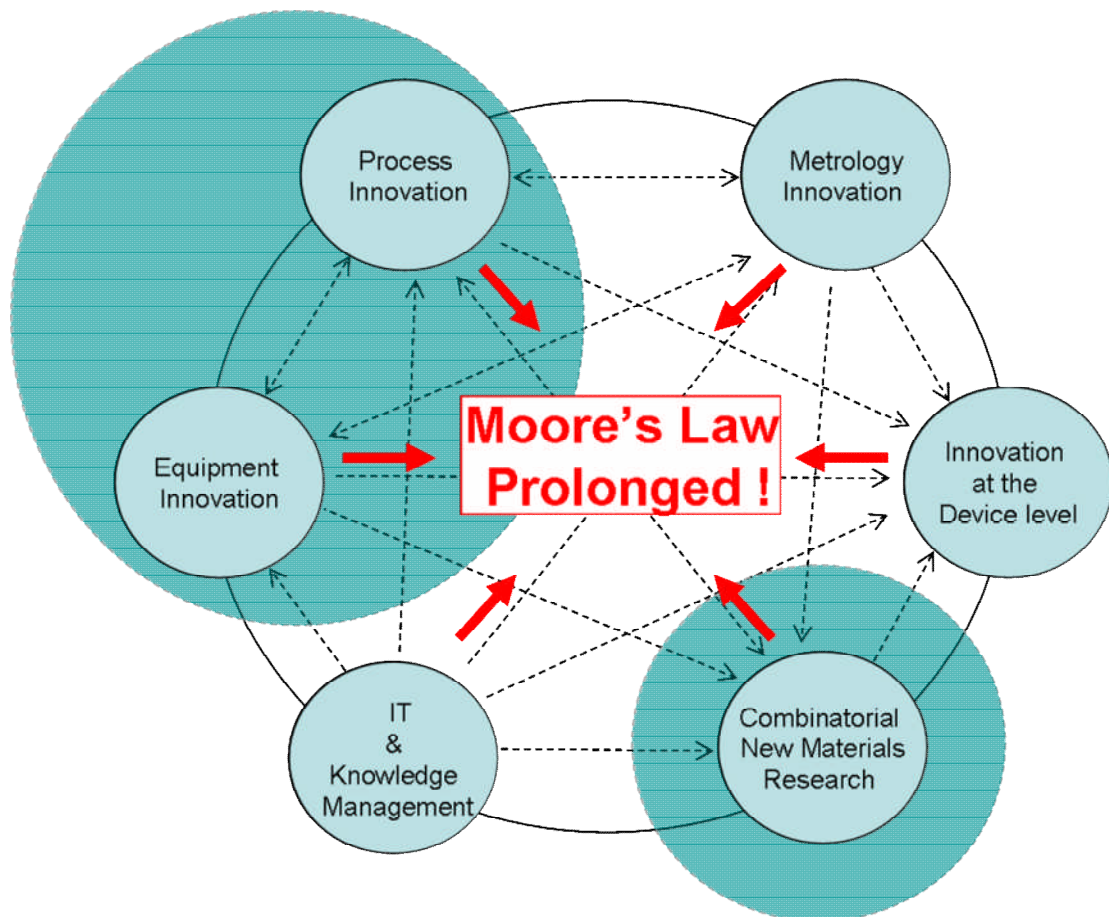


Figure 1: Research endeavors in the semiconductor industry.

1.2 Process Improvement and Innovation

This research effort entails new process innovation; e.g. the recent come back of ALD [4], new recipe identification and optimization, uniformity of wafer state properties, postulating new process theory explaining the process, using this theory for multi scale modeling (first principal and empirical or a combination of both), performing Design of Experiments (DOEs) for model identification, parameter estimation and experimentation to validate and update models and exploiting the model's predictive capabilities to refine the recipe over time. Advanced Process Control (APC) techniques [5] keep the process variables (which can be measured: this is where metrology efforts pitch in) at set point and accelerate the process development cycle and yield learning. The fields of modeling and APC [5] deserve a whole new research subset to itself, but it is included under this research endeavor because the upshot of APC is process improvement. Improvements in contamination control that reduce defects are also included in this research category. Process programmability, a consequence of equipment programmability mentioned above would render the process development cycle several advantages in improving process performance and yield.

1.3 Metrology Improvement and Innovation

As devices get smaller and component density increases it becomes more difficult to measure the physical dimensions of the components ex-situ or in-situ [3]. Research

efforts are underway to implement existing metrology in-situ wherever possible as this facilitates real time measurement, fault detection, end pointing and APC for contamination control and process variable set point tracking. New sensing technologies are being looked into for film property measurement, fault detection, defect measurement etc. [6]. Robustness to process variations and corrosive agents, repeatability, reproducibility, and accuracy through well defined metrics relating the measured property to the wafer state property etc need constant improvement. This research area would also benefit from advances in the field of MEMS and NEMS as sensor size must be reduced and sensors must be integrated with the process tool.

1.4 Innovation at the Device Level

This research effort entails improvements in transistor design and scaling, and ensuring that the interconnect design keeps up with the device scaling. Efforts to improvements in device operation are also being carried out (for example it has been proven operating transistors at lower temperatures can eke out a better performance etc [4]). Device design and quantum mechanics form the foundation for this endeavor as these research topics address the flow of electrons within devices. As we scale down even further, defects and interfaces start having a prominent effect on device operation and understanding the impact of these atomic scale features on mobility and other device characteristics is paramount.

1.5 Combinatorial New Materials Research

It is inevitable that the current materials will fail at smaller nodes; for example SiO_2 fails as a gate dielectric at 50nm nodes and lower as its thickness to provide the necessary capacitance is so small that electrons tunnel through it making the device unusable ([1],[3]). One way to circumvent this problem is to use a thicker film of a material with a higher dielectric constant so that we can still extract the same capacitance from the gate dielectric ($C=kA/d$). Hence there is a quest for new high K dielectrics. Both Intel and IBM have committed to manufacturing hafnium based high K dielectrics and metal electrodes for the 45nm generation [7]. Similarly there are efforts for finding new low k materials for Inter Layer Dielectrics (ILD), new materials for diffusion barriers [4]. It is important to note that often it is a quest for a set of compatible materials rather than an individual material. For example, replacing Al with Cu as the interconnect metal required research to identifying materials for diffusion barriers to prevent Cu from diffusing into Si. Similarly if SiO_2 is replaced with a high k gate dielectric, new metal gate electrodes must be identified to supplant present day's polycrystalline silicon gate electrodes [4].

Combinatorial studies help in identifying alloys of metals, nanolaminates, binary and ternary compounds which are useful in terms of perhaps their k value (high or low) or other desirable properties which may be better than the individual constituents. Researchers are also studying the use of carbon nanotubes for digital switching in transistors to keep up with the miniaturization trend [3].

1.6. Improvements in IT and Knowledge Management

A very key component in this race to miniaturization is an efficient IT framework accompanying every other research endeavor. Process models, control algorithms, computational tools, defect management schemes and petabytes of data generated through experiments and simulations in these different research efforts have to be organized and molded into a powerful, didactic, user friendly, online resource facilitating interdisciplinary learning and concerted efforts of modelers and experimentalists- a far from trivial endeavor in itself.

All the above research groups (Figure 1) have a positive feedback on every other group. Some groups are more tightly coupled than the others. The dashed lines in Figure 1 (some double arrowed and some single) indicate the positive feedback in the direction of the arrow. The recursive improvement of the whole industry is fascinating – every improvement in every direction results in a more miniaturized, faster computing machine that facilitates each one of the above research endeavors as long as there is more room at the bottom as Dr. Richard Feynman aptly put it! As we get down to smaller and smaller dimensions we enter the nano and bio world in terms of dimensions where an insightful visionary would see myriad potential lateral technology transfers, applications and novels ways of computing [8] although this would be a digression as Moore’s law pertains to computing in the world of Si based CMOS switches.

This research work contributes to research endeavors depicted in Figure 1 that are marked by the larger shaded circles, through the novel concept of equipment and process programmability. In Chapter 2 we discuss a novel reactor design that renders flexibility, programmability and controllability to the CVD tool used in this research. In Chapter 3 we discuss further design modifications and process modeling, simulations and performance analyses that help in quantifying process parameters and qualifying the reactor designs. This research work includes reactor design, preliminary simulations to test the design, machining and construction of reactor, preliminary experimentation, and modeling, validation of models and prediction using models and finally inferences from these predictions and inferred improvements to the reactor design from these designs thus covering the entire gamut of process and tool development. We hope it serves as an efficient template for future similar research endeavors.

Chapter 2: A Demonstration of Spatially Programmable Chemical Vapor Deposition: Model-Based Uniformity/Non-uniformity Control

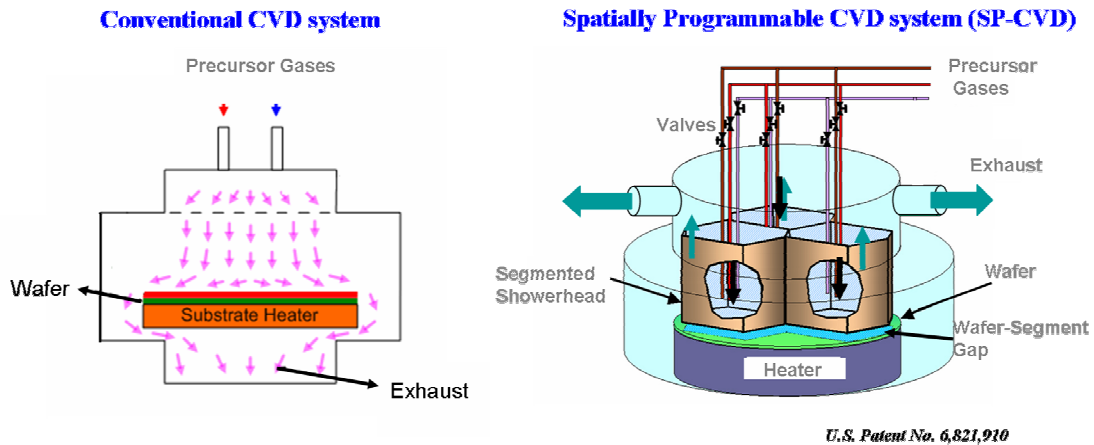
2.1. Introduction

Chemical Vapor Deposition (CVD) tools are prevalent in every semiconductor fabrication facility as an efficient method for depositing non-volatile solid films with good conformality, film quality and microstructure. However most conventional CVD systems are designed for a narrow range of operating conditions and do not offer much flexibility for improving process recipes and optimizing process development cycles for new materials. Furthermore they are usually devoid of “process knobs” or process inputs that can be tweaked using robust and efficient controllers based on Advanced Process Control (APC) techniques [6].

2.2. Conventional CVD reactor design:

Figure 2 illustrates a schematic of a conventional CVD chamber which is prevalent in most semiconductor fabrication facilities. In this design, precursor gases are introduced through a showerhead usually from above the heated wafer. The gases flow down to the wafer surface where they react and deposit a film. The remaining precursors and byproducts then move out radially to the edge of the wafers and around the wafer and then to the volume under the wafer from where they are usually

pumped out of the reaction chamber. Such a flow profile creates a higher



Advantages of SP-CVD:

- Spatial discretization over the wafer surface
- Minimizing convective interaction between segments

Figure 2: Conventional CVD vs. SP-CVD.

concentration of gases closer to the centre of the wafer and a region of depletion closer to the wafer edge thus creating undesirable and uncontrollable non-uniformities in film properties on the wafer surface.

2.3. Earlier work in design improvements:

A good background in recent CVD reactor designs can be found in Jae-Ouk Choo's Ph.D. Thesis [9]. Advanced design features are found in the annular, three-zone Texas Instruments showerhead [10] for tungsten and other CVD processes, where individual gas mass flow controllers could be used to set the gas flow rate to each segment.

In some MOCVD processes, the separation of gas precursors is critical because highly reactive gas precursors can cause undesirable gas phase reactions. In an effort to reduce gas phase reactions, Van der Stricht, Moerman, Demeester, Crawley and Thush [11] designed a vertical reactor with separate feed ports for each precursor

species. Separate gas injectors for individual precursors were designed for a horizontal flow MOCVD reactor introduced by Yang, Huang, Chi and Wu [12]. Theodoropoulos, Mountziaris, Moffat and Han [13] described a new MOCVD reactor design of featuring an annular-ring showerhead configuration that enabled the controlled injection of separate precursors. The authors evaluated several annular ring in that study, and as with Van der Stricht and Yang, Theodoropoulos and co-workers concluded that novel gas delivery designs offered new operational degrees of freedom with which uniformity could be controlled; they also pointed to the importance of simulation tools in optimizing process recipes. Parikh, R.P *et al.* studies the influence of the split-feed inlet design of radial flow reactors on reaction path selectivity for GaN deposition [14].

CVD reactor designs have been developed specifically to allow or improve active control of wafer processing conditions during the dynamic processing cycle. The work at Texas Instruments [15] used multiple heating zones arranged radially across the wafer in single-wafer rapid thermal processing to achieve temperature uniformity. That approach has been adopted by the semiconductor equipment industry, e.g. Applied Materials and CVC Products, Inc. The SEMATECH test bed RTP system [16] and the three-zone RTP system at North Carolina State University [17] use independent lamp zones for compensating edge-cooling effects to control uniformity. Other developments include reduced model-based real-time control studies of the three-zone NCSU RTP system ([18], [19]) and reduced-model-based order state estimation and optimal control of a horizontal high-pressure CVD system ([20], [21], [22]).

This chapter addresses the issue of process flexibility using the concept of a spatially programmable chemical vapor deposition system (SP-CVD) that was developed at the University of Maryland [23]. Earlier work ([9], [24], [25]) describes construction and preliminary testing of the reactor. This chapter describes the results of an expansion of the reactor's capabilities to demonstrate, for the first time, the system's ability to be reprogrammed, effectively reconfiguring the reactor solely in software between deposition runs. To be more precise, reactor system programmability is enabled by the following two design advances:

1. Tool Modularity as defined by equipment components such as the showerhead and gas delivery system designed in a modular fashion giving the tool more flexibility, scalability and extendibility relative to conventional CVD system designs;
2. Process Programmability follows from tool modularity and is the software that endows the tool with the ability to run different recipes over different parts of a wafer, resulting in films with controllable properties across the wafer. This degree of controllability makes possible combinatorial capabilities and can significantly reduce experimentation time by enabling simultaneous experiments on each wafer, accelerating product development cycles and model building.

The objective of this chapter is to demonstrate the programmable design concepts using a prototype, three segment reactor system to deposit tungsten films. The chapter is organized as follows: The next section describes the Spatially Programmable Chemical Vapor Deposition (SP-CVD) reactor and showerhead design followed by a

section which describes the experiments that demonstrate programmability of the SP-CVD system. This chapter culminates with the conclusions and implications for combinatorial CVD.

2.4. Programmable reactor and showerhead design

The SP-CVD reactor design, construction, and operation are described in detail in [9], [24], and [25]; Figure 3 shows a photograph of the main SP-CVD tool while Figure 4 shows a photograph of the gas delivery system. Preliminary experimental tests performed to demonstrate the reactor's ability to deposit spatially patterned films also are described in those references. Figure 5 depicts a schematic diagram of the showerhead and wafer heater assembly inside the reactor. This reactor design controls gas precursor concentrations over predefined areas of the wafer surface by using:

1. A segmented showerhead design that delivers precursor gases to predefined regions over the wafer surface, made possible by a gas delivery system that allows separate control of precursor gas flow rate and composition to each segment. The segmented design results in a discretized space above the wafer surface comprised of individually controlled regions enabling control of two-dimensional gas concentration patterns over the wafer; and
2. A “reverse flow exhaust” method of pumping out residual gases from each showerhead segment up into the Common Exhaust Volume (CEV) that minimizes inter-segment convective gas flows in the gap between the showerhead and the wafer. This design feature makes it possible to control inter-segment region gas species transport by adjusting the gap size because

inter-segment diffusive flux increases proportionally with gap size (Figure 5 and [24]).

These two properties of the reactor enable us to spatially program deposition conditions across the wafer by controlling precursor gas flow rates to each segment.

2.4.1. Gas transport mechanisms

The gas transport mechanisms that are observed in this new reactor configuration illustrated in Figure 5 can be described as follows:

1. Intra-segment gas transport: This transport mechanism refers to the movement of gas species within each segment by the mechanisms of convective transport and diffusion (including thermal diffusion) as reactant gas exits the feed tube and makes its way to the wafer surface and then back up the segment to the CEV.
2. Inter-segment back-diffusion from CEV: This transport mechanism refers to the diffusion of gas from the CEV back into the segments owing to gas composition differences between the CEV and individual segments attributable to different precursor recipes in the different segments or depletion at high deposition rates.
3. Inter-segment gap diffusion: This transport mechanism refers to the diffusion of gas from one segment to the other segments through the gap

between the wafer surface and the bottom of the segments owing to concentration gradients between the segments.

The above mechanisms are quantified through models and simulations and validated through experiments in [24] and [25]].



Figure 3: SP-CVD reactor at LAMP lab.



Figure 4: Gas delivery system for SP-CVD
9 gas lines, 3 to each segment using 9 MFCs to control flow

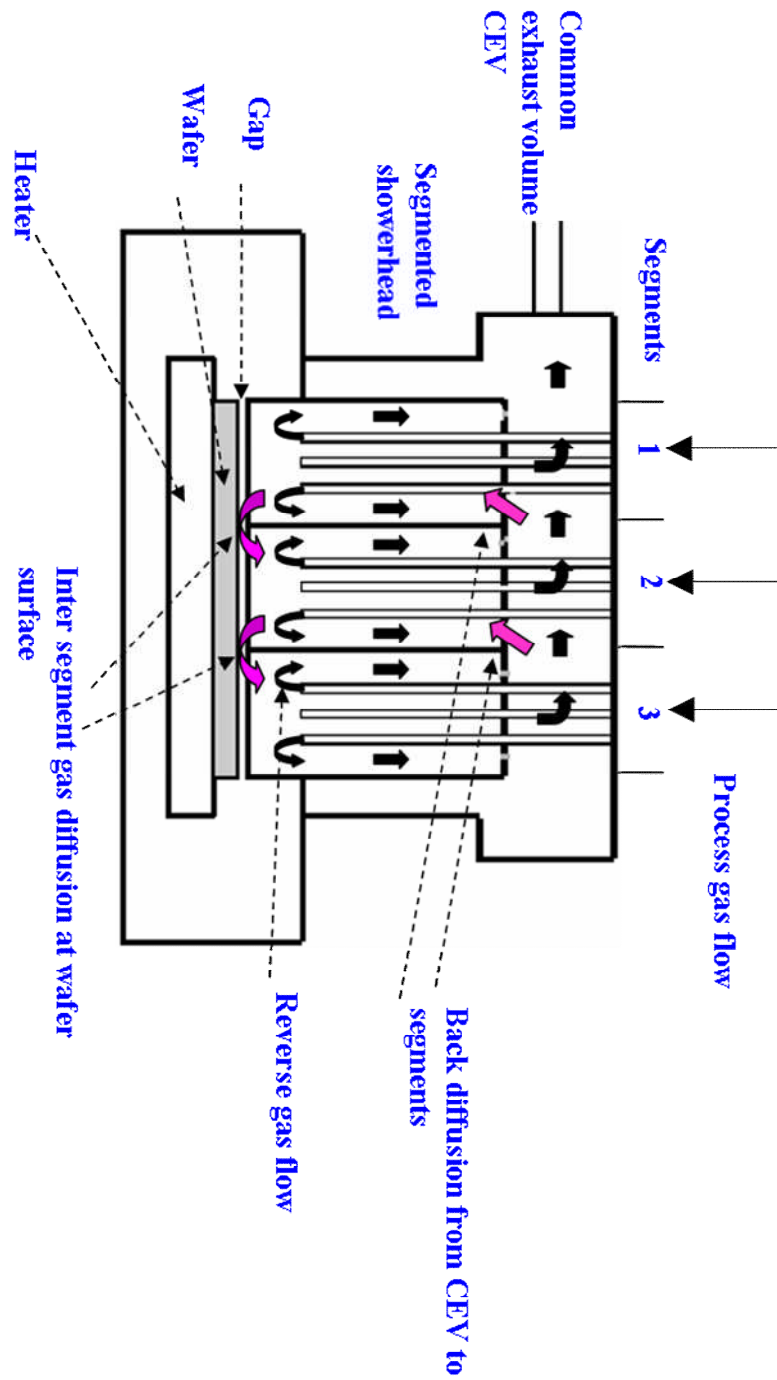


Figure 5: Schematic diagram of the SP-CVD reactor system

2.4.2. Modes of reactor operation

In this work, we expand the operating range of the reactor by demonstrating two modes of operation:

1. Deliberate non-uniformity mode: In this mode, total feed gas molar flow rates to each segment are set to an identical value, but feed gas composition to each segment is varied to generate “patches” of film across the wafer that vary with local gas composition.
2. Uniformity mode: In this mode, total feed molar gas flow rates to each segment are set to an identical value, but feed gas composition to each segment is programmed to generate “patches” of film across the wafer of uniform thicknesses amongst the three segments. The composition in each segment is calculated from models generated from the deliberate non-uniformity experiments described above to compensate for segment-to-segment variability.

These modes of operation along with the steps followed for demonstrating programmability are summarized in Figure 6. In the 3 segment system, precursor gas compositions are adjusted to give three different gas composition recipes (X_A , X_B , X_C); the recipes are then switched between the segments to generate a sequence of wafers from which a model of overall wafer film thickness is created. The model is

then used to reprogram the system to a desired thickness pattern among the three “patches” described above.

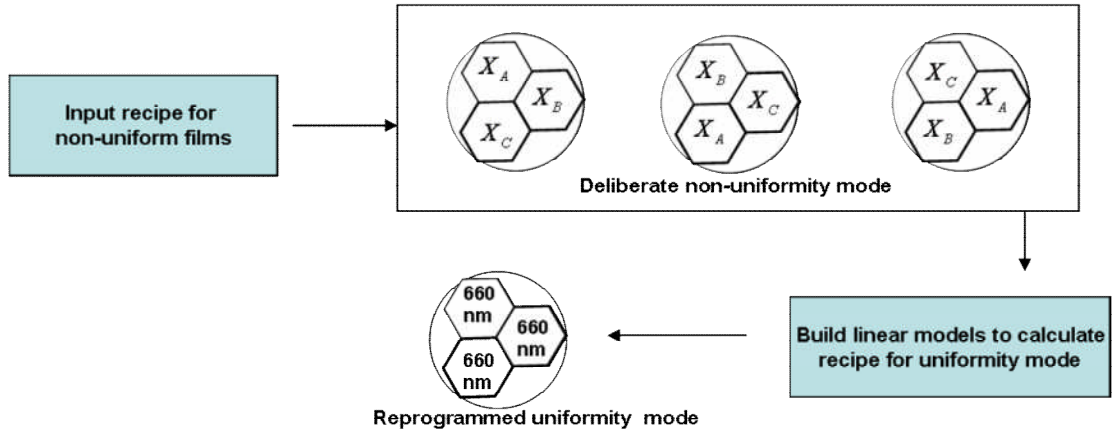


Figure 6: The flow sheet illustration programmed non-uniformity and uniformity experiments.

2.4.3. Prototype reactor experimental system

The chemical system used in this process is tungsten-CVD where the precursor gases are WF_6 and H_2 . The reactor is designed for 4” wafers. Argon is the inert compensatory gas used to maintain the total flow rate to each segment at 60 sccm. For all experiments described in this chapter, the heater temperature is set at 400C giving an approximate wafer temperature of 380C. All experiments were carried out at a reactor pressure of 1 torr maintained by a downstream throttle valve. The gap between the segments and the wafer was kept at 1mm by a linear motion device for the first set of experiments. Deposition time was 900 seconds for all wafers. The gas flow rates of WF_6 , H_2 and Ar are manipulated through mass flow controllers located upstream of the reactor. Details can be found in [25].

The overall deposition reaction is: $WF_6 (g) + 3H_2 (g) \rightarrow W(s) + 6HF (g)$. The gas phase reactions associated with this deposition process are negligible due to low reactor pressure during the process operation [26]. Surface reactions by Si reduction will occur during the film nucleation step. Earlier work using a mass spectrometer to monitor residual gas concentration found this nucleation step was completed in approximately 60 seconds[28], [29]; therefore, it does not play a major role in film deposition in our experiments. The Si reduction is followed by the H_2 reduction of WF_6 which is the dominant reaction. Under our processing conditions, the overall reaction rate can be expressed as the following surface reaction expression [26]:

$$R_{kin} = k_o [P_{WF_6}]^0 [P_{H_2}]^{1/2} \exp\left(-\frac{E_a}{RT}\right) \quad (2.1)$$

where,

R_{kin} is the rate of deposition of Tungsten

$[P_{WF_6}]$ is the partial pressure of WF_6

$[P_{H_2}]$ is the partial pressure of H_2

E_a is the activation energy

R is the universal gas constant

T is the temperature

According to this reaction kinetics model, the reaction rate does not depend on WF_6 partial pressure when sufficient WF_6 is present. However, the reaction rate is proportional to the square root of the hydrogen precursor concentration X_{H_2} :

$$X_{H_2} = \frac{P_{H_2}}{\text{Total pressure } P} \approx \frac{\text{flow of } H_2 \text{ (sccm)}}{\text{Total flow of precursor (sccm)}}$$

in our experiments under the condition of relatively low reactant conversion levels. Hence, in our experiments we should expect a linear relationship between the thickness of the W film and $\sqrt{X_{H_2}}$ or the flow rate of H₂, and so we choose the flow rate of H₂ as the variable in our models in this chapter.

2.5. Demonstration of programmability

The following sections describe the steps that were followed to demonstrate the programmability of the SP-CVD reactor.

2.5.1. Wafer cleaning and reactor conditioning

Each wafer was dipped into 10% HF solution to remove native silicon-oxide film and impurities that block the nucleation of tungsten crystals; after cleaning, the wafers were immediately loaded onto the substrate heater in the reaction chamber. This cleaning time was decided by trial and error with the aim of finding the cleaning time that would still result in blanket tungsten films. We did not quantify the oxide etching rate of the HF solution or the oxide thickness before and after cleaning. The wafers used were (100) non-oxide Si wafers (Boron doped, resistivity of 14-22 ohm-cm). A cleaning time of 5 minutes in HF sufficed followed by rinsing in distilled water and drying with N₂. The background pressure of the reactor, found after each wafer is loaded is about 1×10^{-5} torr (measured by an ion gauge installed in the reactor). The entire operation of venting the load lock, loading the wafer, pumping down the load lock and transferring the wafer to the reactor takes about 5 minutes.

At the start of each day of experimentation approximately two hours were spent conditioning the reactor walls. This conditioning was done by flowing process gases at room temperature over a dummy wafer. Also, the first wafer used for deposition was discarded to eliminate the anomalies due to the first wafer effect commonly seen on starting process tools after an overnight or a longer idle time. During idling the reactor is maintained at a pressure of about 1×10^{-7} torr using a turbo molecular pump.

2.5.2. Deliberate non-uniformity experiments for model building

Table 1 summarizes a set of experiments in which the reactor was operated in the non-uniformity mode to identify a model between the thickness of the W film deposited under each segment and the flow rate of H_2 in that same segment. The wafer names are not listed in chronological order, but are grouped according to the recipe used to process those wafers. Wafers W11 and W13 were scrapped due to processing problems which resulted in film anomalies. The concept behind these model identification experiments was to cycle through the following three recipes

(i) WF_6 flow of 6, 9 and 12 sccm in segments 1, 2 and 3 respectively. Three wafers with good quality films were produced using this recipe.

(ii) WF_6 flow of 9, 12 and 6 sccm in segments 1, 2 and 3 respectively. Two wafers with good quality films were produced using this recipe.

(iii) WF_6 flow of 12, 6 and 9 sccm in segments 1, 2 and 3 respectively. Four wafers with good quality films were produced using this recipe.

As a result, a total of 9 wafers were obtained for model development using the non-uniformity operation mode of the SP-CVD reactor.

WAFER NO	WF6 FLOW (sccm)			4PPTHICKNESS(nm)			
	Seg1 flow	Seg2 flow	Seg3 flow	Seg1 non-unif thickness	Seg2 non-unif thickness	Seg3 non-unif thickness	
W10	6(24)	9(36)	12(48)	519	769	693	
W14	6(24)	9(36)	12(48)	495	636	648	
W17	6(24)	9(36)	12(48)	619	793	678	
$\sqrt{X_{H_2}}$	0.63	0.77	0.89	544	733	673	MEAN THICKNESS
				66	85	23	STDDEV
				12	12	3	STDDEV%
W16	9(36)	12(48)	6(24)	731	795	604	
W19	9(36)	12(48)	6(24)	592	832	564	
$\sqrt{X_{H_2}}$	0.77	0.89	0.63	662	814	584	MEAN THICKNESS
				98	26	28	STDDEV
				15	3	5	STDDEV%
W12	12(48)	6(24)	9(36)	592	599	609	
W15	12(48)	6(24)	9(36)	713	720	678	
W18	12(48)	6(24)	9(36)	650	700	632	
W20	12(48)	6(24)	9(36)	725	736	708	
$\sqrt{X_{H_2}}$	0.89	0.63	0.77	670	689	657	MEAN THICKNESS
				62	62	45	STDDEV
				9	9	7	STDDEV%

Table 1: Recipes and results for deliberate non-uniformity experiments.
WF₆:H₂ flow ratio in each segment=1:4. H₂ flow in parentheses.
Ar Flow in each segment =60 - (H₂ FLOW + WF₆ FLOW) sccm.

2.5.3. Ex-situ metrology

After each deposition process, film thickness was measured using a 4 point probe (4PP) ex-situ metrology station (Figure 7a). The 4-point probe measurements result in a rectangular grid of measurements over the wafer surfaces with an approximate spatial resolution of 3.45 mm generating 900 measurement points. Figure 7b illustrates the graphical output obtained from the LabVIEW based 4-point probe station.

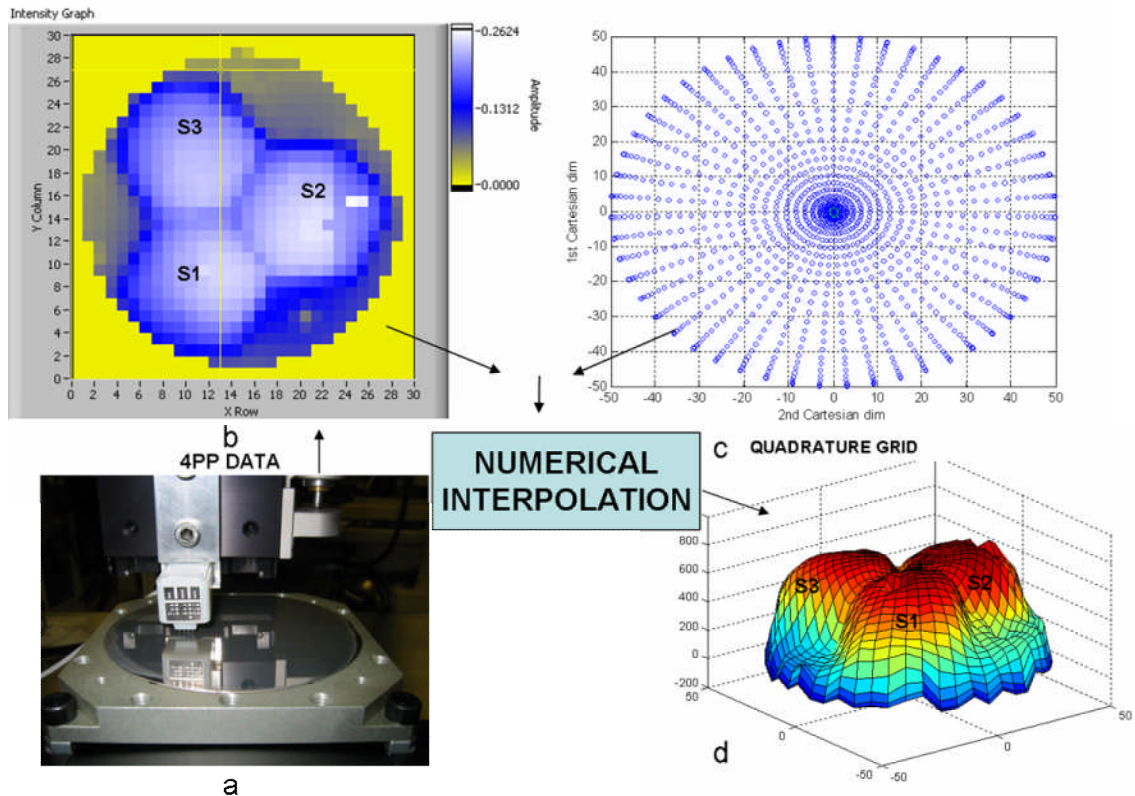


Figure 7: Accurate interpretation of 4PP metrology data using a numerical quadrature technique.

Numerical analysis of these wafer maps begins by interpolating the thickness data to a numerical quadrature grid defined on a computational domain that has the same physical dimensions as the wafer (Figure 7c). This numerical procedure is carried out to simplify subsequent calculations; for example, the exact position of the wafer with respect to the segmented showerhead is difficult to fix because the wafer is lowered onto the heater by a single pin operated by a manual linear motion device. As the wafer is lowered it rotates on the pin and this rotation is not repeatable. Therefore, we use a post-processing quadrature based numerical technique based on finding the maximum correlation between the wafer deposition pattern and a pattern representing the hexagonal segment regions directly under the showerhead, and rotate the wafer (numerically) to maximize this correlation. This technique allows us to orient all wafers accurately with respect to the showerhead segments; the results are displayed in Figure 8. (See for example [30] for the underlying numerical methods, and [31] for another CVD application).

This quadrature grid also is used for numerical interpolation of film thickness in each segment to give a finer (higher resolution) representation of film thickness under each segment. Figure 7d shows the result of this quadrature-based numerical interpolation technique applied to a test wafer. S1, S2 and S3 represent segments 1, 2 and 3 respectively. Figure 8 depicts the thickness profiles of the 9 wafers processed by the non-uniformity mode of the SP-CVD reactor obtained by this numerical technique. The thicknesses are reported in Table 1. The wafers with identical recipes were grouped together and the mean thicknesses under each segment in each group were calculated. From each gas flow recipe, the mole fraction of H_2 , denoted by X_{H_2} , in

each segment is calculated by dividing the flow rate of H₂ by the total gas flow rate (60 sccm) in that segment. The square root of the mole fraction $\sqrt{X_{H_2}}$ is calculated and displayed in the table.

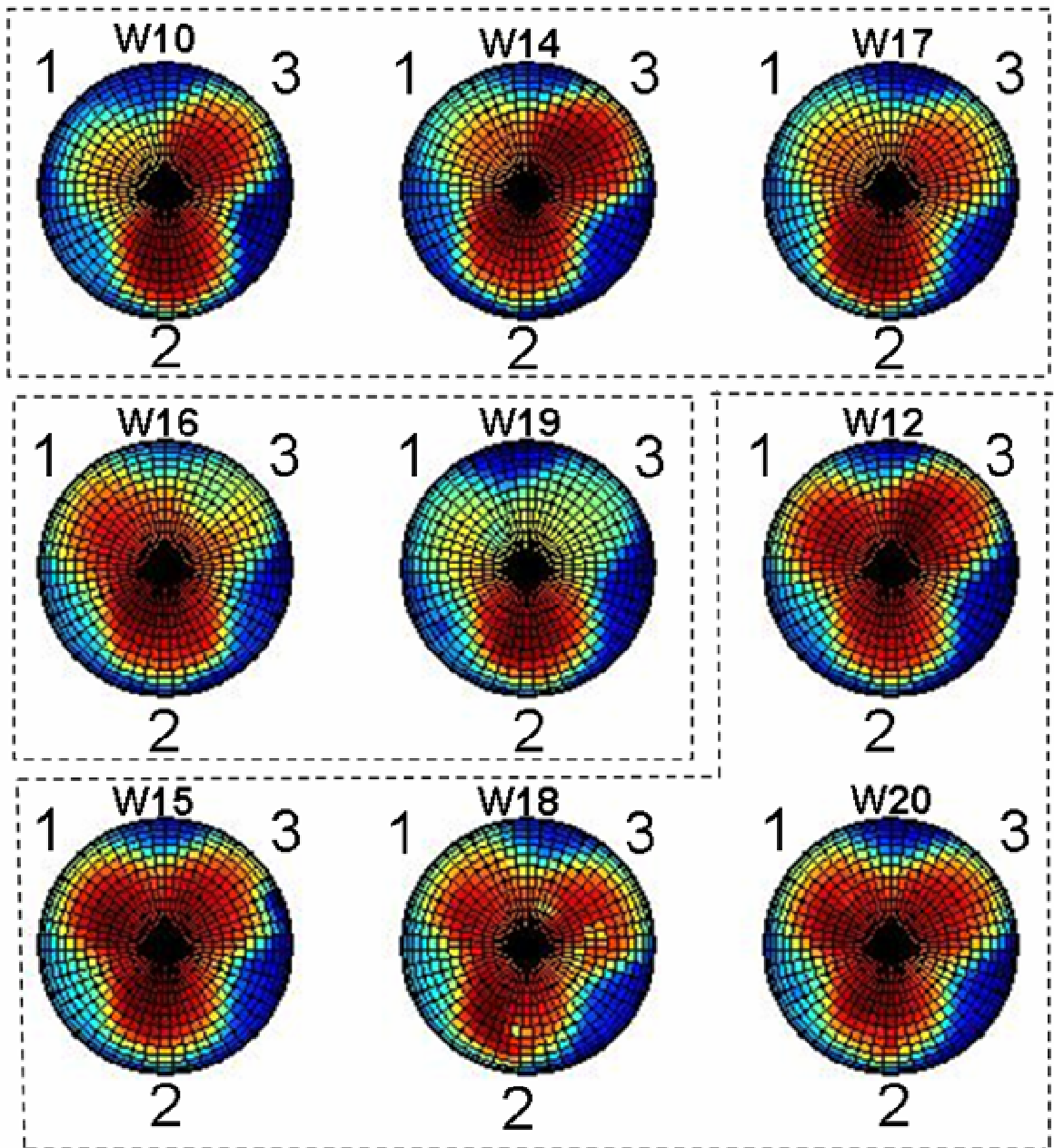


Figure 8: Wafer profiles (deliberate Non-uniformity DOEs)
 Wafers W10, W14 and W17 belong to one group.
 Wafers W16, and W19 belong to the second group.
 Wafers W12, W15, W18 and W20 belong to the third group.
 Numbers 1, 2 & 3 refer to the three segments

2.5.4. Building a model between the W film thickness and the flow rate of H₂

The form of the function relating the film thickness to the corresponding flow rate of H₂ is chosen to be:

$$T_i = a_i + b_i (Flow_{H_2,i})^{1/2} \quad (2.2)$$

where T_i is the mean film thickness under segment $i=1, 2, 3$, and $Flow_{H_2,i}$ is the flow rate of H₂ under segment $i=1, 2, 3$ (Table 1). The form of the function is chosen to reflect the square root dependency of deposition rate on H₂ mole fraction, shown in equation (1). This function (2) then was used to construct the linear models depicted in Figure 9. a_i and b_i represent the slope and intercept, respectively, of a line drawn through the data points using a least squares regression.

2.5.5. Inferences from the deliberate non-uniformity experiments

The results from the deliberate non-uniformity experiments are plotted in Figure 8 and Figure 9. Two trends emerge from these profiles:

1. The proposed correlation between the H₂ flow rate and film thickness of equation (1) holds, where the film thickness increases with H₂ flow rate in each segment
2. The film thickness under S2 is consistently thicker compared to those corresponding to S1 and S2 for the same gas composition.

The latter trend is attributed to a local hot spot under the region S2 resulting from a larger number of resistance heater coils under this segment. This hotter region results in a higher W film growth rate and so a thicker film results under S2. Because this

non-uniform heating can be viewed as a process disturbance, we re-program the reactor in the next set of experiments by adjusting the recipes in each segment to compensate for this disturbance. Uniform films are produced by exploiting the programmability of this reactor design. We also note that this multi-segmented showerhead was exploited to minimize the number of experiments needed to identify a model between the wafer recipe and deposition thickness for each segment. With a conventional CVD reactor the same modeling effort would have required 3 times as many as the number of wafers used here.

Finally, in Table 1, we can observe the effect of wafer to wafer process disturbances that produce different *mean* film thicknesses for wafers with the same flow recipes. Improving process repeatability is not the main focus of this set of experiments. The aim here is to demonstrate spatial programmability which can be reasonably decoupled from process repeatability.

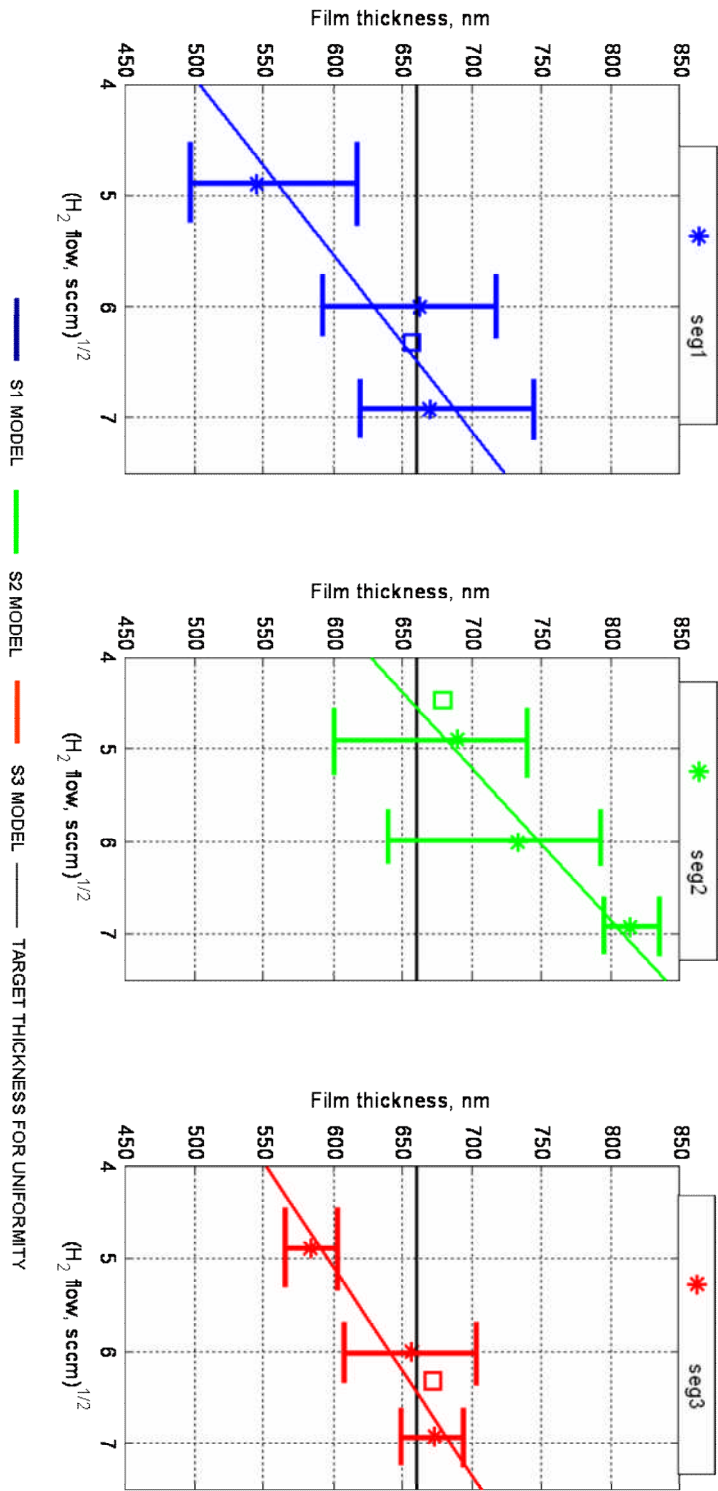
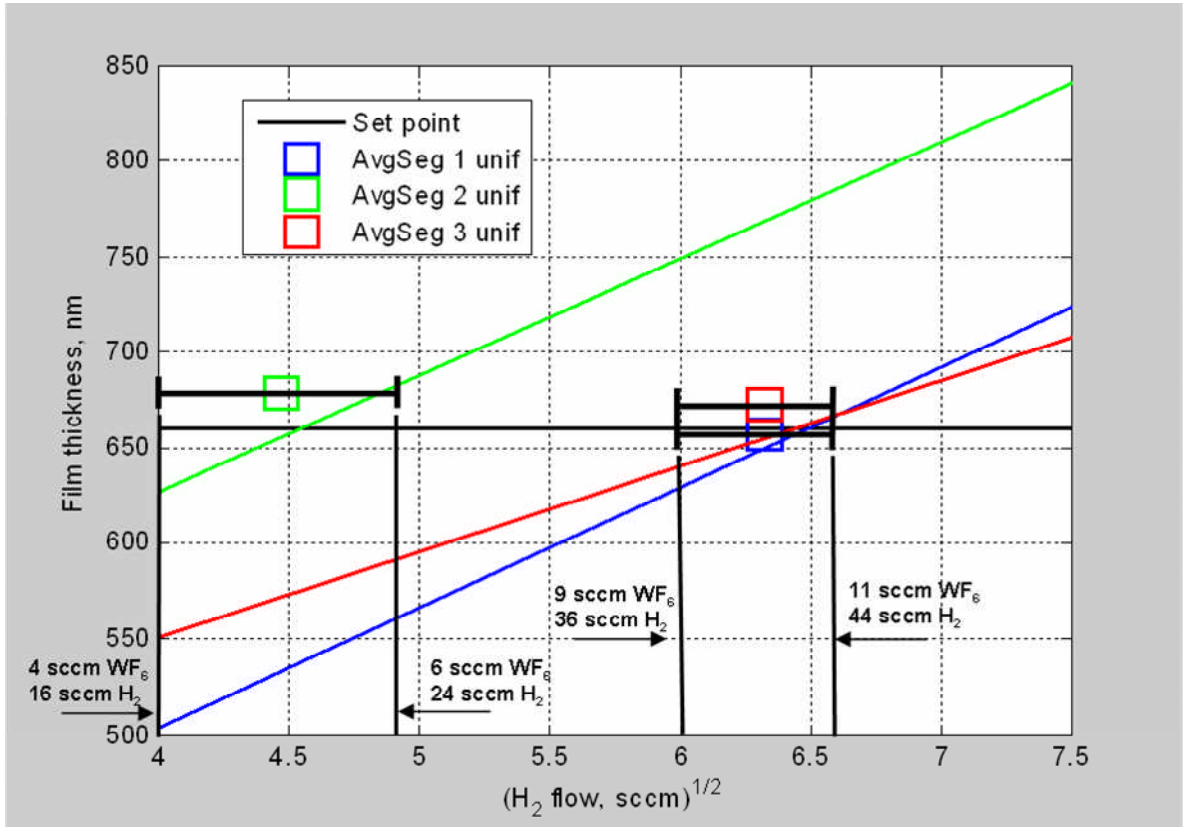


Figure 9: Plot showing linear models for each segment. The vertical error bars range from the minimum thickness to the maximum thickness obtained for that particular flow recipe (From Table1). The solid black line is the new set point. This line intersects the linear models and this point of intersection when projected on to the x axis gives us the new recipe (WF₆ and H₂ flowrates). The square markers denote the average thickness in each segment for wafers W32 to W41 processed using the segment-to-segment uniformity recipe.

2.5.6. Reprogramming the process for uniformity

The three linear models (with respect to the square root of the H₂ flow rate) depicted in Figure 10 were used to reprogram the process as follows: we chose the target thickness of 660 nm depicted by the horizontal solid line intersecting all three linear models. The points of intersection were projected onto the abscissa (square root of the H₂ flow rate); this projection translated to a WF₆ flow recipe of 10, 5 and 10 sccm in S1, S2 and S3, respectively, as shown in Figure 9 which translates to a H₂ flow recipe of 40, 20 and 40 sccm in S1, S2 and S3, respectively. We then performed deposition experiments with this recipe on a sequence of 10 wafers: W32 to W41. All the deposition runs were carried out in a single day and film thickness was measured using the ex-situ 4PP metrology station. The results are tabulated in Table 2. The average thickness in each segment over these 10 wafers was calculated and plotted in Figure 10 using square markers. The horizontal error bars on the square markers indicate the range of flow rates on the x axis that would have resulted in the same reprogrammed flow rate recipe of WF₆ (5 sccm in S2 and 10 sccm in S1 and S3 which translates to a H₂ flow rate of 20 sccm in S2 and 40 sccm in S1 and S3) because of the 1 sccm resolution of the mass flow controllers used to control the mass flow rates.



— S1 MODEL — S2 MODEL — S3 MODEL — TARGET THICKNESS FOR UNIFORMITY

Figure 10: This figure illustrates the three linear models in one plot. The horizontal error bars on the averaged uniform profiles under each segment represent the range of WF_6 flow rates that would have resulted in the same uniformity producing recipe needed for the set point of 660 nm, due to the 1sccm resolution of the mass flow controllers used to control the precursor mass flow rates.

2.5.7. Inferences from the re-programmed uniformity experiments

The re-programmed uniformity experiments demonstrated the efficacy of the novel SP-CVD reactor design which enables us to switch between deliberate non-uniformity producing recipes to recipes which produced segment to segment uniformity, all in the process control software used to control the feed gas MFCs. The re-programming was effective in achieving close to target thickness in each segment (660 nm). Table 2 depicts the mean film thickness and standard deviation for the 10 wafers, W32 to W41. An inter-segment uniformity approaching 0.60 % (calculated using the same formula used to calculate standard deviation) was achieved in the best case. The worst case approached 4.87% thickness standard deviation and this could be attributed to unmeasured disturbances of a downstream throttle valve and other mechanisms currently under investigation. Figure 11 shows a plot of the results summarized in Table 2. Figure 12 shows averaged thickness profiles for both the deliberate non-uniformity experiments and the re-programmed uniformity experiments.

Target = 660nm

REPROGRAMMED RECIPE

W 32 - 41	S1	S2	S3
WF6 (sccm)	10	5	10
H2 (sccm)	40	20	40
Ar (sccm)	10	35	10

MEASURE OF SEGMENT
UNIFORMITY OVER 10 WAFERS

WAFER NO	THICKNESS (nm)			MEAN	STD%
	S1	S2	S3		
W32	727	761	709	732	3.18
W33	602	607	600	603	0.60
W34	631	684	677	664	4.34
W35	609	616	664	630	4.75
W36	713	748	786	749	4.87
W37	608	635	619	621	2.19
W38	653	682	643	659	3.07
W39	675	662	650	662	1.89
W40	729	750	737	739	1.43
W41	621	641	640	634	1.78
MEAN	656.80	678.60	672.50		
STD	50.84	57.14	56.78		
STD%	7.74	8.42	8.44		

MEASURE OF PROCESS
REPEATABILITY OVER 10 WAFERS

Table 2: Programmed uniformity results for W32 - W41

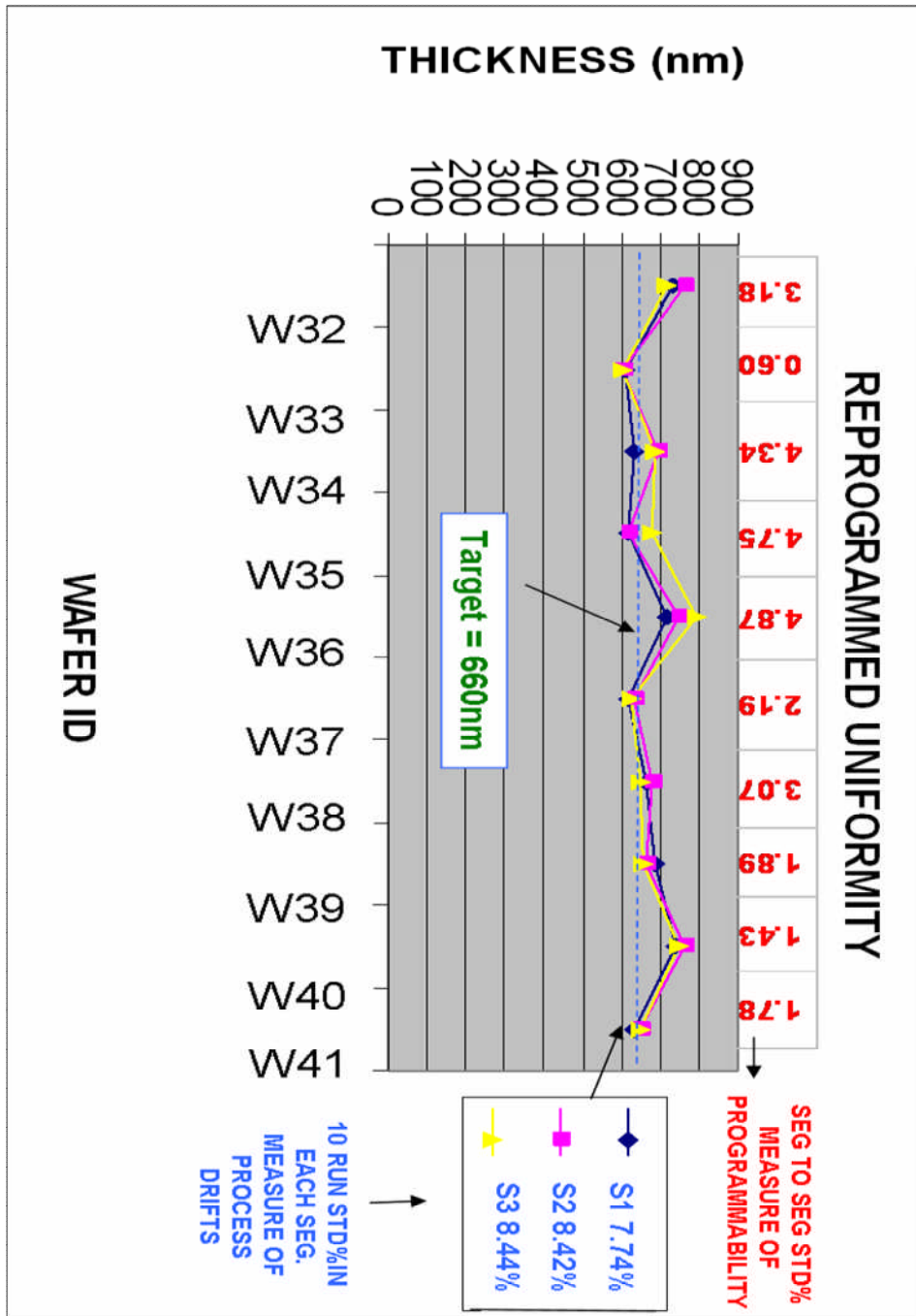


Figure 11: A plot of the programmed uniformity results shown in Table 2

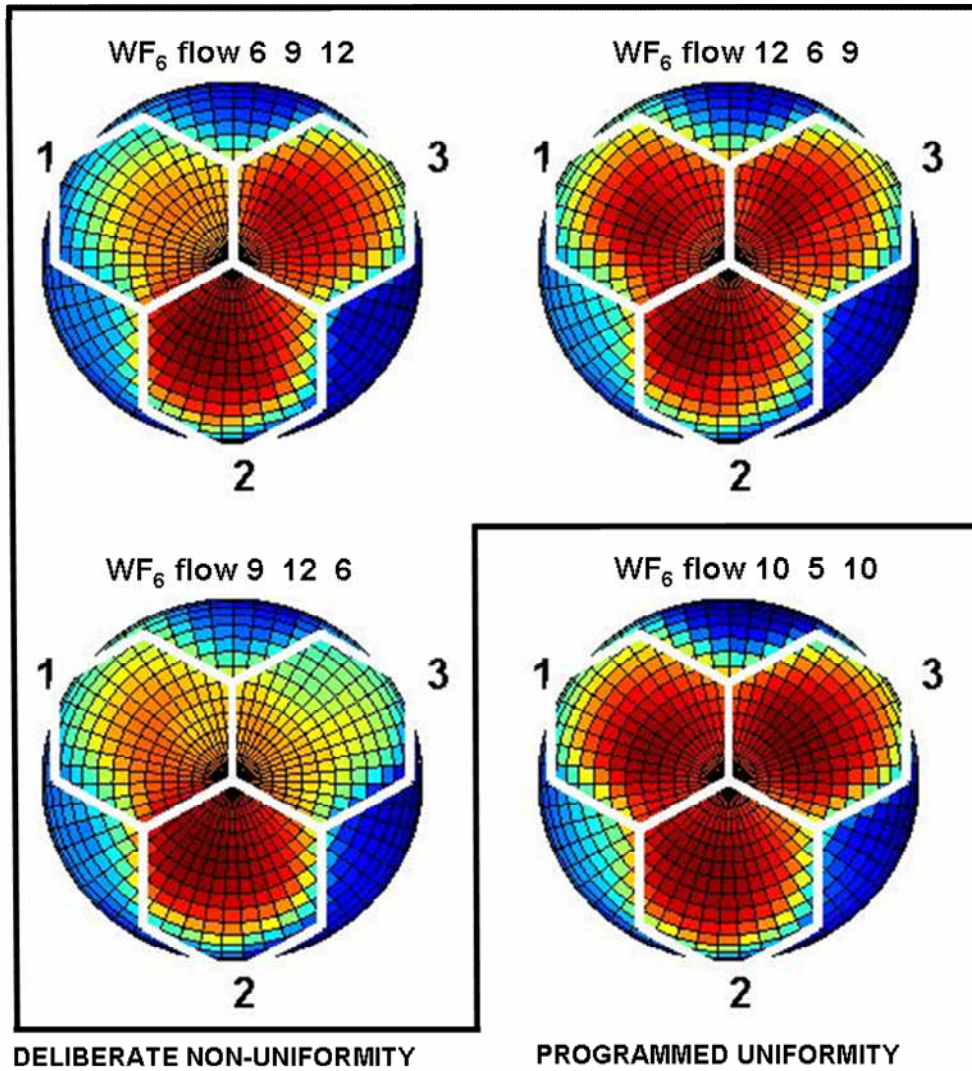


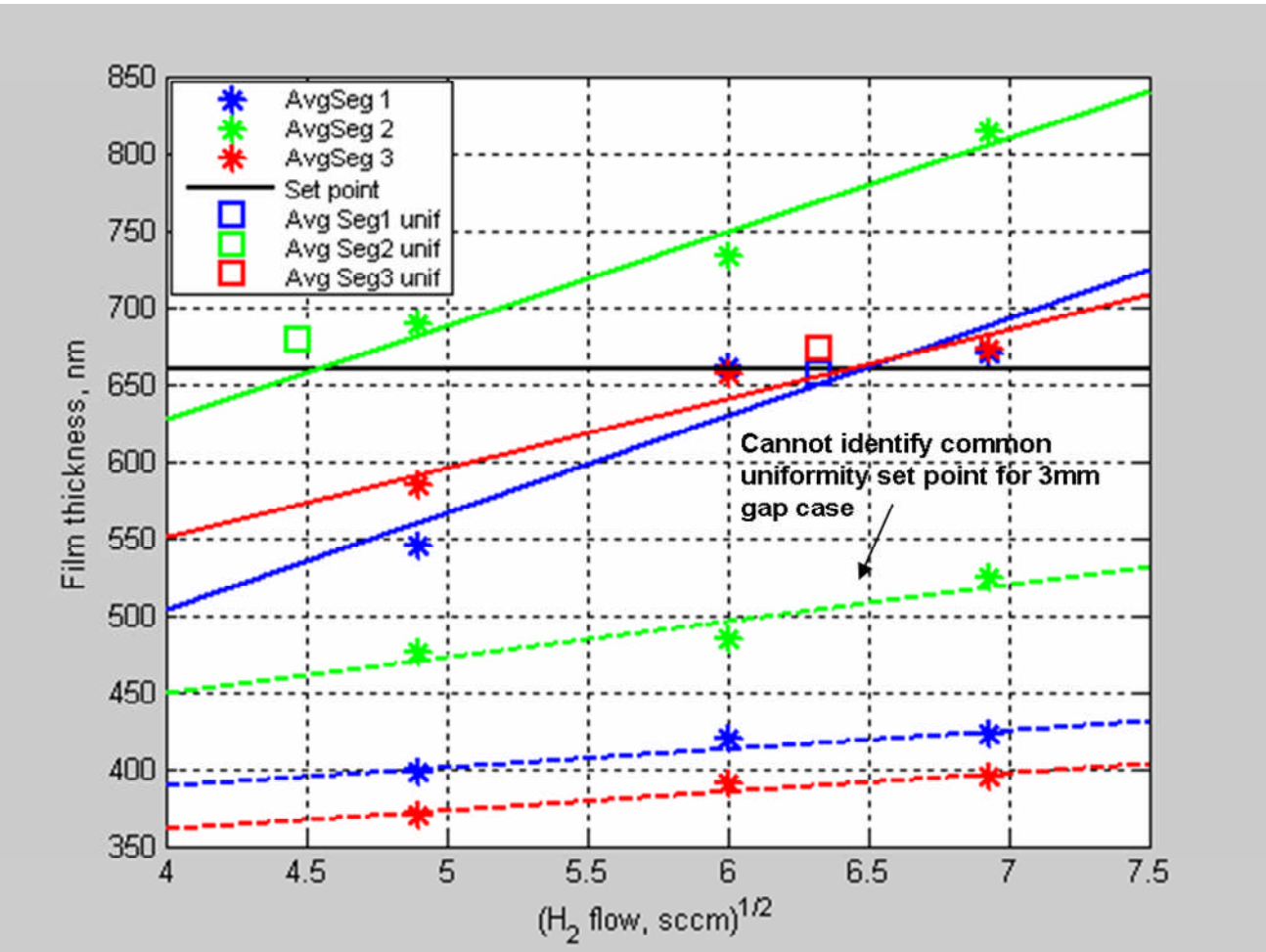
Figure 12: Averaged profiles

2.5.8. Effect of showerhead-wafer gap size on programmability

Figure 13 shows the linear models corresponding to a 3 mm showerhead-wafer gap, produced using the same approach to modeling and programmability as for the 1mm showerhead-wafer gap size experiments. In this figure, the linear models correlating film thickness to H₂ mole fraction for the 1mm showerhead-wafer gap size and the 3 mm showerhead-wafer gap size are compared. Two effects are observed here:

1. In the 3mm deliberate non-uniformity experiments, the thicknesses of the films are considerably lower than those corresponding to the 1mm gap case. This difference is attributable to a fraction of the gases fed to each segment “leaking out” through the gap into the reaction chamber and subsequently being pumped out from the chamber region outside of the segments. The current reactor design is such that the baffle located at the top of the segments and just below the CEV is not leak tight (Figure 14) and so allows gases from the chamber volume outside the segments to enter the CEV. This fraction of the precursor gases escaping through the increased gap does not contribute to the film deposition on the wafer. Minimizing this external chamber volume outside the segments may reduce the depletion of precursors around the edge of the wafer from the outer segments; future designs which will incorporate more segments and smaller chamber volumes.
2. The slopes of the linear models corresponding to the 3 mm gap experiments are smaller in magnitude than those of the 1 mm gap experiments. One factor contributing to the reduction in slope is the increased inter-segment diffusion arising due to the increased gap size. As a result, the segments are not as effectively

decoupled when the gap size is 3mm gap size compared to a gap size of 1mm. For example, in the 1mm gap size experiments, a 0.63 mole fraction of H₂ in S1 produces a mean film thickness of 544 nm (Table 1) while a 0.77 mole fraction of H₂ produces a mean film thickness of 662 nm. Thus, an increase of 0.14 in the H₂ mole fraction results in a mean film thickness increase of 108 nm. However when the gap size is 3 mm, the same increase of 0.14 in H₂ mole fraction in S1 results only in a mean film thickness increase of 15 nm, thus reducing the slope of the linear model. The gases escaping to the chamber volume, as in case (a), also contributes to this reduction in slope.



— 1 mm gap non-uniformity - - - 3 mm gap non-uniformity
— data & models - - - data & models
— - - -

Figure 13: 3mm vs. 1mm data: Linear models

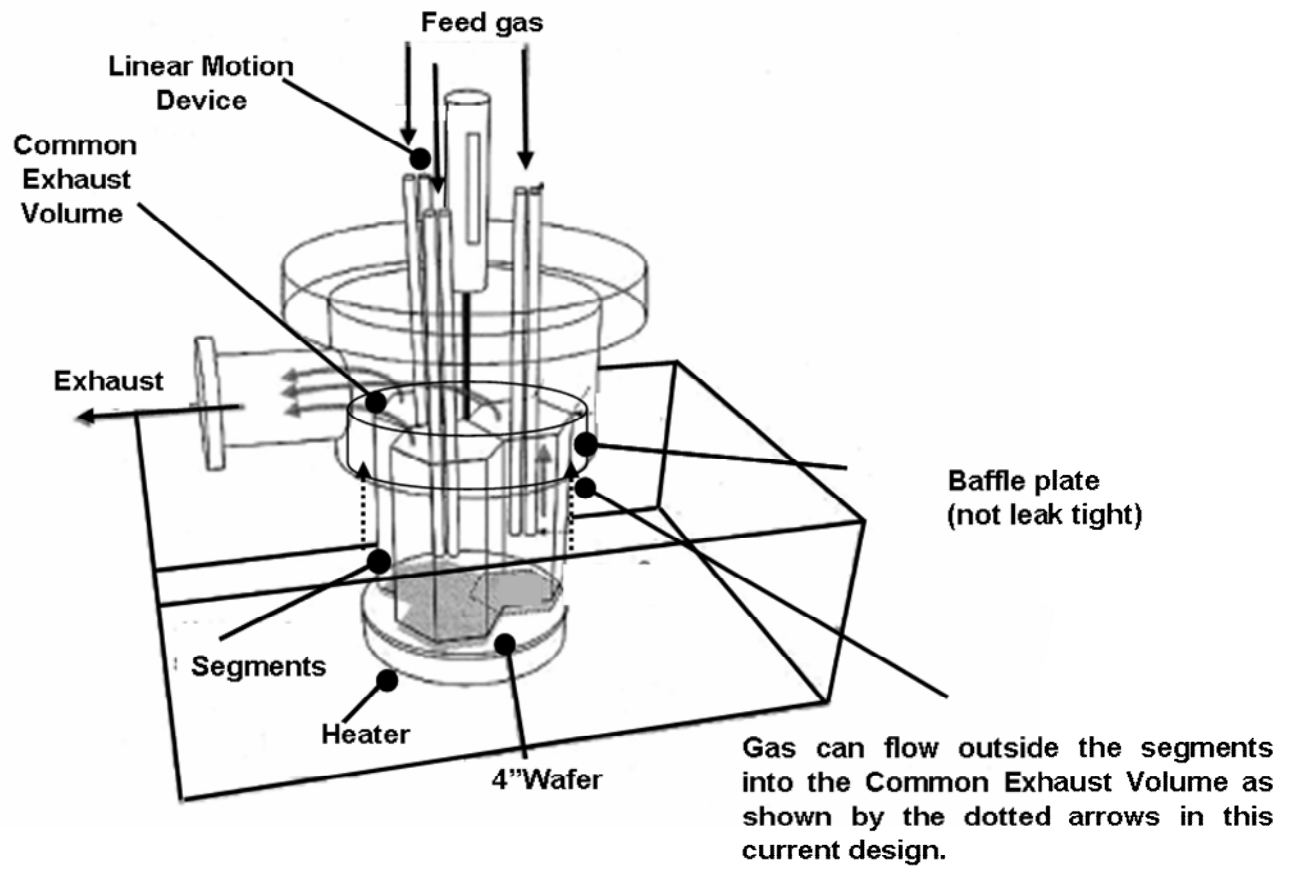


Figure 14: Schematic of the SP-CVD reactor assembly

We could not conduct “re-programmed uniformity” experiments in the 3mm gap case. As seen in Figure 13, we cannot identify a common thickness set point that would intersect all 3 segment model lines within the operating range of gas flow recipes, such as was done in the 1mm gap size case. This problem would not arise if the linear models were “close enough” (visually from Figure 13) to one another. The hotter part of the wafer under S2 is a major contributing factor to the dissimilarity amongst the segments, translating into the linear model of S2 not being “close enough” to the linear models of S1 and S3. Were the temperature profile more uniform, the deposition behavior for S2 would be closer to those of S1 and S3 and one would be able to reprogram the system using a recipe to produce the same film thickness in every segment within the operating range of the gas delivery system.

We would like to point out that in the modeling approach in this chapter we have not explicitly addressed the interaction amongst the segments in our models. Models that take the segment to segment interaction into account are described in the next chapter. One such approach that provides evidence of little segment-to-segment interaction at 1mm gap is discussed in the following section.

2.6. Segment-to-segment interaction analysis in the programmable reactor

The 1mm gap case: In this modeling approach, we consider the problem of creating an empirical model from a sequence of N full wafer maps $\{W_n\}_{n=1}^N$, each map corresponding to a particular process recipe denoted as $\{S_n^1, S_n^2, S_n^3\}$ where S_n^i denotes the hydrogen flow in sccm to each segment i corresponding to wafer n . The model

will predict the entire wafer film thickness profile $W^{pred}(r, \theta)$ (in nm) and, based on the square root dependence of W film growth with H_2 concentration, will take the form

$$W^{pred}(r, \theta) = B_0(r, \theta) + B_1(r, \theta)\sqrt{S^1} + B_2(r, \theta)\sqrt{S^2} + B_3(r, \theta)\sqrt{S^3} + B_4(r, \theta)g_n, \quad (2.3)$$

where g_n is the inter segment gap corresponding to wafer n .

Given this form of the model it is easy to see that the sensitivity of the wafer film thickness profile to the H_2 feed is given by

$$\frac{\partial W^{pred}(r, \theta)}{\partial S^i} = \frac{B_i(r, \theta)}{2\sqrt{S_{avg}^i}} \quad (2.4)$$

and

$$\frac{\partial W^{pred}(r, \theta)}{\partial g} = B_4(r, \theta) \quad (2.5)$$

at the average of all process recipes.

The spatially varying coefficients $B_i(r, \theta)$ are computed from the solution of the least squares procedure using the N experimentally determined thickness maps and corresponding process recipes, where $N > 4$:

$$\begin{pmatrix} W_1 \\ \vdots \\ W_n \\ \vdots \\ W_N \end{pmatrix} = \begin{pmatrix} 1 & \sqrt{S_1^1} & \sqrt{S_1^2} & \sqrt{S_1^3} & g_1 \\ \vdots & \vdots & \vdots & \vdots & \vdots \\ 1 & \sqrt{S_n^1} & \sqrt{S_n^2} & \sqrt{S_n^3} & g_n \\ \vdots & \vdots & \vdots & \vdots & \vdots \\ 1 & \sqrt{S_N^1} & \sqrt{S_N^2} & \sqrt{S_N^3} & g_N \end{pmatrix} \begin{pmatrix} B_0 \\ B_1 \\ B_2 \\ B_3 \\ B_4 \end{pmatrix} \quad (2.6)$$

In Figure 15, we see strong evidence for the lack of segment-to-segment interaction for the 1mm gap case - this is demonstrated by the 6-10nm/sccm H_2 change in total film thickness with each sccm of H_2 flow in each segment region where the H_2 is

changed, and virtually no change in the other segments. These results correspond to the system linearized at a 30 sccm H₂ flow to each segment. Of course, this behavior is expected to change with increasing gap size, this will be tested in the next round of experiments. The numerical techniques will be discussed in chapter 3.

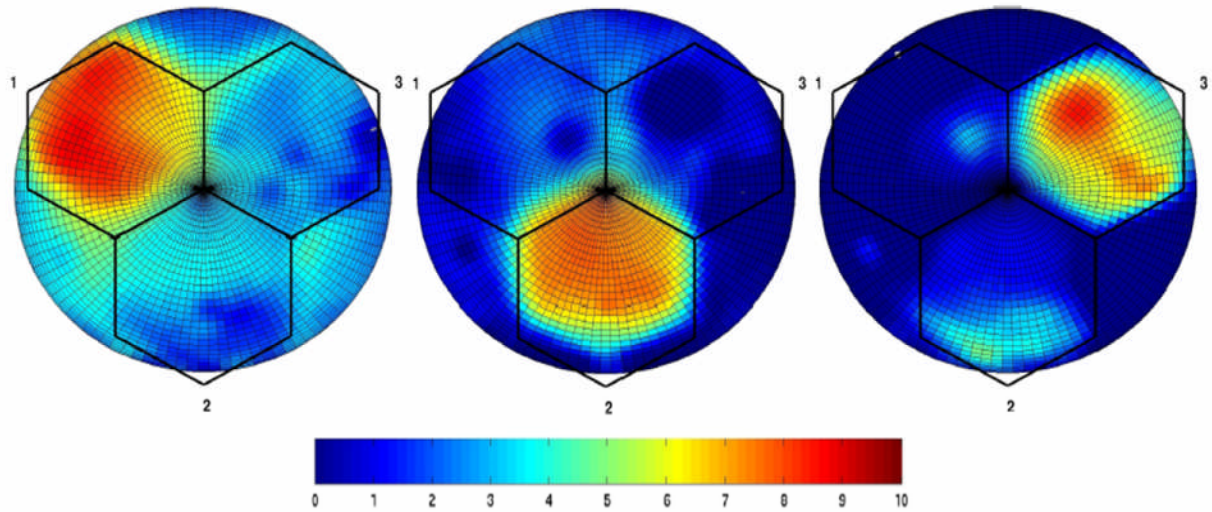


Figure 15: Sensitivity (nm/sccm H₂) with respect to H₂ flow to segment 1 (left), segment 2 (center), and segment 3 (right).

2.7. Chapter summary

We introduced the reader to the new SP-CVD design pointing out the 2 main advantages i.e. spatial discretization capability and a handle to control convective gas flow over the wafer surface and controlling concentration gradients as a consequence.

We discussed the reaction chemistry, the kinetics and the experimental procedure.

Different recipes were cycled through each of the segments in a sequence of deposition experiments to develop a linear model relating precursor concentration to film thickness in each segment region. We did not vary the wafer-segment gap size because the conversion rates at higher gaps were too low to obtain films of substantial thickness that made deriving the linear models possible (Figure 13). As a demonstration of spatial programmability, the system was re-programmed using this

model to produce uniform thickness amongst the segments; inter-segment uniformity approaching 0.60 % (thickness standard deviation) was demonstrated.

Chapter 3: Demonstration of gradient control

3.1. Introduction

As discussed in Chapter 2, conventional CVD systems are designed for a narrow range of operating conditions and do not offer much flexibility for improving process recipes and optimizing process development cycles for new materials. Also, most designs do not allow for controlling precursor concentration gradients over a wafer surface during a deposition run allowing for combinatorial capabilities.

There are relatively few examples of chemical vapor deposition reactor systems designed with combinatorial capabilities. Those that do exist, however, all demonstrate the capability to produce films with graded properties over a portion of the substrate surface. For example, the CVD reactor design of Gladfelter [32], [33] features three feed tubes in a triangular arrangement across the substrate; a different single-source precursor is fed through each tube, generating compositional spreads of three metal dioxides over the substrate. In Wang [34]-[36], thickness graded films of hydrogenated silicon were deposited in a hot-wire CVD system featuring a mask and motorized shutter; control of the shutter speed was used to create strips of graded films over the substrate. Finally, in Taylor and Semancik [37], microhotplate devices were used to control the temperature in an array of micro-scale substrate samples; it was found that temperature gradients in the microhotplate supports resulted in a microstructurally graded film on the support legs. References [23], [25] and [38] describes the preliminary construction and testing of a spatially programmable

chemical vapor deposition (SP-CVD) system that was developed at the University of Maryland. The “original” SP-CVD reactor design (Figure 5 henceforth denoted as design A), construction, operation and preliminary evaluation experiments are described in the cited references mentioned in Chapter 2.

The results from the Chapter 2 cited demonstrated for the first time the SP-CVD system’s ability to be reprogrammed, effectively reconfiguring the reactor solely in software between deposition runs to intentionally induce spatially non-uniform thickness deposition patterns on a single wafer. The results are published in [38]. In that chapter, a relatively simple linear model was used to relate average film thickness under each of the segments to the feed gas recipe of each segment. Because this model did not account for segment to segment interactions, a more accurate modeling approach is developed in this chapter to enable modeling of those interactions.

The purpose of this chapter is to demonstrate the use of Response Surface Models (RS models) to predict film thickness response over the entire wafer to adjustable process parameters enabling control to a specified thickness spatial function, such as a linear thickness gradient across a patch of wafer surface. This model is used to quantify the reactor’s performance and examine the relative merits of different reactor designs. This approach is applied to evaluate two reactor designs: the “original” SP-CVD reactor (design A) and a modification (design B) motivated by an attempt to reduce the chamber volume.

3.2. Modeling for design A

Key to this study is the development of an accurate model of the full wafer response to adjustable process operating conditions; the model is necessary to compute process

recipes that optimize a wafer profile objective function. The model, while physically motivated, will be identified from a set of experiments.

3.2.1. The response surface approach:

The response surface modeling approach comprises of the following three steps [10]:

- 1) Systematic experiments: This step entails setting up a series of experiments that generate a range of reliable measurements of the desired output or response variable. The input variables/predictor variables are varied systematically to generate the range of measurements of the response variable by running experiments on the process tool. For the reactor designs discussed in this chapter, we selected a subset of experiments based on our intuitive understanding of segment to segment interactions based on the results from preliminary experiments in [38], followed by a statistical analysis of the estimated parameters.
- 2) Identify a mathematical model relating the response variables (wafer thickness profile) to the input variables. The model form (linear vs. quadratic for example) is based on our physical and intuitive understanding of the process. The model is tested for accuracy and validated. The derivation of the RS model is discussed in detail in the next section.
- 3) The RS model is used to optimize the settings of the input variables to minimize the value of an objective function, based on our film gradient control criterion, solving a constrained non-linear optimization problem. This optimization is discussed in section 3.3.3.

In this chapter, the input variables of the reactor system are defined by the recipe of the SP-CVD tool. This recipe comprises the flow rate of H₂, the flow rate of WF₆ (H₂:WF₆ flow ratio is fixed at 4:1), and the showerhead-wafer gap size. The desired response variable is the film thickness of deposited tungsten defined at a specific spatial resolution over the wafer surface.

3.2.2. Derivation of the model form:

Under isothermal processing conditions, the overall reaction rate can be expressed as the following surface reaction expression [26]:

$$R_{\text{kin}} = k_o [P_{\text{WF}_6}]^0 [P_{\text{H}_2}]^{1/2} \quad (3.1)$$

where,

R_{kin} is the rate of deposition of tungsten

$[P_{\text{WF}_6}]$ is the partial pressure of WF₆

$[P_{\text{H}_2}]$ is the partial pressure of H₂

According to this reaction kinetics model, the reaction rate does not depend on WF₆ partial pressure when sufficient WF₆ is present. However, the reaction rate is assumed to be proportional to the square root of the hydrogen precursor concentration X_{H_2} , so as a first order approximation we have:

$$X_{\text{H}_2} = \frac{P_{\text{H}_2}}{\text{Total pressure } P} \approx \frac{\text{flow of } \text{H}_2 \text{ (sccm)}}{\text{Total flow of precursor (sccm)}} \quad (3.2)$$

Furthermore, in our experiments we should expect a linear relationship between the deposition rate of the W film and $\sqrt{X_{\text{H}_2}}$ when precursor conversion rates are low, and so the square root of H₂ flow to each segment is finally used as input to our model.

As explained in Chapter 2, The SP-CVD reactor has a showerhead with three segments which interact with one another by the following two gas transport mechanisms:

- (1) Intersegment gap diffusion: In this mechanism, process gases diffuse from one segment to the other segments through the gap between the wafer surface and the bottom of the segments owing to the concentration gradients between the segments when different recipes are used in neighboring segments.
- (2) Intersegment back diffusion: In this mechanism, process gases diffuse from the common exhaust volume (CEV) back into the segments owing to gas composition differences between the CEV and individual segments; these differences are attributable to different precursor recipes in the different segments or depletion at high deposition rates.

The showerhead-wafer gap is a process parameter that controls segment to segment interaction in the gap region and is included in the RS model. We derive a model which will predict the entire wafer film thickness profile $W^{pred}(r, \theta)$ (in nm, for a fixed deposition time) based on the following input variables:

$$x_i : \sqrt{H_2 \text{ flow}(sccm)} \text{ to segment } i$$

$$g : \text{wafer} - \text{showerhead gap, mm}$$

Based on the deposition rate expression, and the mechanism of segment to segment interaction through inter-segment gap diffusion and back diffusion from CEV, we intuitively define the properties of the model to satisfy the following requirements:

- 1) The model should be such that it predicts the local thickness under segment i to be proportional to x_i and, to a lesser extent x_j for $i \neq j$ because of back diffusion.

2) Segment i film thickness dependency on x_j is modulated by g for transport to that region by inter segment gap diffusion.

3) No deposition should take place when all $x_i=0$ and the deposition rate should not change with g alone.

Under these assumptions, we arrive at the RS model form to be:

$$W_{pred}(r, \theta) = b_1(r, \theta)x_1 + b_2(r, \theta)x_2 + b_3(r, \theta)x_3 + b_{1,4}(r, \theta)x_1g + b_{2,4}(r, \theta)x_2g + b_{3,4}(r, \theta)x_3g \quad (3.3)$$

To understand this model, consider a spatial point (r', θ') under segment 1; the terms in the expression $b_1(r, \theta)x_1 + b_2(r, \theta)x_2 + b_3(r, \theta)x_3$ are ‘designed’ to satisfy requirement 1, i.e., $W_{pred}(r', \theta')$ would be primarily dependent on x_1 and the coefficient b_1 quantifies this dependency. The terms $b_2(r', \theta')x_2$ and $b_3(r', \theta')x_3$ account for the contribution of back diffusion to the point thickness $W_{pred}(r', \theta')$.

The terms in the expression $b_{1,4}(r, \theta)x_1g + b_{2,4}(r, \theta)x_2g + b_{3,4}(r, \theta)x_3g$ are designed to satisfy requirement 2, i.e. if the spatial point (r', θ') is under segment 1, $W_{pred}(r', \theta')$ also will depend on the intersegment gap diffusion which is captured by the terms $b_{1,4}(r', \theta')x_1g, b_{2,4}(r', \theta')x_2g$, and $b_{3,4}(r', \theta')x_3g$. Finally, the absence of a constant term in equation (3.3) satisfies requirement 3, i.e. when $x_i=0$ and $g=0$, $W_{pred}(r, \theta) = 0$.

The six spatially varying coefficients $b_i(r, \theta)$ and $b_{i,j}(r, \theta)$ are computed from the solution of the least squares procedure using the N experimentally determined thickness maps and corresponding process recipes, where $N > 6$. The unique

computational approach necessary to compute the spatially varying coefficients will be discussed in a separate publication.

3.2.3. Data set to build RSM for design A:

25 wafers were processed for creating the data set from which we derived the RS model. Please note that these wafers comprise the set of wafers listed in Table 1(9 wafers), Table 2 (10 wafers) and the 6 wafers processed at 3mm gap (contributing to the data in Figure 13). These wafers are summarized in Table 3. After each deposition process, film thickness was measured using a 4 point probe (4PP) ex-situ metrology station. As before, we interpolate the 4PP data to a quadrature grid to create a set off “virtual” wafers.

Wafer number	H2 flow S1(sccm)	H2 flow S2(sccm)	H2 flow S3(sccm)	Gap (mm)
1	24	36	48	1
2	48	24	36	1
3	24	36	48	1
4	48	24	36	1
5	36	48	24	1
6	24	36	48	1
7	48	24	36	1
8	36	48	24	1
9	48	24	36	1
10	40	20	40	1
11	40	20	40	1
12	40	20	40	1
13	40	20	40	1
14	40	20	40	1
15	40	20	40	1
16	40	20	40	1
17	40	20	40	1
18	40	20	40	1
19	40	20	40	1
20	24	36	48	3
21	48	24	36	3
22	36	48	24	3
23	24	36	48	3
24	48	24	36	3
25	36	48	24	3

Table 3: Wafers 1 to 25 were used to deposit films from the above recipes (varying flow rates and showerhead-wafer gaps sizes) for generating the data to obtain the RS model for reactor design A. $WF_6:H_2$ flow ratio in each segment is 1:4. Ar flow in each segment is $60-(H_2 \text{ flow} + WF_6 \text{ flow})$ sccm

3.2.4. RS model identification and validation for design A

The six spatially varying coefficients $b_i(r, \theta)$ and $b_{i,j}(r, \theta)$ are computed from the solution of the least squares procedure using the 25 experimentally determined thickness maps and corresponding process recipes. Figure 16 illustrates the comparison between the model's prediction and true measurement for wafers No. 6, 8 and 23 (Table 3). These wafers were processed with the reactor operating in the non-uniformity mode. The RS model was used to predict the segment averaged values which show a good agreement with the true segment averaged values as shown by the bar charts. 10 wafers were processed with the same recipe, operating the reactor in the uniformity mode. This recipe (40 sccm of H₂ in S1 and S3 and 20 sccm of H₂ in S2) was calculated to be the recipe required to produce a thickness of 660 nm in each segment using a linear model. See chapter 2 for details regarding this linear model. The average thickness of these 10 wafers are calculated and illustrated as a wafer map in Figure 16 and compared with the RS model's prediction for the same. The RS model predicts the uniformity in agreement with the measured values to an accuracy of 8% with a standard deviation of 5%. Thus RS models can be effectively used to predict the thickness maps accurately produced by the reactor when operated in both the non-uniformity mode and the uniformity mode.

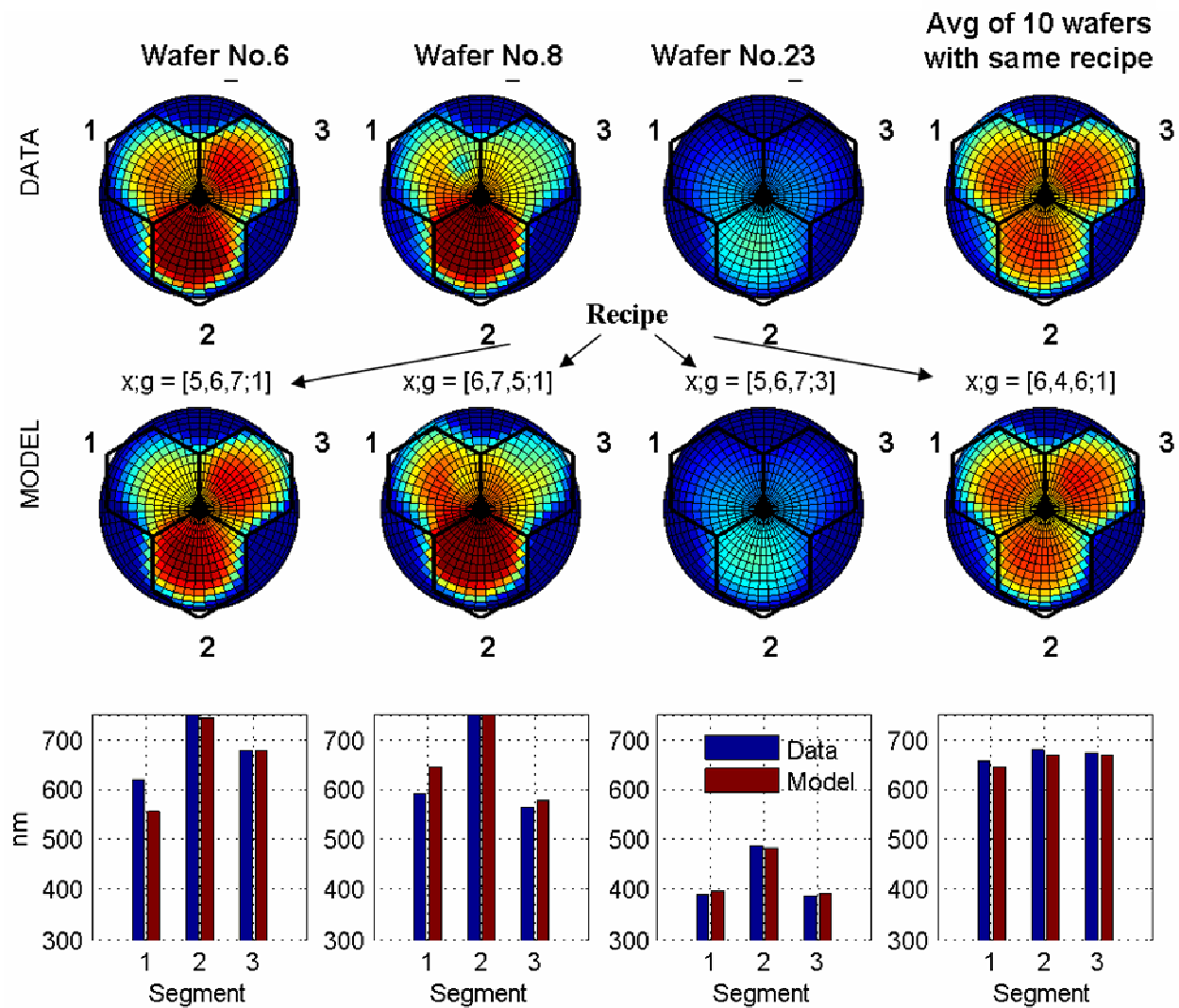


Figure 16: True wafer maps (data) of wafers No.6, No.8 and No.23 (Table 1), and averaged profiles of 10 wafers processed with the same recipe, obtained from 4 point probe measurements and numerically interpolated in MATLAB are shown in the top row. The interpolated data are compared to the maps predicted by the RS model shown in the second row. The third row compares the average thickness for each segment through bar charts. The recipe is written in the format: $[\sqrt{H_2 \text{ flow}(sccm) \text{ in } S1}, \sqrt{H_2 \text{ flow}(sccm) \text{ in } S2}, \sqrt{H_2 \text{ flow}(sccm) \text{ in } S3} \text{ gap}]$

3.3. Performance analysis for design A:

The validated RS model was used to evaluate the original reactor design using the following three criteria:

3.3.1. Sensitivity of film thickness profile to gas flow rate and gap:

Differentiating equation (2) with respect to x_1 we obtain:

$$\frac{\partial W_{pred}(r,\theta)}{\partial x_1} = b_1(r,\theta) + b_{1,4}(r,\theta)g \quad (3.4)$$

Similarly we obtain:

$$\frac{\partial W_{pred}(r,\theta)}{\partial x_2} = b_2(r,\theta) + b_{2,4}(r,\theta)g \quad (3.5)$$

$$\frac{\partial W_{pred}(r,\theta)}{\partial x_3} = b_3(r,\theta) + b_{3,4}(r,\theta)g \quad (3.6)$$

These sensitivity maps with respect to the reactant concentration of gas fed to each segment are calculated for all (r,θ) over the patch of the wafer surface under each segment. Color plots of these patches are found in Figure 17 showing the sensitivity of $W_{pred}(r,\theta)$ in each segment to each x_i with increasing gap size. Two effects are observed here:

- 1) The thickness of film $W_{pred}(r,\theta)$ in each segment patch i is most sensitive to the corresponding x_i . This observation is physically intuitive.

- 2) The sensitivity decreases with increasing gap size because as gap size increases, precursor gases 'escape' into the external chamber volume causing reactant depletion over the wafer surface.

Because of the second of these two observations, design A performs poorly when gap sizes are greater than 3 mm. For large gap sizes, the conversion rates are reduced and programmability of the reactor cannot be exploited for desired uniformity/non-uniformity profiles.

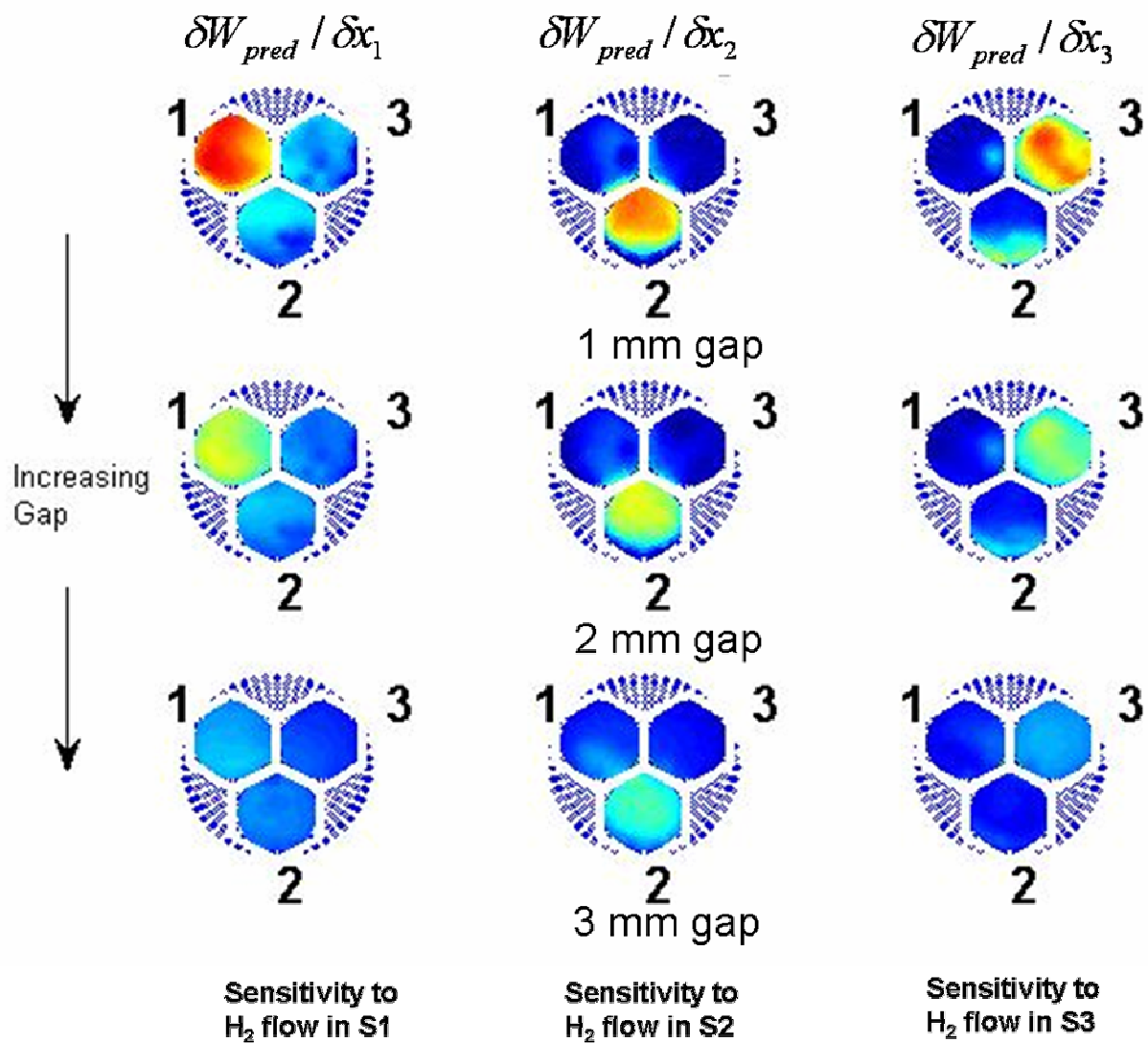


Figure 17: Sensitivity of the reactor to recipe and gap size as predicted by the RS model for design A. The greater the redness of the plot within a segment, the more sensitive that segment is to H_2 flow in that segment. As gap size increases, sensitivity to H_2 flow decreases because with increasing gap, the precursor gases ‘escape’ into the external volume of the chamber.

3.3.2. Range of segment to segment uniformity

With the potential limitations in operating performance for large gap sizes in mind, the RS model is used to predict the range of uniform film thicknesses that can be produced across all segments (i.e., same thicknesses in all three segments) given the fixed range of flow rates allowed by the mass flow controllers (MFCs) for varying gap size. The MFCs for WF₆ have a range from 0 sccm to 12 sccm limiting the H₂ flow range from 0 sccm to 48 sccm. The gap size ranges from 0 to 5 mm.

We define:

W_i^s to be the average thickness for segment i

x_i^s to be the recipe for segment i to achieve W_i^s

S_i to be the segment area , $i = 1,2,3$

We then write out the expression for W_i^s using (3.3) and the above defined terms in compact matrix form as:

$$\begin{bmatrix} W_1^s \\ W_2^s \\ W_3^s \end{bmatrix} = \mathbf{B} \begin{bmatrix} x_1^s \\ x_2^s \\ x_3^s \end{bmatrix} + \mathbf{D}\mathbf{G} \begin{bmatrix} x_1^s \\ x_2^s \\ x_3^s \end{bmatrix} \quad (3.7)$$

where the segment-averaged RS model coefficients are

$$B_{i,j} = \int_{S_i} b_j(r,\theta) ds / \int_{S_i} ds; \quad i, j = 1,2,3, \quad (3.8)$$

$$D_{i,j} = \int_{S_i} b_{j,4}(r,\theta) ds / \int_{S_i} ds; \quad i, j = 1,2,3 \quad (3.9)$$

and the influence of gap size g is included as the matrix

$$\mathbf{G} = \begin{bmatrix} g & 0 & 0 \\ 0 & g & 0 \\ 0 & 0 & g \end{bmatrix} \quad (3.10)$$

To calculate the range of uniformity that can be achieved using the reactor, we use the following steps:

- 1) Set $g=0$ mm, $W^s \rightarrow 0$ (desired uniform thickness)
- 2) Set $W_1^s = W_2^s = W_3^s = W^s$
- 3) Solve equation (3.7) for unknowns x_1^s , x_2^s and x_3^s .
- 4) If x_i^s are valid (positive and below the MFC upper limit), then set $W^s = W^s + \varepsilon_w$ (increment thickness) and return to step 2 i.e., if the unknowns x_1^s , x_2^s and x_3^s are within the acceptable flow range, we return to step 2, increase the value of the desired uniform thickness and recalculate the unknowns in step 3.
- 5) If x_i^s are not valid, then set $g = g + \varepsilon_g$ (increment gap), $W^s \rightarrow 0$ i.e., if the unknowns do not lie between 0 and $\sqrt{48}$ sccm, we conclude that the desired uniform thickness cannot be achieved with the current gap size and mass flow constraints and return to step 1 and increment the gap size provided it is less than 5 mm.
- 6) If $g < 5$ mm, return to step 2.

We thus calculate the maximum value of W^s for a given gap size given the mass flow constraints of the reactor. Figure 18 contains a plot of max W^s vs. gap size. The plot indicates that this reactor can be used to produce uniform films ranging from 0 to 800

nm across all three segments, given the above mentioned range of flow rates. As gap size exceeds ~ 3.4 mm, max W^s reduces to zero. Thus design A is limited to depositing uniform films of thickness < 800 nm and cannot produce segment to segment uniform films for $g > 3.4$ mm. We hypothesize that the curve does not gradually tail off as g grows, but ends abruptly because of segment region asymmetries, such as non-uniform CEV concentration or heater hot spots.

In Chapter 2 we concluded that we could not identify a uniformity producing recipe for a 3mm gap case. But from Figure 18, we see that there is a range of W^s that can be achieved for $g = 3$ mm. We attribute this difference in this conclusion for uniformity at $g = 3$ mm is due to the fact that in Chapter 2 the relatively simpler linear model is not accurate enough to predict deposition thicknesses. (The linear model uses an average measure of thickness over the entire segment area on the wafer surface and it does not take segment to segment interaction into account. Segment to segment interaction is significant at higher gaps.). According to the RS model in this chapter, we can produce uniform films up to 300nm thick at $g = 3$ mm.

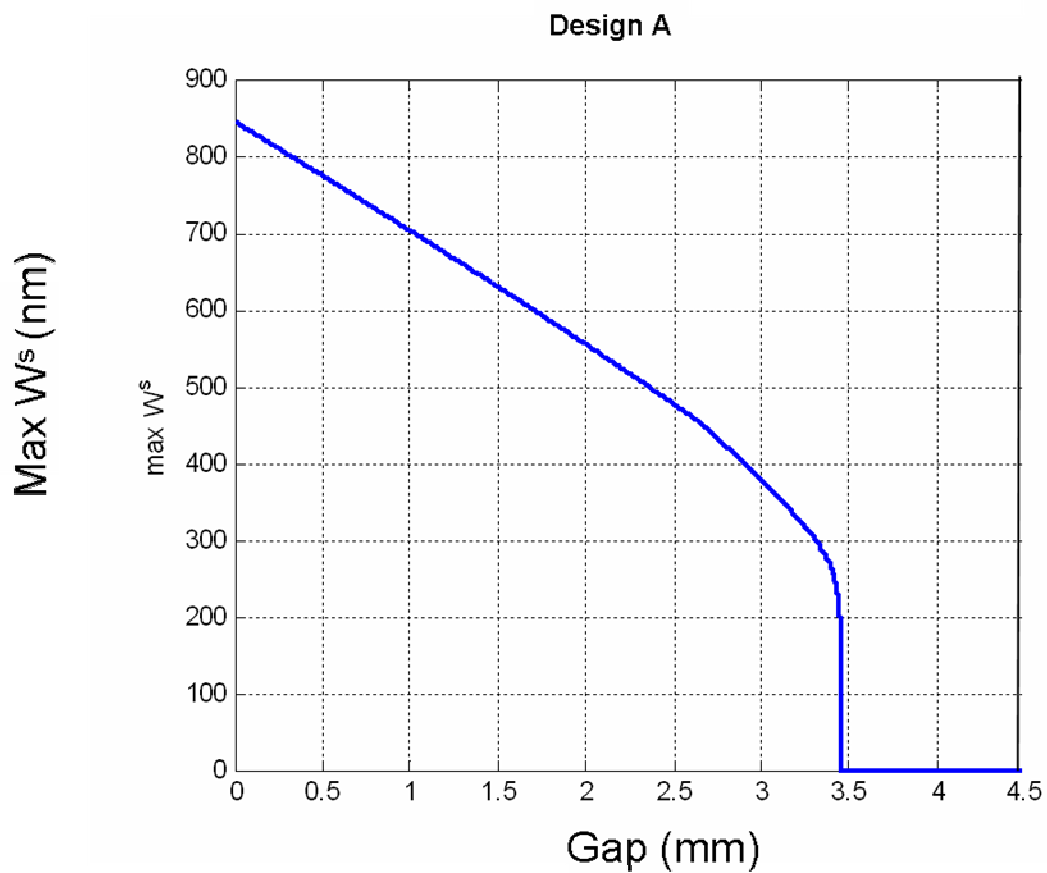


Figure 18: The range of uniformity control possible for the design A as predicted by the RS model. This plot conveys that this reactor design could be used to deposit uniform films ranging from 0 to 800 nm using gap sizes ranging from 0 to 3 mm, with WF_6 flow rates ranging from 0 to 12 sccm in each segment (limited by the MFCs) and H_2 flow rates in each segment ranging from 0 to 48 sccm (to maintain the stoichiometric ratio of 1:4 $WF_6:H_2$). Ar flow in each segment is 60- $(H_2 \text{ flow} + WF_6 \text{ flow})$ sccm.

3.3.3. Gradient control performance

The programmable reactor can be used to produce wafers with a deliberate thickness gradient across segment regions. To demonstrate this ability, we define a set point film gradient over a subset of the wafer by defining a line of length s_m on the wafer surface starting at point S1 and ending on S3 (Figure 19). The segment wall separating S1 and S3 bisects this line. We define the desired thickness gradient along this line $W_{set}(s)$ by the following equation:

$$W_{set}(s) = \frac{2s - s_m}{s_m} W_m \delta_m + W_{avg} \quad (3.11)$$

where

$0 \leq s \leq s_m$, W_{avg} is the mean thickness along the gradient defined by the user in nm, and W_m is the difference between the values of the thickness at the two extremities of the gradient and the centre point, defined by the user in nm.

δ_m is a tuning parameter that varies from -1 to 1. This parameter is used so that equation (3.11) represents all possible linear thickness gradients from S1 to S3 over the length s . Consider, for example,

$$W_{set}(s) = -\left(\frac{2W_m}{s_m}\right)s + (W_{avg} + W_m) \text{ when } \delta_m = -1 \text{ (maximum negative gradient)} \quad (3.12)$$

$$W_{set}(s) = W_{avg} \text{ when } \delta_m = 0 \text{ (flat profile)} \quad (3.13)$$

$$W_{set}(s) = \left(\frac{2W_m}{s_m}\right)s + (W_{avg} - W_m) \text{ when } \delta_m = +1 \text{ (maximum positive gradient)} \quad (3.14)$$

Equation (3.12) is the equation of a line with negative slope implying that the desired film thickness $W_{set}(s)$ decreases from S1 to S3 in a linear fashion. Equation (3.13) is

the equation of a horizontal line, implying that the desired film thickness remains constant at W_{avg} nm from S1 to S3. Finally, equation (3.14) is an equation of a line with a positive slope, implying that the desired film thickness increases from S1 to S3 in a linear fashion. All other values of δ_m between -1 and 1 represent the remaining gradients between $-\left(\frac{2W_m}{s_m}\right)$ and $+\left(\frac{2W_m}{s_m}\right)$ respectively.

In each of the above cases, we set the thickness gradient over any desired target circular patch on the wafer surface, as shown in Figure 19. The gradient along one axis of the patch is defined by (3.11), while along the orthogonal axis the gradient is set to zero resulting in a flat tilted circular set point patch, $W_{set}(r, \theta)$. Our objective is to calculate a recipe that when inserted into the RS model gives $W_{pred}(r, \theta)$ that matches $W_{set}(r, \theta)$ over the entire target patch as accurately as possible. This can be stated as the following optimization problem:

$$\min_{g, x} \|W_{pred}(r, \theta) - W_{set}(r, \theta)\| \quad (3.15)$$

$$\text{subject to } 0 \leq x_i \leq 7(\text{sccm})^{0.5} \quad i = 1, 2, 3$$

$$0 \leq g \leq 5\text{mm}$$

We define the objective function by numerically computing the norm of the difference between the computed wafer profile in the patch region and the set point; we use the built-in optimization routine ‘fmincon’ in MATLAB to solve the constrained optimization problem (3.15).

Figure 19a, b and c illustrate the $W_{set}(s)$ and $W_{pred}(s)$ as thickness maps over the patch area when δ_m equals -1, 0 and 1 respectively. The parameter O_v is the value of the expression $\|W_{pred}(s) - W_{set}(s)\|$ at the end of the optimization.

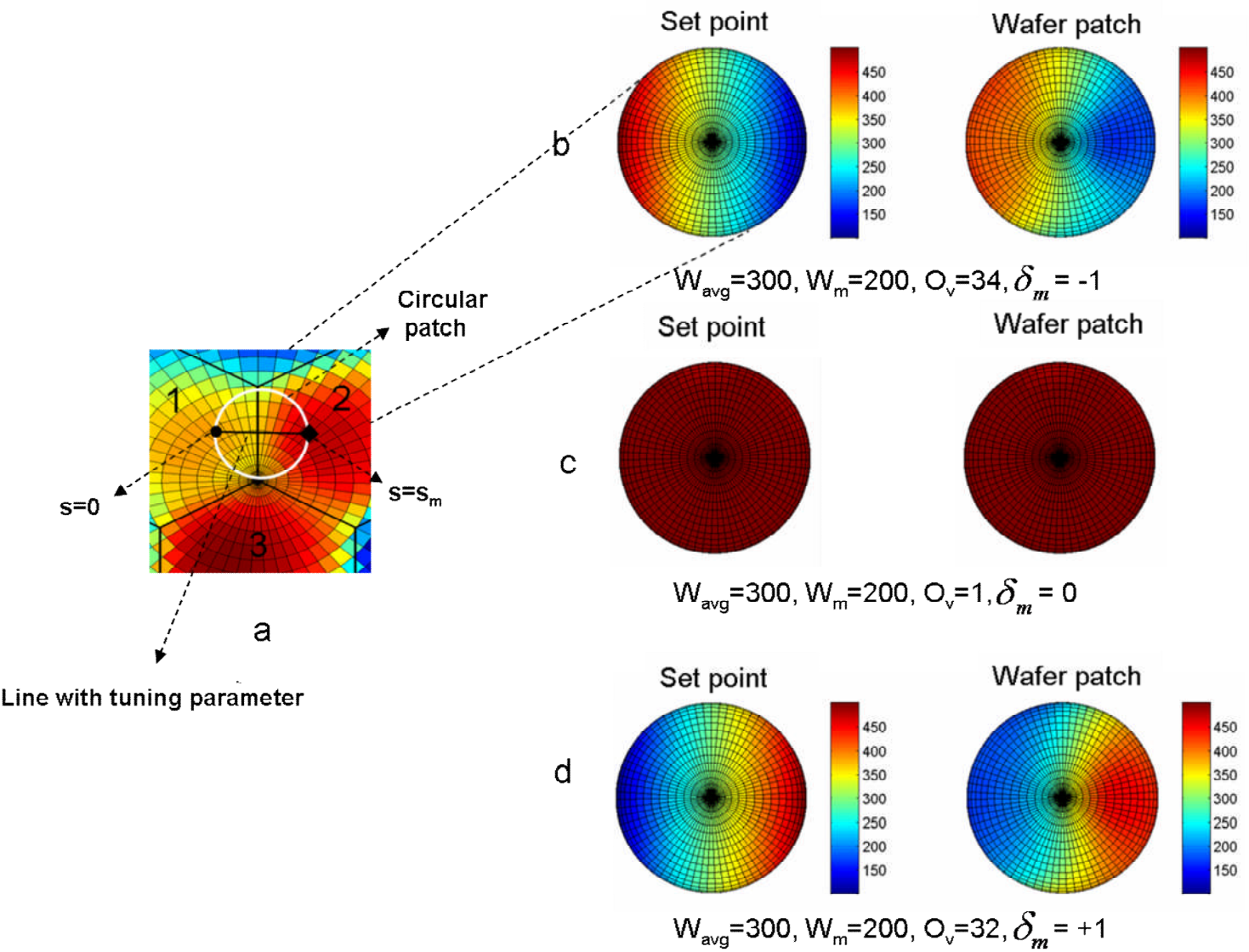


Figure 19: Gradient control for design A for three cases of δ_m values (-1, 0 and 1). The value of the minimized objective function O_v at the end of the optimization routine is shown below the plots in each case. W_{avg} , W_m and O_v in nm.

Figure 20a illustrates the gradient across the circular patch extending from S1 to S3 obtained for different values of δ_m . Plots of the x_i , g , and O_v computed as solutions to (14) as a function of δ_m are shown in plots 6b and 6c respectively. When $\delta_m = -1$ our set point corresponds to a film profile that is thickest under S1 and thinnest under S3 on the defined circular patch. Intuitively, we would predict that x_1 should be higher than x_3 . The optimization routine computes a recipe which confirms our intuition. Figure 20b illustrates this recipe with $x_1 \sim 5$ (sccm)^{0.5}, with $x_2 \sim 0$ (sccm)^{0.5} and $x_3 \sim 0$ (sccm)^{0.5}. Intuitively, to maintain a steep thickness gradient we would expect to use a small gap size. The optimization routine arrives at gap size ~ 0 mm (Figure 6b) to achieve this desired gradient.

When $\delta_m = 0$, our set point corresponds to a film profile that is flat from S1 to S3. Intuitively, we would predict that $x_1 \sim x_3$. Figure 6b illustrates this recipe with x_1 , x_2 and $x_3 \sim 2$ (sccm)^{0.5}. However the gap size is 0 mm. Intuitively we would expect a larger gap size for flat profiles, but because design A yields very poor conversion rates with large gap sizes, the RS model used in the optimization routine ‘recommends’ a small gap size even for flat profiles.

When $\delta_m = 1$, the target film profile is thickest under S3 and thinnest under S1 on the defined circular patch. Intuitively, we would predict that x_3 should be higher than x_1 using a smaller gap size. The optimization routine computes this recipe to be $x_1 \sim 0.5$ (sccm)^{0.5}, $x_2 \sim 5$ (sccm)^{0.5}, and $x_3 \sim 4$ (sccm)^{0.5} (Figure 6b) with a gap size of ~ 0 mm.

Thus the RS model was effectively be used to identify recipes to achieve desired thickness gradients on wafer. O_v as low as ~ 1 nm when δ_m equaled 0, with a mean of

16 nm over all δ_m was achieved. Roughly speaking, this is approximately 5% error in achieving our set point profile, implying a very good gradient control.

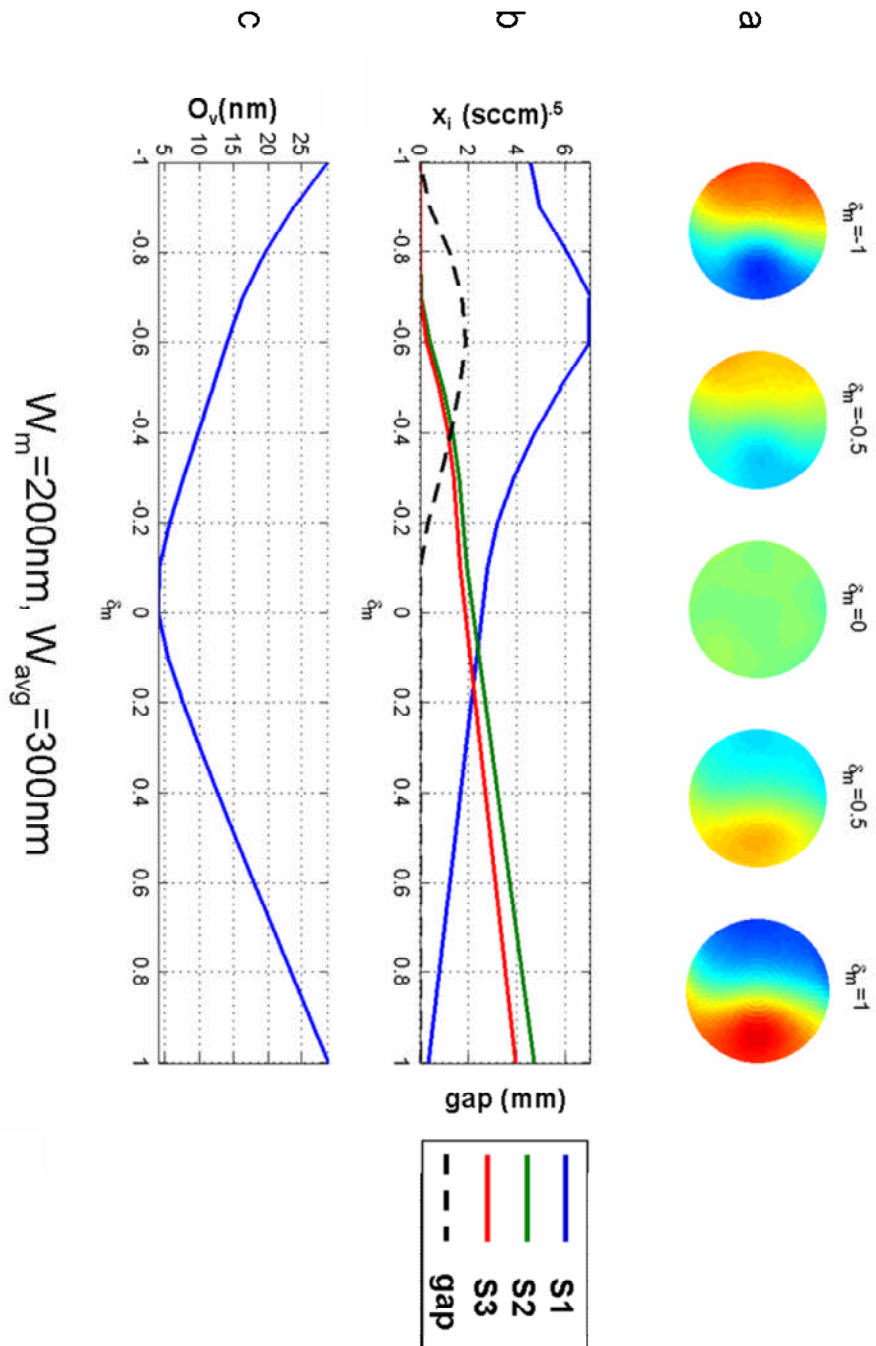


Figure 20: Evaluation of gradient control across segments 1 and 3 as a function of δ_m using the RS model for design A.

Chapter 4: The mini reactor (Design B)

4.1. Disadvantages of design A

The analysis using the RS model for design A revealed the following drawbacks:

- 1) Gap sizes > 3 mm cannot be used because precursor gases escape into the larger chamber volume resulting in poor conversion rates. Smaller precursor flow rates would further lower the conversion rate. The use of design A for combinatorial Atomic Layer Deposition (ALD), a future research direction, requires minute quantities of precursors pulsed into the reactor. Most of these pulses would escape into the larger chamber volume resulting in a very poor growth rate. This drawback calls for a smaller chamber volume.
- 2) The maximum thickness that can be uniformly deposited in all three segments is ~ 800 nm. A smaller chamber volume would improve conversion rates and thicker uniform films can be deposited.

Owing to the above drawbacks of design A, it was decided to design, construct and implement a smaller chamber (called a mini chamber in Figure 21) volume. In this chapter, we refer to the SP-CVD reactor with the mini chamber as design B. The mini chamber was constructed from aluminum and comprised of two parts. 1) The main mini chamber and 2) the lid with appropriately shaped holes through which the segments pass. Figure 21 illustrates a schematic of design B. The mini chamber seats around the heater and the wafer. The lid rests on small screws drilled horizontally into the segment walls 120 degrees apart. The clearance between the outer segment walls and the inner walls of the mini chamber is 0.38 mm. After a wafer is transferred to the

wafer lifter by a wafer holder from the load lock chamber and lowered onto the heater, the segments are lowered. The lid of the mini chamber then rests on the upper lip of the mini chamber while the segments continue to be lowered closer to the wafer. With the lid resting on the mini chamber, the segment-wafer gap can be varied from a minimum of 0 mm to a maximum of 10 mm. The mini chamber together with the lid enclosed the wafer in a cylindrical volume of diameter ~ 106 mm and a height of ~ 10.5 mm which is considerably smaller than the chamber volume in design A.

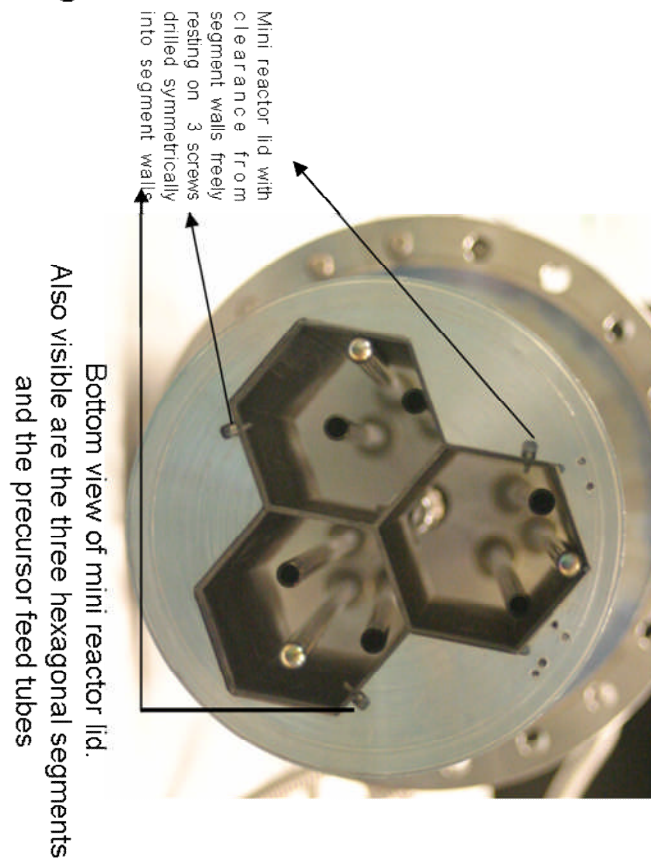
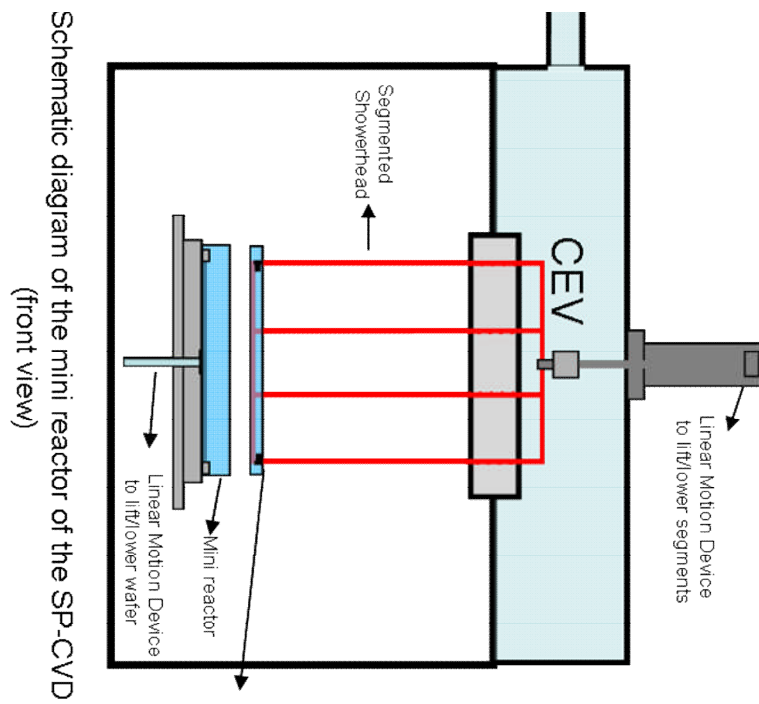


Figure 21: Schematic front view of Design B and photograph of bottom view of mini reactor lid. When the segments are lowered, the lid is stopped by the wall of the mini chamber while the segments continue to be lowered to the desired segment-wafer gap. This design renders a chamber with a reduced volume and overcomes drawbacks of design A

4.2. Modeling for design B

4.2.1. Data set to build RSM for design A:

28 wafers were processed to create the data set from which we derived the RS model. Table 4 summarizes this data set. Pre-process cleaning, process temperature, pressure, and post process metrology and numerical interpolation techniques remained the same as they were for design A.

4.2.2. RS model identification and validation for design B

The six spatially varying coefficients $b_i(r, \theta)$ are computed in the same manner as they were computed for design A using the 28 experimentally determined thickness maps and corresponding process recipes.

Figure 22 illustrates the comparison between the model's prediction and true measurement for wafers No 2, 11, 13 and 22 (Table 4). These wafers were processed with the reactor operating in the non-uniform mode.. The RS model predicts the uniformity in agreement with the measured values to an accuracy of 14% with a standard deviation of 8%. Compared to the design A, the films deposited by design B are 3-4 times thicker. Design B confines more precursor gases over the wafer surface and improves reactant conversion by as much as 400%. However model accuracy appears to be lower than design B.

Wafer number	H2 flow S1(sccm)	H2 flow S2(sccm)	H2 flow S3(sccm)	Gap (mm)
1	16	32	48	3
2	48	16	32	3
3	32	32	32	3
4	32	0	0	3
5	0	32	0	3
6	0	0	32	3
7	0	0	32	1
8	0	32	0	1
9	32	0	0	1
10	48	16	32	1
11	32	48	16	1
12	16	32	48	1
13	16	32	48	5
14	32	48	16	5
15	32	32	32	5
16	32	0	0	5
17	0	32	0	5
18	0	0	32	5
19	0	0	32	3
20	0	32	0	3
21	32	0	0	3
22	32	32	32	3
23	48	16	32	3
24	32	48	16	3
25	16	32	48	3
26	0	0	32	2
27	0	32	0	2
28	32	0	0	2

Table 4: Wafers 1 to 28 were used to deposit films from the above recipes (varying flow rates and showerhead-wafer gaps sizes) for generating the data to obtain the RS model for design B. $WF_6:H_2$ flow ratio in each segment is 1:4. Ar flow in each segment is $60-(H_2 \text{ flow} + WF_6 \text{ flow})$ sccm

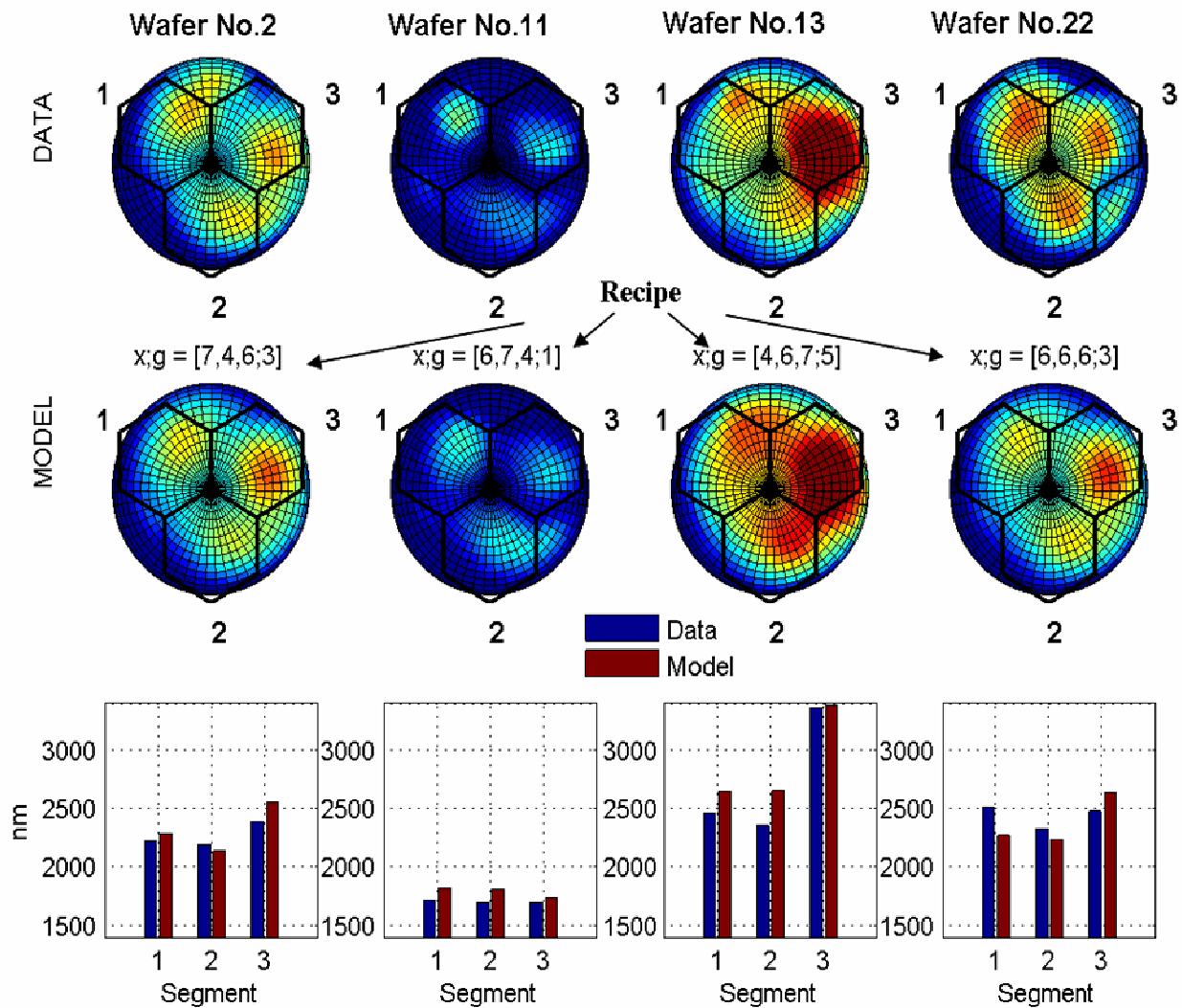


Figure 22: True wafer maps (data) of wafers No.2, No.11, No.13 and No.22 (Table 2), obtained from 4 point probe measurements and numerically interpolated in MATLAB are shown in the top row. They are compared with the predicted maps by the RS model for the same shown in the second row. The third row compares the average thickness for each segment through bar charts. The recipe is written in the format:

$$\left[\sqrt{H_2 \text{ flow}(sccm) \text{ in } S1}, \sqrt{H_2 \text{ flow}(sccm) \text{ in } S2}, \sqrt{H_2 \text{ flow}(sccm) \text{ in } S3} \quad \text{gap} \right].$$

4.3. Performance analysis for design B:

The validated RS model was used to evaluate design B for the same three performance criteria used to evaluate the reactor design A.

4.3.1. Sensitivity to gap size

The RS model captures the sensitivity of the mini reactor to x_i and gap through the color plots in Figure 23. The inferences from the plots are:

- 1) As with design A, the thickness of film $W_{pred}(r, \theta)$ in each segment is most sensitive to the corresponding x_i calculated for that segment.
- 2) This sensitivity does not decrease significantly with increasing gap size because the mini chamber in design B confines the gases preventing their escape to the main chamber as in design A. The slight decrease in sensitivity is attributed to the intersegment diffusion that is facilitated by increasing gap size.

4.3.2. Range of segment to segment uniformity

The range of uniformity that can be achieved using design B was calculated using the same procedure used for design A. Figure 24 shows a plot of $\max W^s$ vs. gap size for both design A and the design B. The plot indicates that the design B can be used to produce uniform films across all three segments ranging from 0 to 1800 nm, given the earlier mentioned range of flow rates. Design B can thus be used to produce uniform films at a rate 2 to 3 times that of design A.

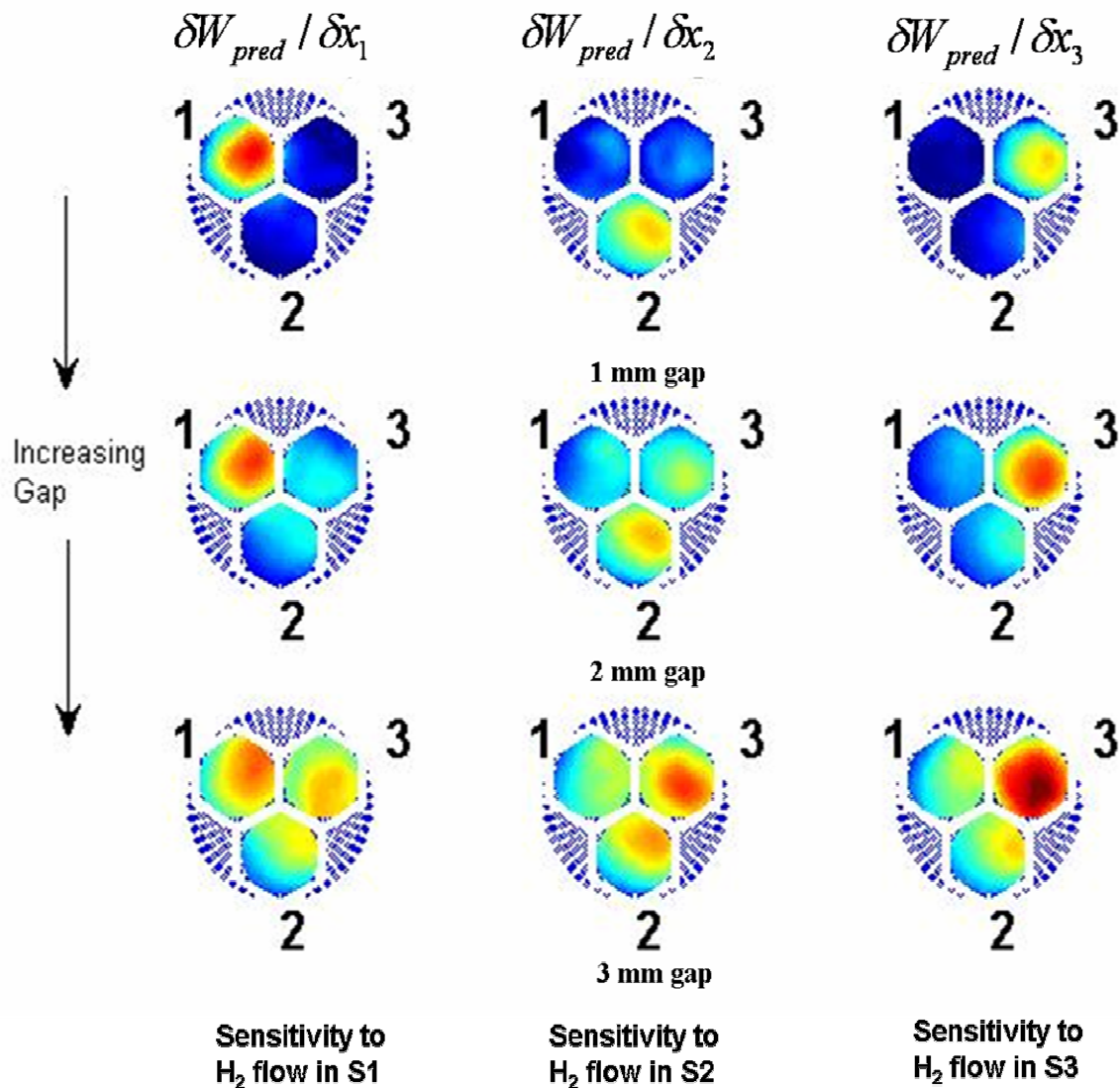


Figure 23: Sensitivity of the reactor to recipe and gap size as predicted by the RS model for design B. The greater the redness of the plot of the plot within a segment the more sensitive that segment is to H₂ flow in that segment. As gap size increases, sensitivity to H₂ flow does not decrease as in design A because the mini reactor design minimizes the gases escaping into the larger chamber volume.

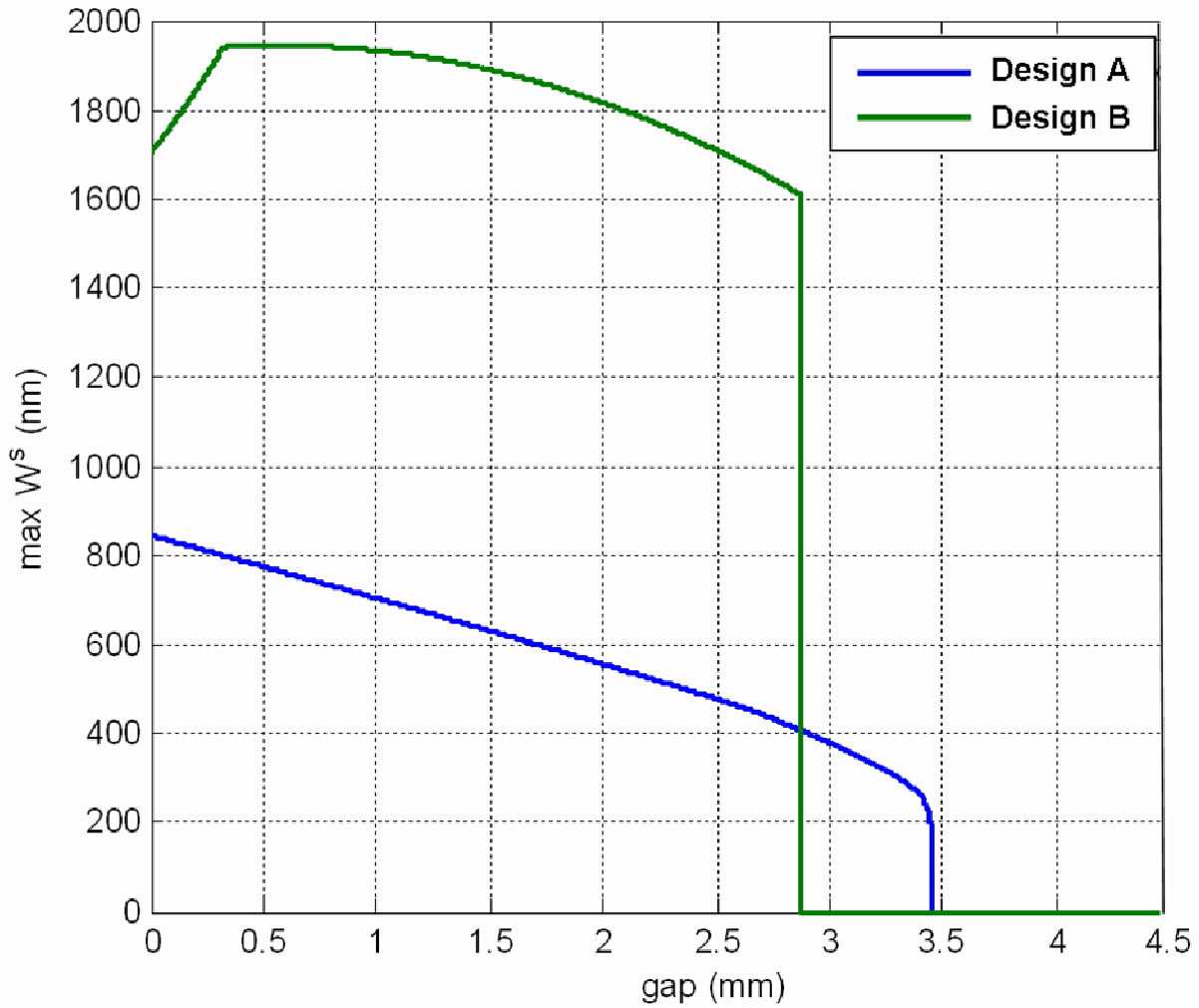


Figure 24: The range of uniformity control possible for the design A vs. design B as predicted by the RS model. This plot indicates that design B could be used to deposit uniform films ranging from 0 to 1800 nm using gap sizes ranging from 0 to 2.5 mm, with WF_6 flow rates ranging from 0 to 12 sccm in each segment (limited by the MFCs) and H_2 flow rates in each segment ranging from 0 to 48 sccm (to maintain the stoichiometric ratio of 1:4 $WF_6:H_2$). Ar flow in each segment is $60 - (H_2 \text{ flow} + WF_6 \text{ flow})$ sccm.

4.3.3. Gradient control performance

We defined and solved the gradient optimization problem for design B using the same approach used for design A. Figures Figure 25a, b and c illustrate the $W_{set}(s)$ and $W_{pred}(s)$ when δ_m equals -1, 0 and 1 respectively while Figure 26 illustrates optimized profiles and plots between δ_m vs. x_i , δ_m vs. gap and δ_m vs. O_v .

When $\delta_m = -1$ the optimization routine computes a recipe (Figure26b) with $x_1 \sim 2.5$ (sccm)^{0.5}, $x_2 \sim 0$ (sccm)^{0.5} and $x_3 \sim 0$ (sccm)^{0.5}. The optimization routine recommends a gap size ~ 0 mm to achieve this desired gradient.

When $\delta_m = 0$, the optimization routine computes a recipe (Figure 26b) with $x_1 \sim 0.5$ (sccm)^{0.5}, with $x_2 \sim 1.5$ (sccm)^{0.5} and $x_3 \sim 0$ (sccm)^{0.5} with a gap size ~ 5 mm. This confirms our intuition that we would expect a larger gap size for flat profiles.

When $\delta_m = 1$, the optimization routine computes this recipe to be, $x_1 \sim 0$ (sccm)^{0.5}, $x_2 \sim 0$ (sccm)^{0.5} and $x_3 \sim 5$ (sccm)^{0.5} (Figure 26b) with a gap size of ~ 1 mm. Comparing Figure 20 with Figure 26 we see that design B requires $\sim 50\%$ smaller flow rates of precursor gases (defined by x_i) than design A for the same thickness gradient. Figures 27- 34 compare the recipes predicted by the RS model for Design A and Design B for several cases of W_m and W_{avg} .

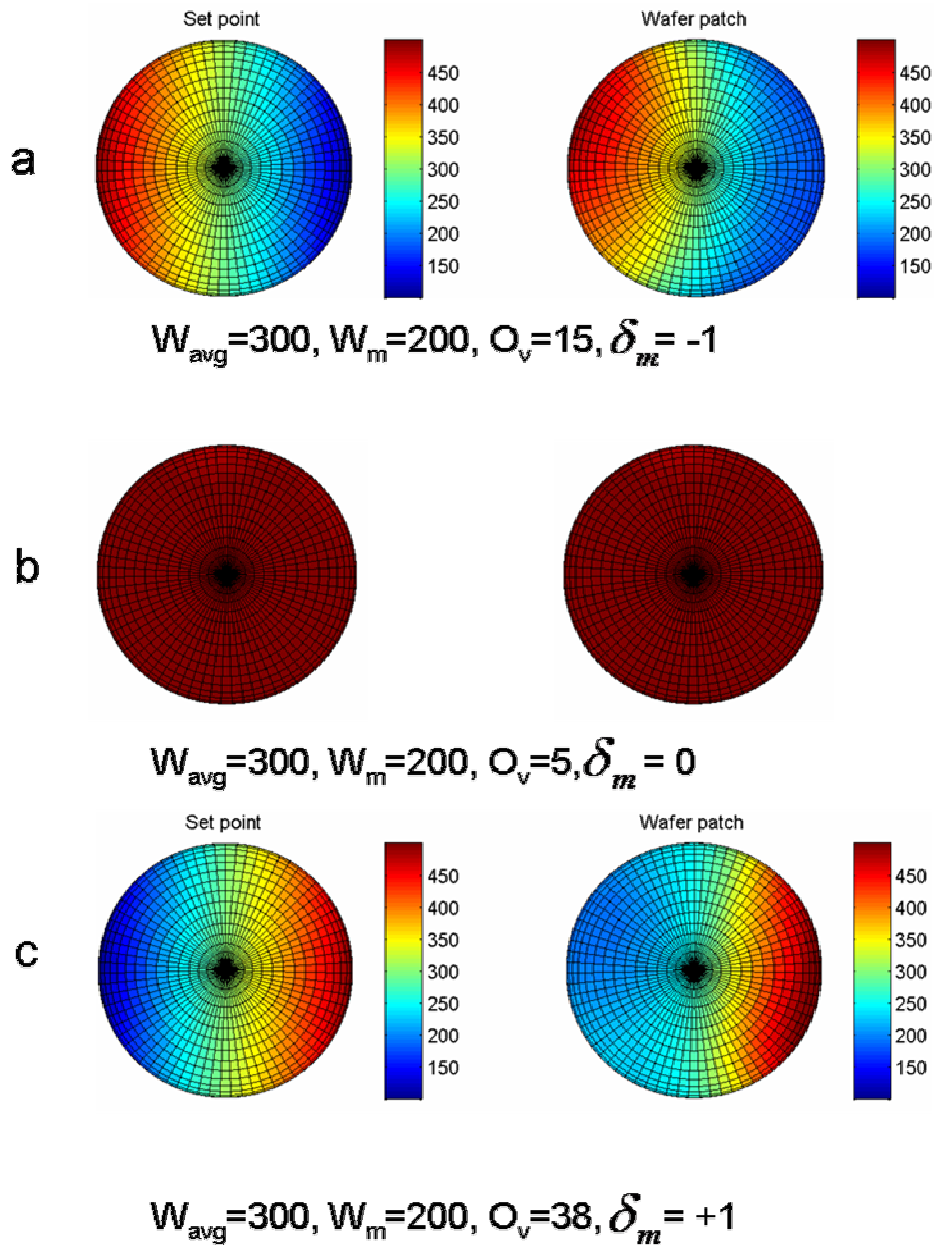


Figure 25 Gradient control for design B for three cases of δ_m values (-1, 0 and 1). The value of the minimized objective function O , at the end of the optimization routine is shown below the plots in each case. W_{avg} , W_m and O_v in nm.

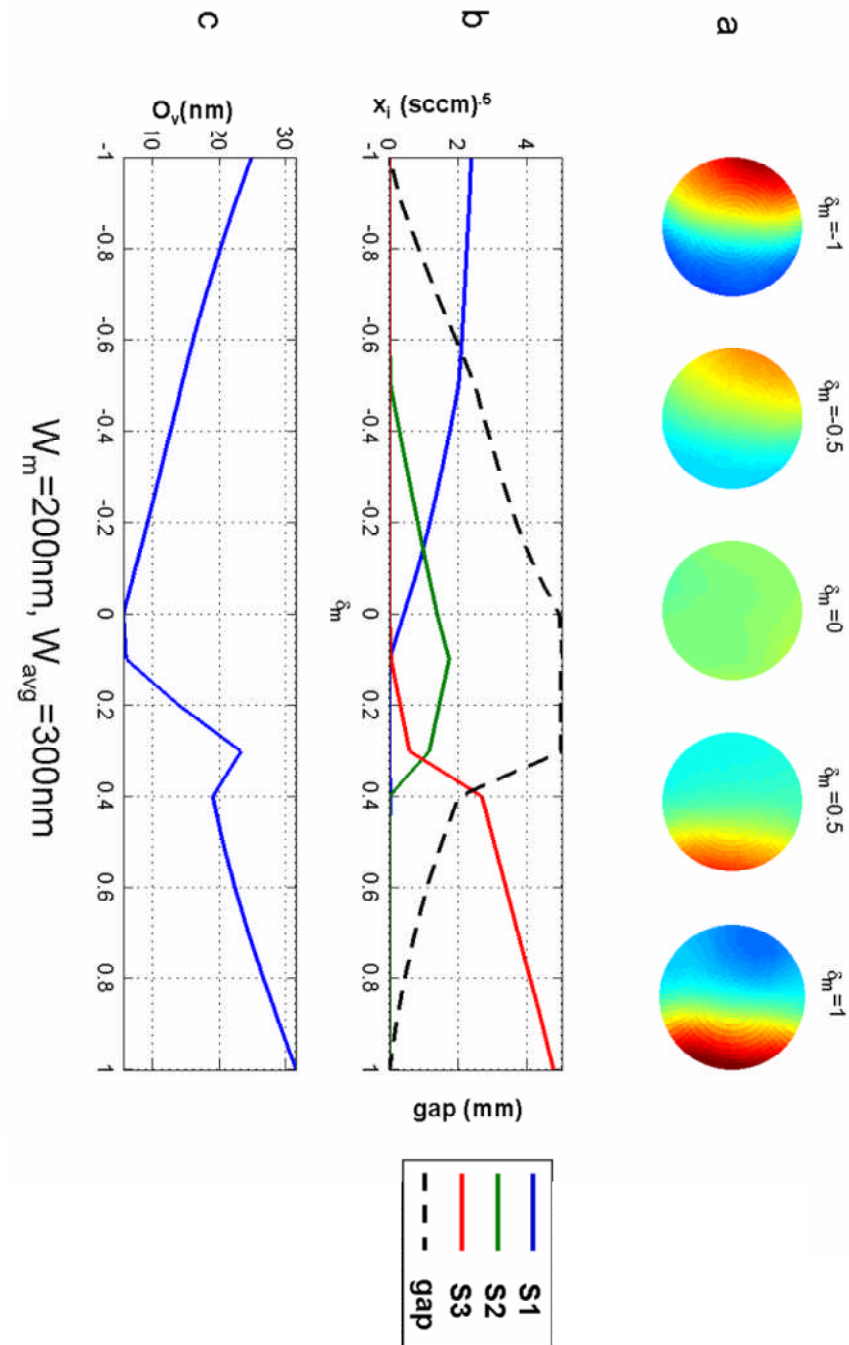


Figure 26: Evaluation of gradient control across segments 1 and 3 as a function of δ_m using the RS model for design B.

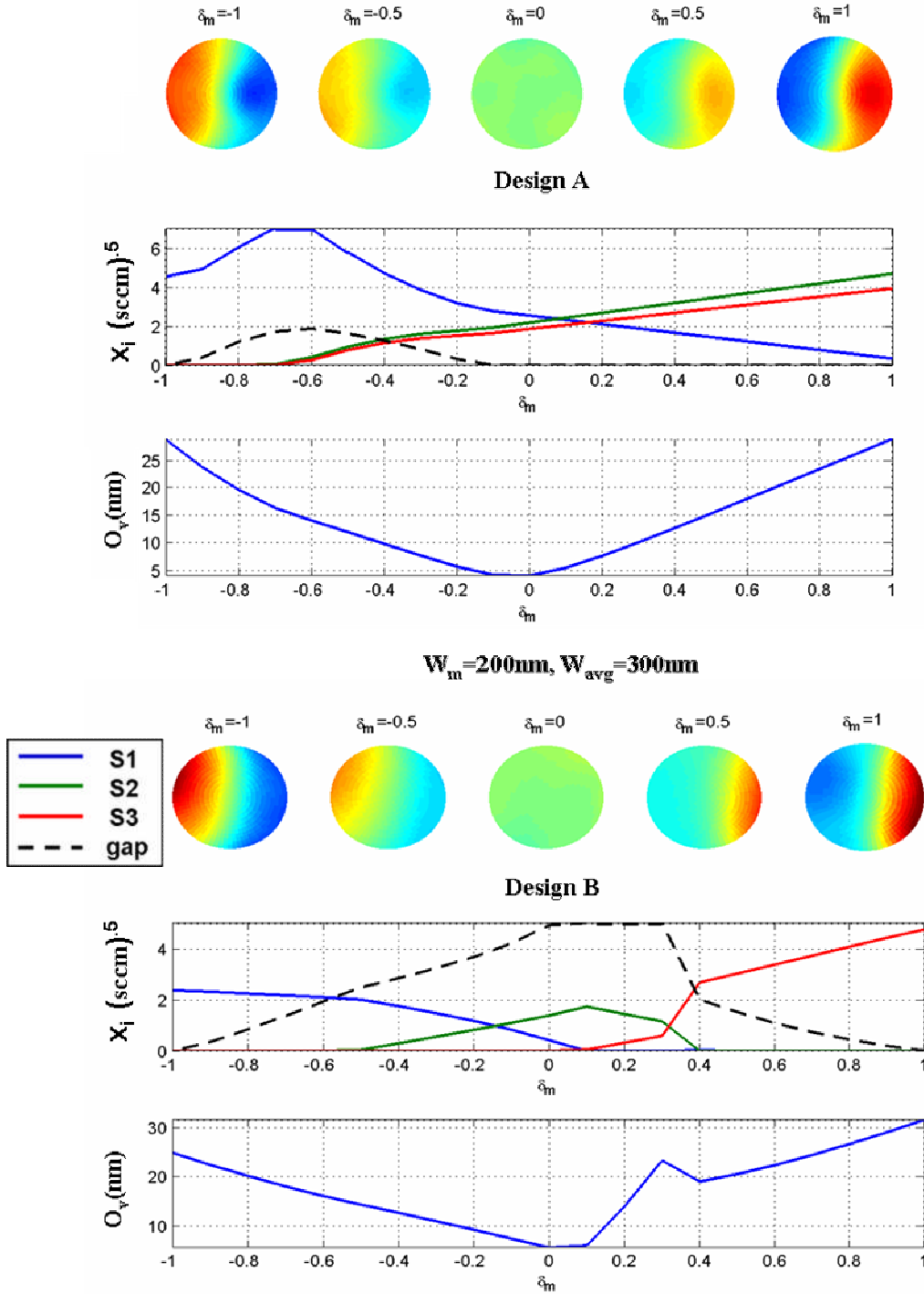


Figure 27: Design A vs. Design B Comparison for $W_m = 200 \text{ nm}$ and $W_{\text{avg}} = 300 \text{ nm}$.

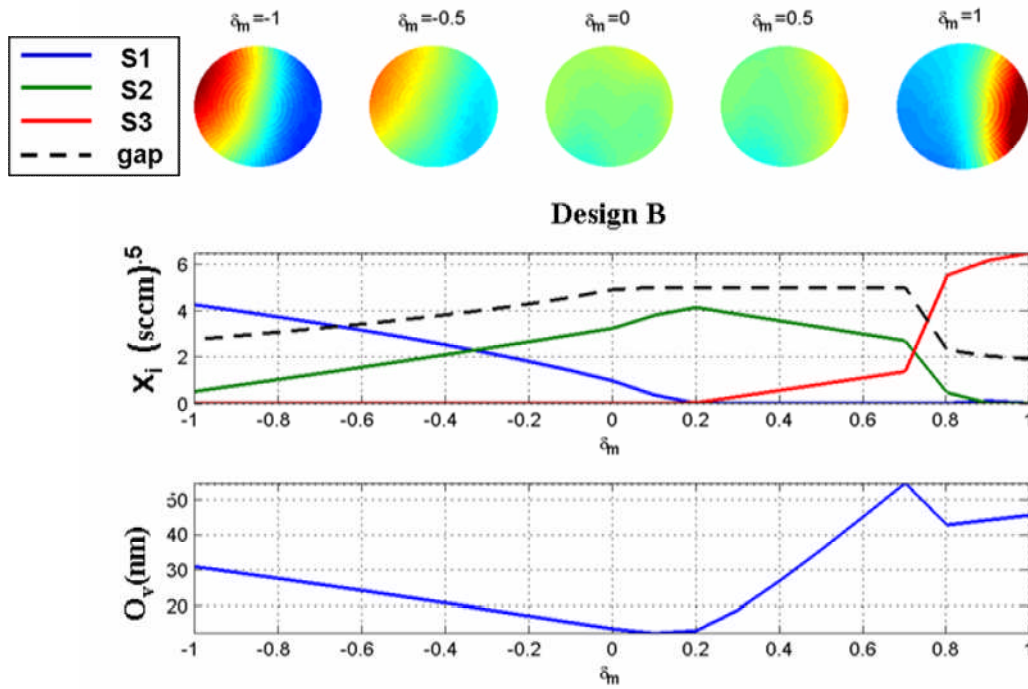
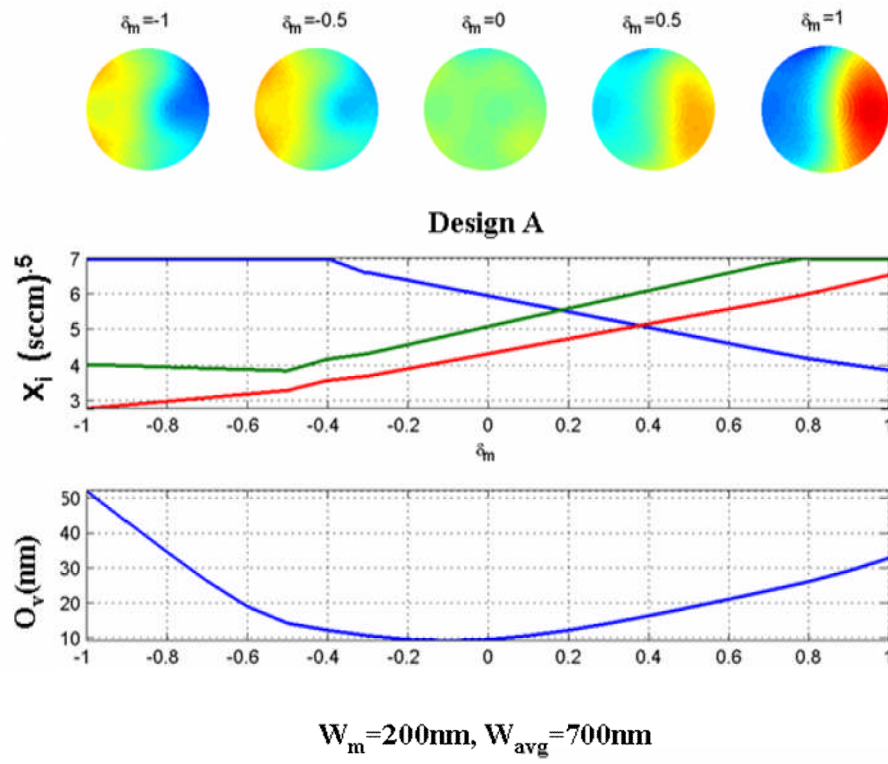


Figure 28: Design A vs. Design B Comparison for $W_m = 200\text{ nm}$ and $W_{\text{avg}} = 700\text{ nm}$.

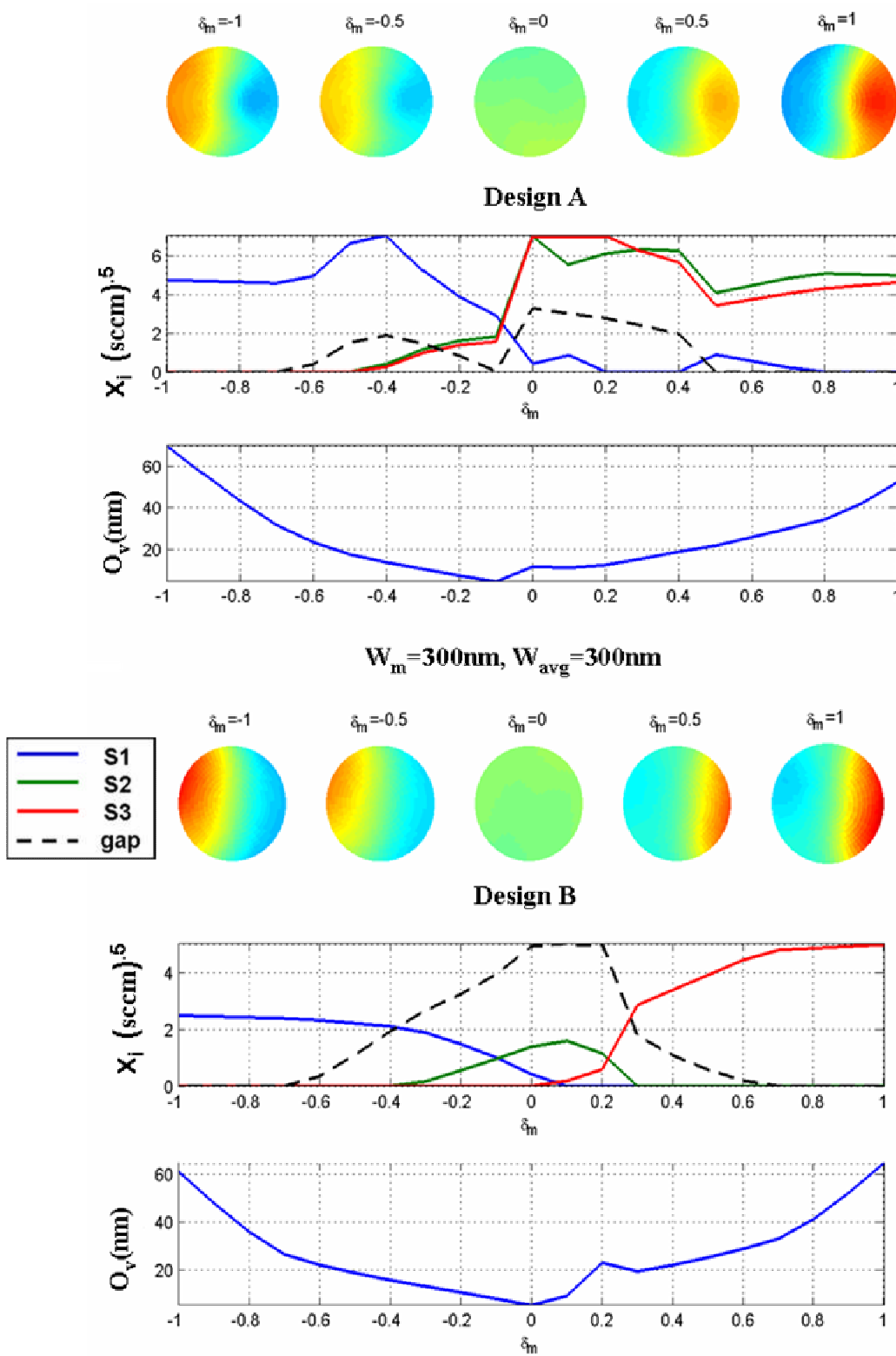


Figure 29: Design A vs. Design B Comparison for $W_m = 300 \text{ nm}$ and $W_{\text{avg}} = 300 \text{ nm}$.

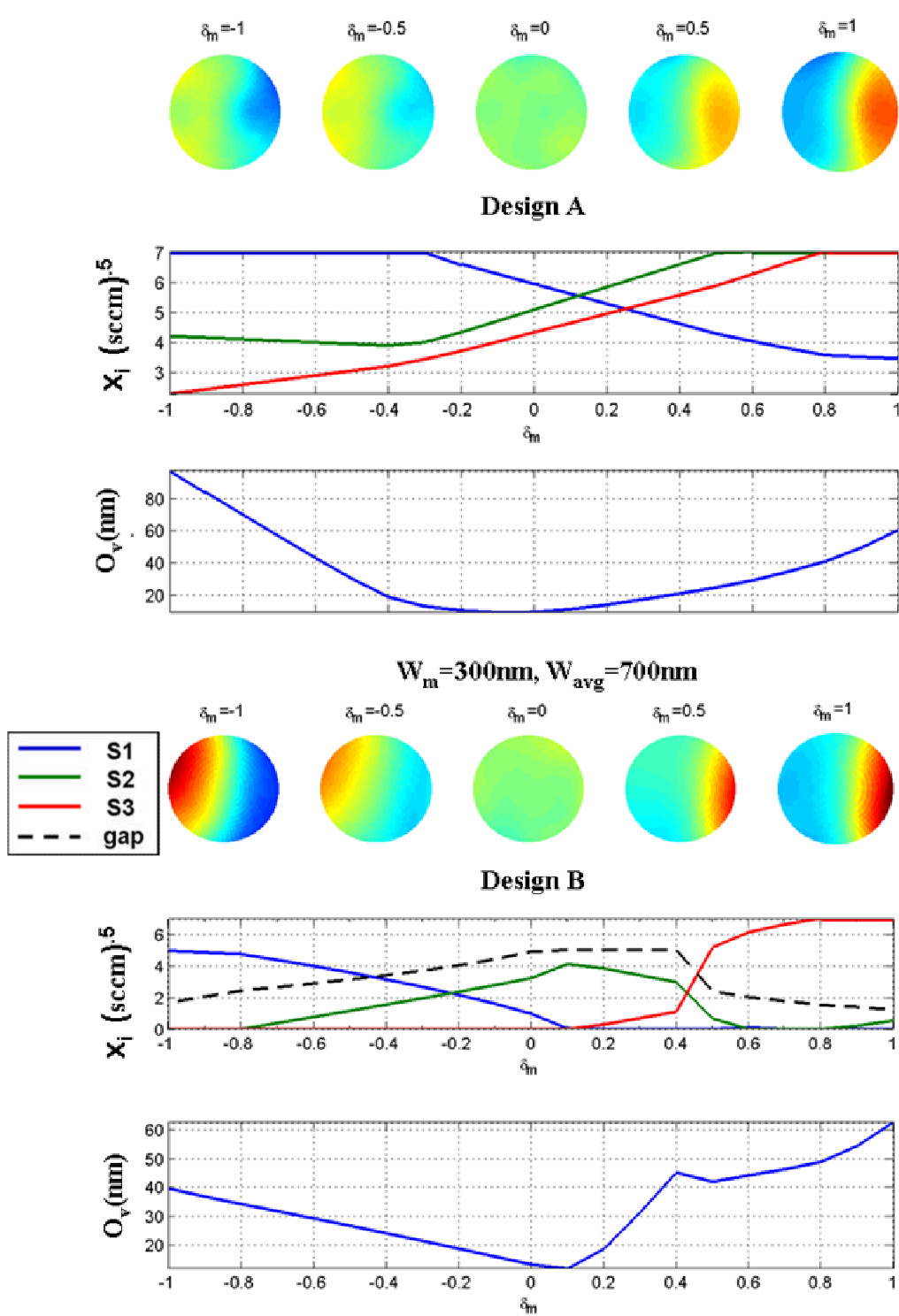


Figure 30: Design A vs. Design B Comparison for $W_m = 300 \text{ nm}$ and $W_{\text{avg}} = 700 \text{ nm}$.

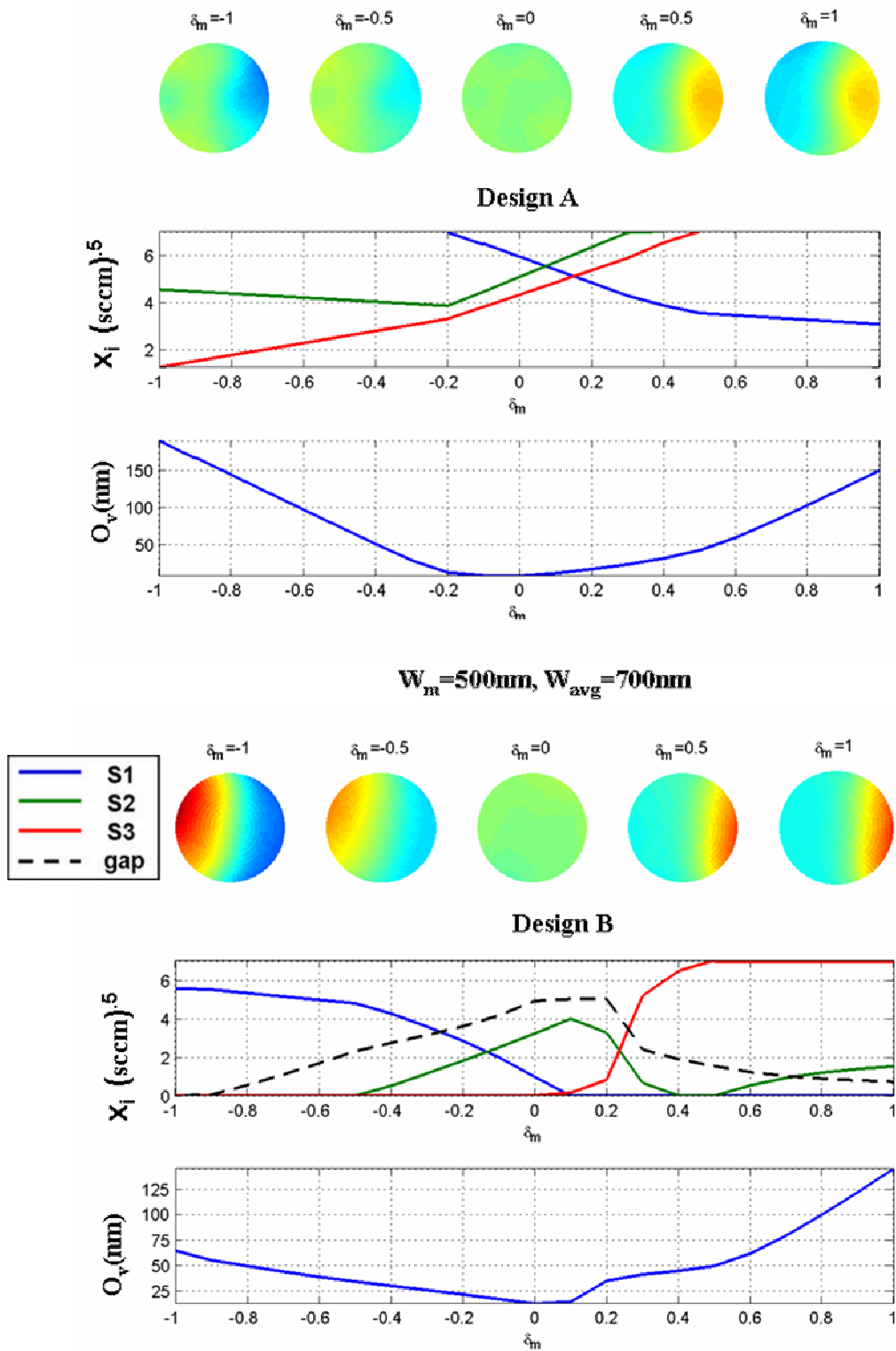


Figure 31: Design A vs. Design B Comparison for $W_m = 500 \text{ nm}$ and $W_{\text{avg}} = 700 \text{ nm}$.

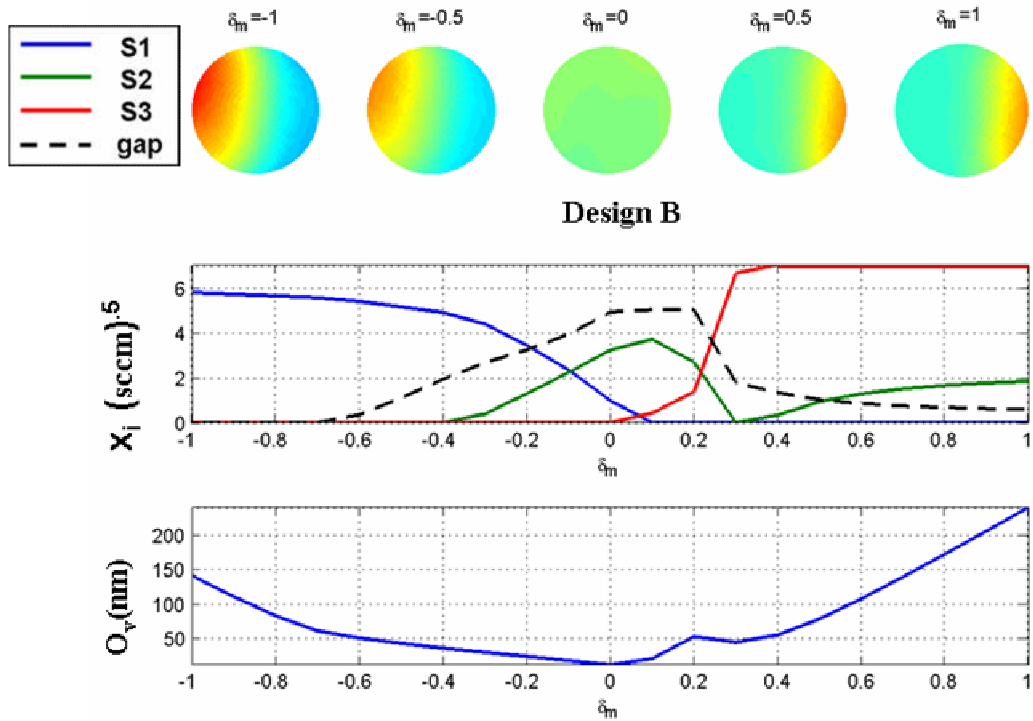
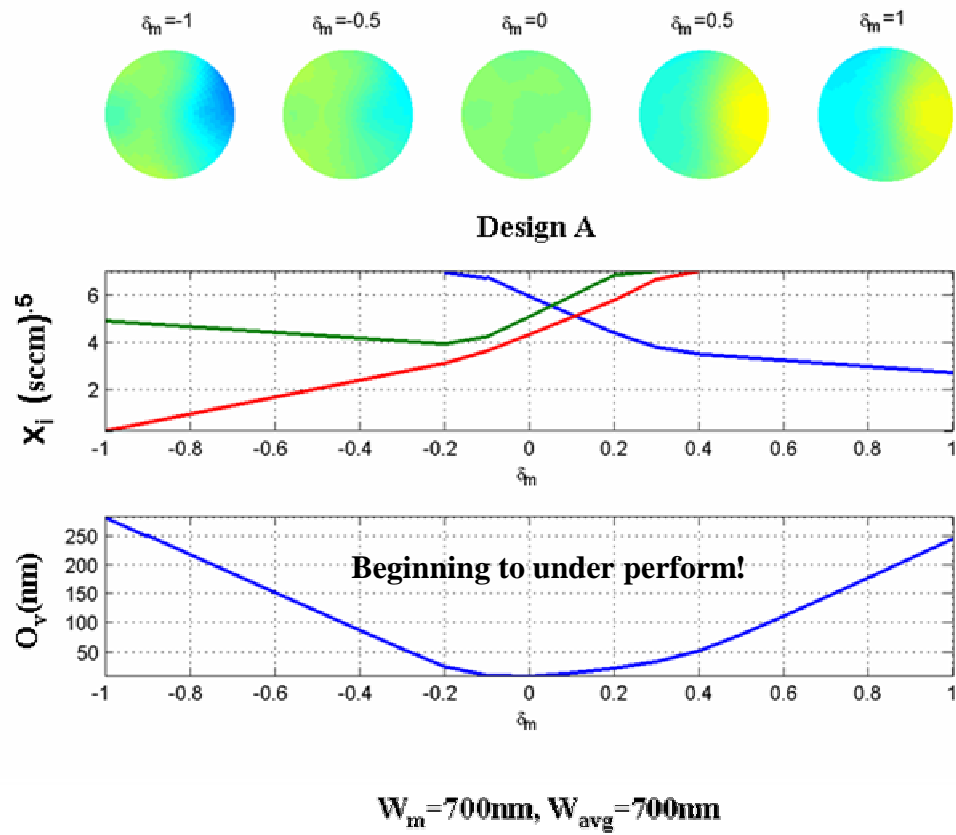


Figure 32: Design A vs. Design B Comparison for $W_m = 700 \text{ nm}$ and $W_{\text{avg}} = 700 \text{ nm}$.

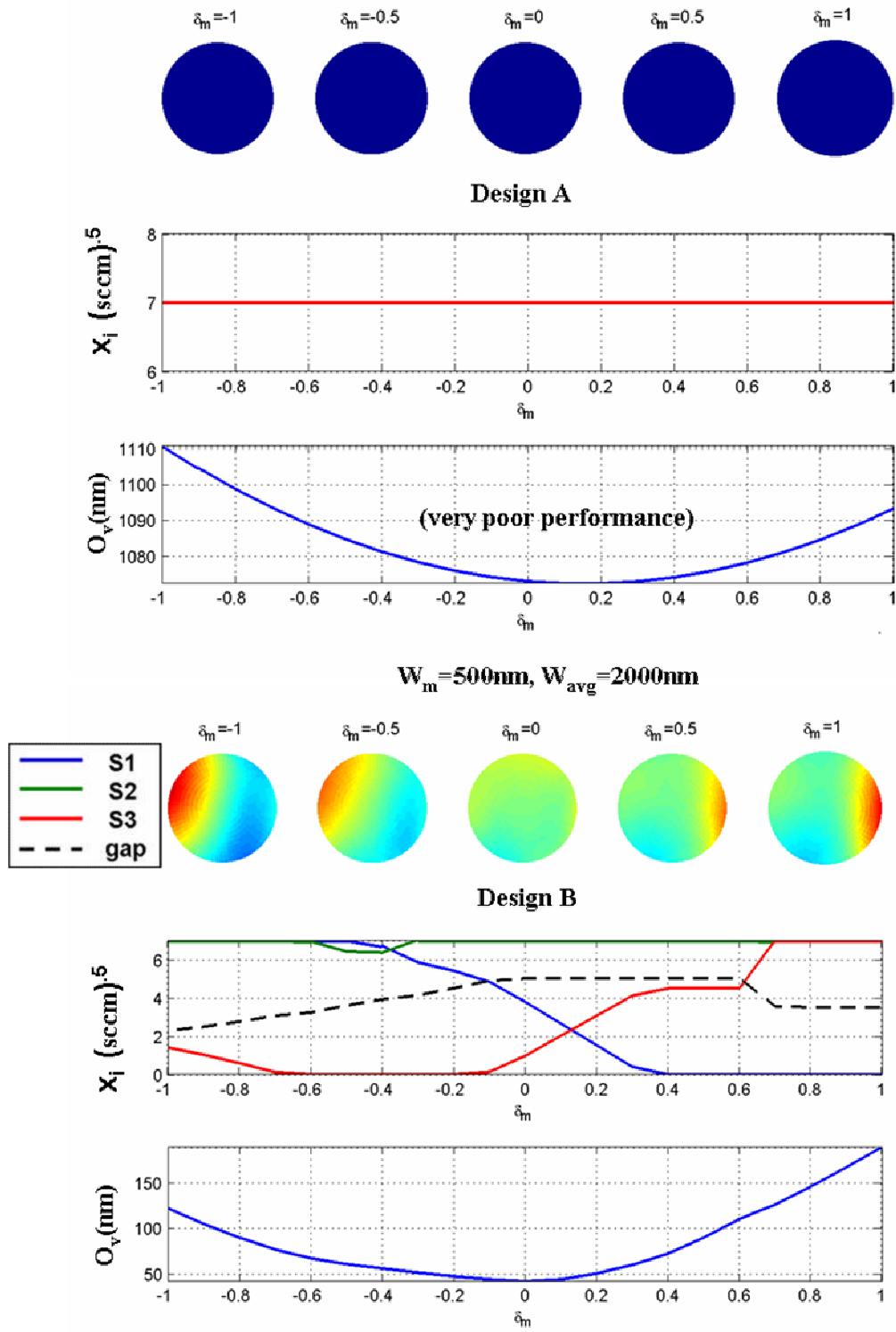


Figure 33: Design A vs. Design B Comparison for $W_m = 500 \text{ nm}$ and $W_{\text{avg}} = 2000 \text{ nm}$.

Design A: will yield poor results as predicted for $W_m=500\text{nm}$, $W_{\text{avg}}=2000\text{nm}$

$W_m=1500\text{nm}$, $W_{\text{avg}}=2000\text{nm}$

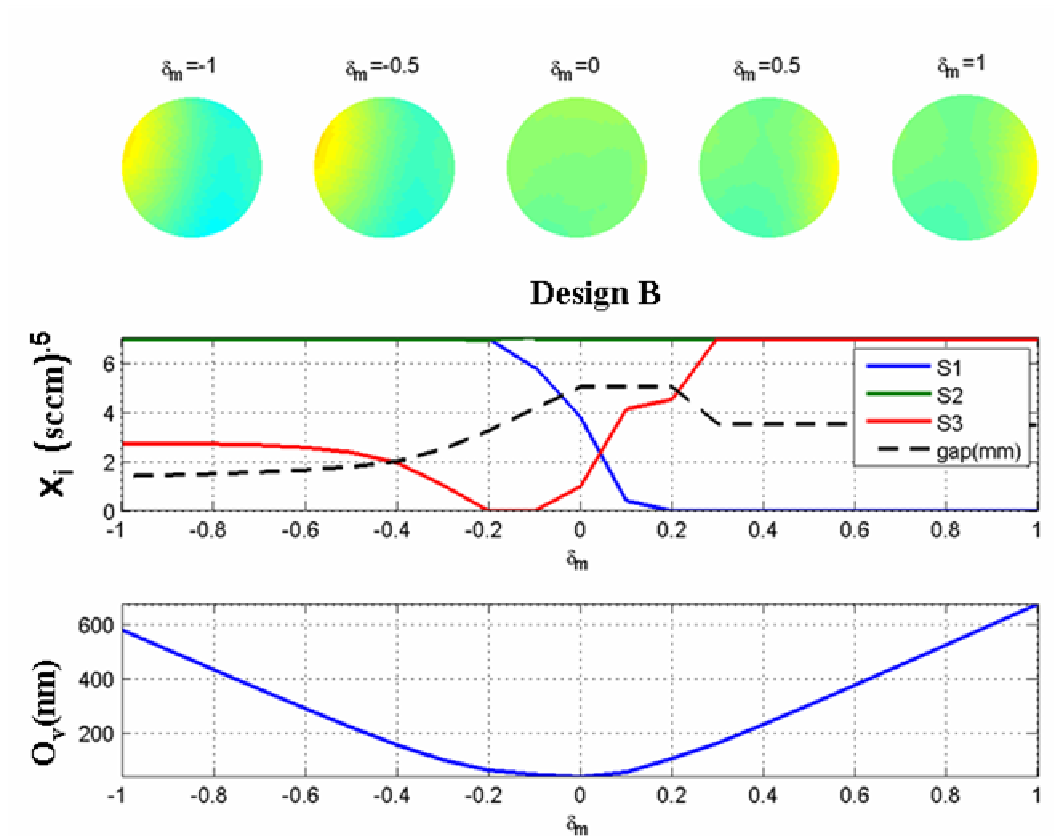


Figure 34: Design A vs. Design B Comparison for $W_m = 1500\text{ nm}$ and $W_{\text{avg}} = 2000\text{ nm}$.

3.7. Chapter summary

The RS modeling approach was used successfully to compare the processing capabilities of two CVD reactor designs and to assess their ability to produce controlled graded films over a sub-section of the wafer surface. The following table compares the merits/demerits of the two designs.

Serial No	Criteria of comparison	Design A	Design B
1	RS Model fidelity reported as $\left \frac{W_{predicted} - W_{measured}}{W_{measured}} \right $	$8 \pm 5\%$	$14 \pm 8\%$
2	Programmability (Uniformity/Non uniformity control)	Good	Good
3	Sensitivity to gap and flow rate	Sensitivity declines rapidly with increasing g	Exhibits good sensitivity with increasing g
4	Range of segment to segment uniformity for the given flow constraints	0-800nm with gaps $0 < g < 3\text{mm}$	0-1800nm with gaps $0 < g < 2.5\text{mm}$
5	Gradient control	Good	Good

Table 5: Design A vs. Design B comparison table

We conclude that design A could be effectively used to deposit uniform and non-uniform films at low gap sizes accurately and with good repeatability. Design B could

be used to deposit thicker uniform and non-uniform films. The gap size could be effectively used as a knob to control intersegment diffusion in the case of design B. ALD films from binary and ternary systems control film composition by adjusting the pulsing and purging frequencies of the individual precursors. Film compositions can be varied from one wafer to the next using this approach. However, deliberate composition gradient control within a single wafer deposition run has not been demonstrated for ALD. We are currently studying reactor designs for combinatorial ALD that enable gas composition gradient control over the wafer surface to deposit varying compositions over a single wafer. Design B, because of its smaller volume and higher conversion rates could prove useful for this purpose.

Chapter 5: Conclusions and Future Work

5.1. Conclusions and inferences:

This research work clearly demonstrated the programmability of the SP-CVD reactor by deliberately producing non-uniform and uniform wafers with a high degree of controllability. In Chapter 2, these modes of operations (non-uniform and uniform) were modeled using a relatively simple linear model. The model was validated and used successfully for predicting thickness profiles for new recipes.

In Chapter 3, two reactor designs were evaluated using RS models. The models were validated and successfully used to evaluate and compare key reactor performance parameters of both designs. The efficacy of simple empirical RS models in predicting reactor performance was demonstrated.

The concept of programmability could itself be extended to all facets of equipment design for which miniaturization of equipment hardware would be a key necessity. We envision the number of segments could be increased to an optimum number with MEMS based mass flow controllers [39] controlling the flow rate of precursor gases from tiny “plug and play” precursor “cartridges” which serve as the gas sources mounted on the top of the showerhead assembly. However, increased programmability and equipment miniaturization must be balanced against the increased complexity of the resulting systems. Having an abundance of spatial control “knobs” in a reactor system is effective only if there are good models relating the manipulated variables to the controlled variables of the system and therein lies the challenge.

5.2. Future work

The next steps for research arising from this work can be categorized as follows:

5.2.1. From an equipment perspective:

- The symmetry of the pumping system could be improved. Currently, the exhaust in the CEV is closer to S1 and S3 giving rise to asymmetry which affects gas flow profiles in the three segments.
- The segments and the mini chamber of Design B are made of Aluminum. This conducts heat away from the wafer surface which reduces wafer temperature and hence conversion rates. These parts could be machined out of Lava or Macor which are non-conducting machinable ceramic materials.
- The heater used to heat the wafer consist of a spirally wound heater coil, which produces temperature non-uniformities. A better ceramic heater would improve temperature uniformity. The downside is that such heaters are very expensive as they have to be custom built for this application.
- The current pressure controller limits the reactor pressure to 1 torr. Using a pressure controller that can enable higher reactor pressures gives more latitude for experimentation and process optimization.
- Next generation showerheads with more segments would render a higher resolution of programmability to the SP-CVD system, although this makes the gas delivery system more complicated. The pros and cons of

developing a showerhead with more segments must be carefully evaluated.

- We are currently studying new showerhead and reactor designs for enabling combinatorial materials research for both CVD and ALD processes.

5.2.2. From a materials perspective:

The W-CVD reactor has been very challenging to work with because the HF generated as a byproduct of the CVD reaction is extremely corrosive and detrimental to fittings, pumps and personnel. Several safety precautions have to be taken. Pumps have to be regularly rebuilt. The HF also corrodes the heater coil which has to be replaced on a monthly basis. For this purpose the vacuum of the reaction chamber has to be broken and the reactor has to be exposed to air for us to access the heater coil and replace it. Also considerable time (~2 weeks) is spent in reactor conditioning times after vacuum is reestablished before good W CVD films can be grown. Also, from a materials perspective W films are well understood. We could consider a material of more interest and which could be deposited (CVD/ALD) using relatively benign precursors and safety requirements.

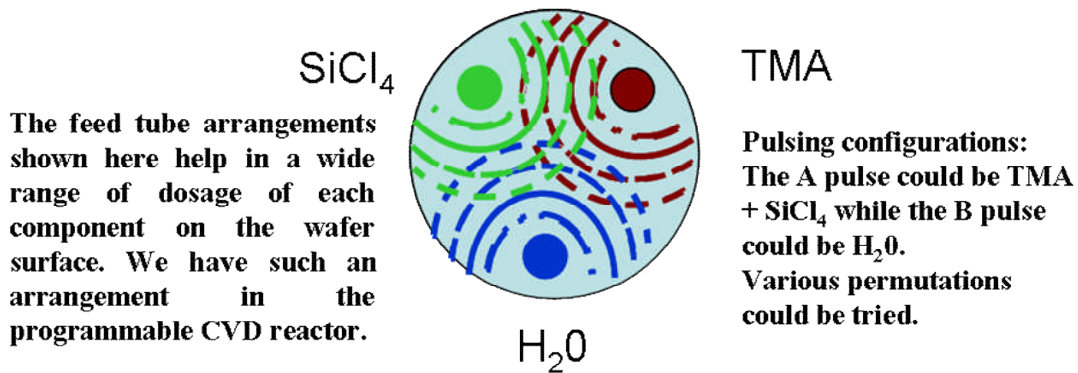
5.2.2. From a process perspective:

In the semiconductor industry as we approach future nodes (45nm and smaller) , the even higher aspect ratios (due to even smaller structures) require methods and new materials to retain and even improve upon the computational performance available at the previous generation ([40], [41]). ALD is a clear choice for thin film deposition at

these nodes. We hope to extend the concept of equipment and process programmability of the SP-CVD reactor to the ALD process also.

Al_2O_3 and SiO_2 ALD are well modeled and understood. Ternary systems like Hafnium Silicate (Hf-Si-O) are very much desired because of their High $-K$ values (for gate oxides, capacitor dielectrics). When a high K oxide is used, the gate dielectric can be made physically thicker, thus lowering the tunneling current. To understand Hafnium Silicate ALD we plan to start our experiments with a chemistry that is well understood and we have identified Al-Si-O (combination of Al_2O_3 and SiO_2 ALD) as a good material system to test and improve upon the combinatorial capabilities of the existing reactor. Figure 35 illustrates this concept.

Low K materials are needed for Inter Layer Dielectric (ILD) applications. ILD material used to electrically separate closely spaced interconnect lines arranged in several levels in a chip; ILD need to have a low dielectric constant k (as close to 1 as possible) to minimize capacitive coupling or what is cross talk between adjacent metal lines.



Precursors

- >TMA for Al_2O_3 (liquid: Use a bubbler and a carrier gas (usually H_2 apart from Ar & N_2))
- > SiCl_4 for SiO_2 (liquid . No carrier gas required)
- >Water (liquid)

Chemistry and reaction conditions:

T, Pressure, flow rates etc

The outcome : A library wafer having a varying Al-Si-O film would be created and could be studied for desired material properties by examining different parts of the same wafer. The appropriate characterization methods have to be identified depending on the property to be measured.

Figure 35: An example of combinatorial ALD

The SP-CVD/ALD system could thus use different precursors in different segments inducing concentration gradients of the precursors over the wafer surface. These gradients could be quantified using spatial sensing capabilities (for example using a mass spectrometer in a multiplexing mode where it samples different areas of the wafer in-situ ([28], [29]) and could be translated through well defined models into surface properties such as thickness, microstructure, or specific electrical properties. The patch of area on the wafer with the most desired property could be identified and the system re-programmed to produce an entire wafer with film having this desired property. Such an approach shortens the product development cycle and reduces material cost. Figure 36a illustrates this concept.

An example of such a study would be a system where W could be deposited by the H_2 reduction of WF_6 as shown in this research work or by SiH_4 reduction of WF_6 . The properties of the W film (grain size, resistivity, growth rate) grown by these two reduction chemistries are different. It would be an interesting exercise to see if the film grown by a combination of these two chemistries would provide a W film with more desirable properties. Figure 36b illustrates this concept.

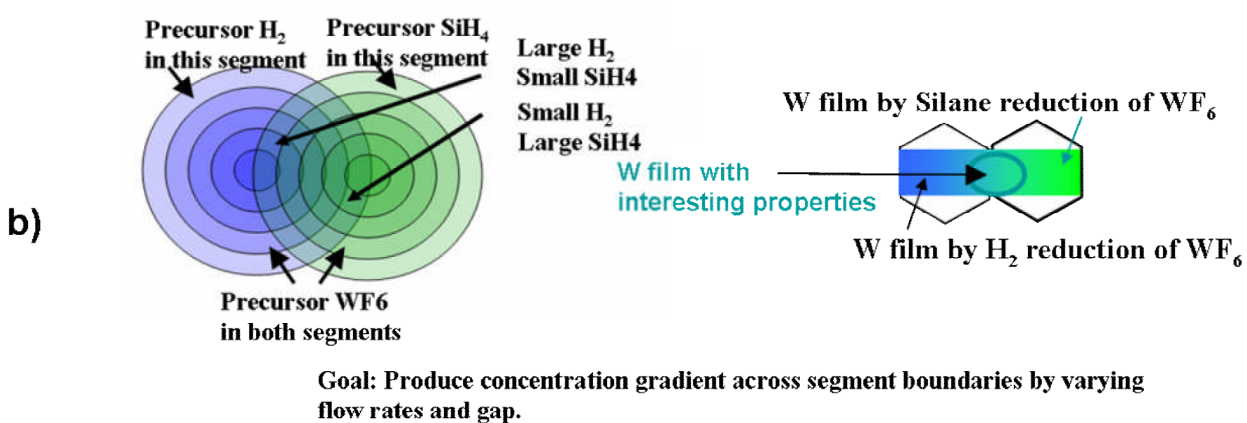
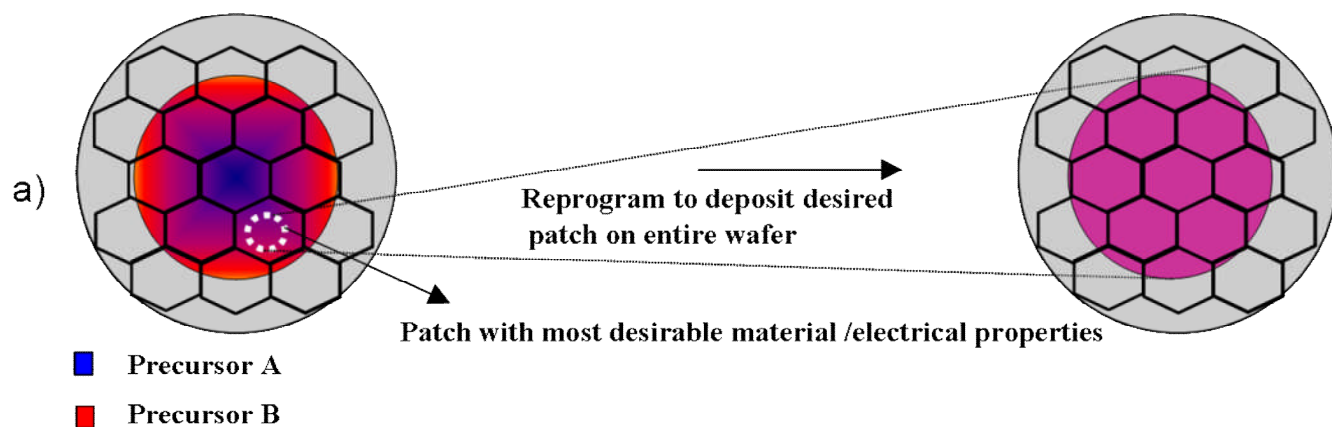


Figure 36: Combinatorial CVD/ALD strategies.

5.2.3. Combinatorial ALD for nano-laminates and nano-composites:

A nano-laminate ([42], [43]) is a thin film composed of a series of alternating sub-layers with different compositions, e.g., Al_2O_3 and Ta_2O_5 . In nano-laminates the advantageous properties of each component can be retained, for example in insulators: high permittivity, low leakage current, high charge storage capacity). The above choice of materials would enable proof of concept of programmable combinatorial ALD. But may not be necessarily the best choice of materials as it is agreed that Hafnium oxide or some form of Hafnium silicate would be the choice for 65 nm nodes and lower.

The world of nano-materials has opened up a wide range of potential applications in the recent decade. The advent and fast paced progress of micro electronics on a solid foundation of quantum mechanics has not only provided us the sophisticated technology that we see being applied everyday but also the insight into the promising world of devices in the nano-scale. Small wavelength high resolution measurement devices aided by the ever increasing computing power of the processors, controllers and data acquisition systems have validated predictive quantum theories of the last century (for e.g. existence of quarks) and paved way for bold research endeavors to explore the nano- world.

One recent revelation is the field of nano-laminate composite materials or nano-composites deposited layer by layer to form a device of technological significance. They represent a new frontier in materials science because composites can have very different properties from their constituents. A nano-laminate (a monolayer of the

constituent nano-composite) exhibits unique physical properties when the thickness of the monolayer (nanolayer) is less than the characteristic length scale that defines the physical property. For example, the thermal conductivity is reduced when the nanolayer thickness is less than the mean free path of the phonon that transfers the heat. Other physical properties that are altered include hardness, optical properties, electrical conductivity, and the crystalline structure to name a few. In the semiconductor industry HfO_2 and ZrO_2 and their associated silicates and aluminates have emerged as leading high-k dielectric candidates to replace SiO_2 . Hence nano-composites which constitute several nanolayers (usually a binary system) of different composites result in thin films having the desired physical properties conducive to the application in mind which would not be possible had the thin film been made out of just one of the constituent composites. This paradigm shift of material property as its dimensions enter the nanoscale is the motivation for research. This interest is further supported by the advent and development of ALD systems which show great promise in the ability to deposit ultra thin films /nano layers in a manufacturing environment. ALD is ideally suited for the deposition of nanocomposite films with a thickness control of $\sim 1\text{\AA}$ of the individual composite layers.

Thin film deposition span a wide range of applications. Some of them are corrosion resistant coatings, nanotubes, nanowires, organic semiconductors, III-V Semiconductors (gate dielectrics), MEMS, NEMS, Photonic Crystals, Porous Media, Filters, Membranes, OLED(Organic LEDs), Solar Cells (passivation and anti reflection coatings), Silicon Microelectronics, DRAM (high-k dielectrics, capacitors), Integrated Optics, Lasers, and Photonics (optical coatings). Nano-composites thus

show a promising potential for the future as devices in the whole gamut of applications shrink in size, and demand greater performance in terms of the physical property (hardness, flexibility, rigidity, conductivity, etc.) most conducive to the application at hand.

This study would entail parallel research in four directions:

- 1) ALD equipment design: (Programmable ALD design at the university of Maryland renders the tool combinatorial capabilities necessary for nano-laminate ALD research)
- 2) Combinatorial approach to experiments and Material Selection: (A combinatorial approach would help in identifying new nano-laminates with an optimized set of experiments). A new library of nano composites could thus be systematically created. Binary and ternary systems could be explored for starters. Identifying the materials depends on the current bottlenecks of the semiconductor industry for e.g.
 - Critical control of the dimensions of the channel and gate length
 - The need for high K gate and capacitor dielectrics as SiO_2 and Al_2O_3 fail to deliver at smaller scales.
 - The search for new Low K dielectric for ILD (inter layer dielectric) as line widths get smaller
 - The search for new barrier materials
 - High conformality films for high aspect ratio structures

Identifying the most suitable precursors would also be a subset of this direction.

- 3) Identifying the physical properties to be measured and the selection of the apt characterization methods.
- 4) Nano scale (atomistic) modeling with reliable predictive capabilities of growth rates and even film properties.

Appendix A: Title of related online videos

The following links are to help readers improve their understanding of the work reported in this thesis. These videos are meant to provide the reader a better visual understanding of the equipment used in this research and guide the new research student to certain useful procedures in vacuum technology. The student is encouraged to improve upon these procedures and capture the improvisation on video and upload the new improved version.

1. <http://www.doflick.com/ViewVideo.aspx?vId=165> (Video of Design B)
2. <http://www.doflick.com/ViewVideo.aspx?vId=166> (Video of a close up of Design B)
3. <http://www.doflick.com/ViewVideo.aspx?vId=248> (Video of substrate heater)
4. <http://www.doflick.com/ViewVideo.aspx?vId=246> (Video of a Linear Motion Device installation procedure)
5. <http://www.doflick.com/ViewVideo.aspx?vId=155> (Video of a simple leak check tutorial for vacuum systems)
6. <http://www.doflick.com/ViewVideo.aspx?vId=181> (Video of a tutorial showing how to tighten a CF flange)
7. <http://www.doflick.com/ViewVideo.aspx?vId=247> (Video of a tutorial on how to replace the filament in an ion gage)
8. <http://www.doflick.com/ViewVideo.aspx?vId=208> (Video demonstrating the use of swage lock for plastic tubes)
9. <http://www.doflick.com/ViewVideo.aspx?vId=245> (Video demonstrating the use of gas feed through for Vacuum chambers)
10. <http://www.doflick.com/ViewVideo.aspx?vId=164> (Video of a tutorial on how to assemble a VCR fitting)
11. <http://www.doflick.com/ViewVideo.aspx?vId=182> (Video of a tutorial on how to replace a gas cylinder)

Bibliography

- [1]. Robert R. Schaller, "Moore's Law: Past ,present and future", IEEE SPECTRUM, June 1997.

- [2]. <http://www.itrs.net/papers.html>

- [3]. Paul S. Peercy, "The drive to miniaturization", Nature **406**, 1023-1026 (2000).

- [4]. R. D. Isaac, "The future of CMOS technology", IBM Journal of Research and Development, 2000, Vol. **44**, No.3, web site: www.research.ibm.com/journal/rd/443/isaac.html

- [5]. <http://www.adventact.com/products/processworks/images/Deployment-of-runtorun.pdf>

- [6]. Gary W. Rubloff, Invited paper, Proc.2003 International Conference on Characterization and Metrology for ULSI Technology, Austin, TX, March 24-28, ed by D. G. Seiler et. al., AIP Conf. Proc.Vol. **683**, 583-591.

- [7]. <http://www.reedlectronics.com/semiconductor/article/CA6410945?nid=2012>

- [8]. <http://computer.howstuffworks.com/dna-computer1.htm>

- [9]. Choo, J. O., Ph.D. Thesis, University of Maryland, 2005

- [10]. Moslehi, M. M, C. J. Davis, and R. T. Matthews, United State Patent 5,453,124 (1995).

- [11]. Van der Stricht, W., I. Moerman, P. Demeester, J. A. Crawley and E. J. Thrush, *J. Crystal Growth* **170**, 344-348 (1997).
- [12]. Yang, C., C. Huang, G. Chi and M. Wu, *J. Crystal Growth* **200**, 39-44 (1998).
- [13]. Theodoropoulos, C., T. J. Mountziaris, H. K. Moffat and J. Han, *J. Crystal Growth* **217**, 65-81 (2000).
- [14]. Parikh, R. P., R. A. Adomaitis, M. E. Aumer, D. Partlow, D. Thomson, and G. W. Rubloff, "J. Crystal Growth accepted for publication (2006).
- [15]. Moslehi, M. M., C. J. Davis, and A. Bowling, *TI Technical Journal*, Sept-Oct, 44-64 (1992).
- [16]. Stuber, J. D., I. Trachtenburg, and T. F. Edgar, *IEEE Trans. Semicond. Manuf.* **11**, 442-457 (1998).
- [17]. Kiether, W. J., M. J. Fordham, S. Yu, A. J. S. Neto, K. A. Conrad, J. Hauser, F.Y. Sorrell, and J. J. Wortman, *Proc. 2nd Int (1994). RTP Conf.*, 96-101.
- [18]. Theodoropoulou, A., E. Zafiriou, and R. A. Adomaitis, *IEEE Trans. Semicond. Manuf.* **12**, 87-101 (1999).
- [19]. Christofides, P. D., Birkhauser Pub.Co. (2001).
- [20]. Banks, H. T., S. C. Beeler, G. M. Kepler, and H. T. Tran, *SIAM J. Appl.Math.* **62**, 1251-1280 (2002).

- [21]. Kepler, G. M., H. T. Tran, and H. T. Banks, *Optim. Contr. Appl. Meth.* **21**, 143-160 (2000).
- [22]. Kepler, G. M., H. T. Tran, and H. T. Banks, *IEEE Tran. Semicond. Manuf.* **14**, 231-241 (2001).
- [23]. U.S. patent 6,821,910 was issued Nov. 23, 2004 to Professors Ray Adomaitis, John Kidder and Gary Rubloff for the invention of the programmable reactor.
- [24]. J. O. Choo, R. A. Adomaitis, G. W. Rubloff, L. Henn-Lecordier, and Y. Liu “Simulation-Based Design and Experimental Evaluation of a Spatially Controllable Chemical Vapor Deposition Reactor”, *AIChE Journal*, February 2005 Vol. **51**, 572-584.
- [25]. J. O. Choo, R. A. Adomaitis, L. Henn-Lecordier, Y. Cai, and G. W. Rubloff “Development of a Spatially Controllable Chemical Vapor Deposition Reactor with Combinatorial Processing Capabilities”, *Review of Scientific Instruments*, **76** (2005).
- [26]. R. Kleijn, C. J. Hoogendoorn, A. Hasper, J. Holleman and J. Middelhoek, “Transport phenomena in tungsten LPCVD in a single-wafer reactor”, *Journal of the Electrochemical Society*, **138**, 509(1991).
- [27]. R. Kleijn and C. Werner, *Modeling of chemical vapor deposition of tungsten films*, Basel; Boston: Birkhäuser Verlag, 1993.
- [28]. T. Gougousi, R. Sreenivasan, Y. Xu, L. Henn-Lecordier, J.N. Kidder., G. W. Rubloff, and E. Zafiriou, “In-situ Sensing using Mass-Spectrometry and its use for Run-to-Run Control on a W CVD Cluster Tool”,

Characterization and Metrology for ULSI Technology: 2000 International Conference, Gaithersburg, MD, 26-29 June 2000, AIP Conference Proceedings, Melville, NY, 2001, vol. **550**, pp. 249-253.

- [29]. Y. Cai, R. Sreenivasan, J. O. Choo, R. A. Adomaitis, G. W. Rubloff, "Multiplexed Mass Spectrometric Sensing in a Spatially Programmable Chemical Vapor Deposition Reactor", to be submitted to JVST, 2005.
- [30]. Adomaitis, R. A., *Computers & Chem. Eng* (2002) **26**, 981-998.
- [31]. Parikh, R. P., R. A. Adomaitis, J. D. Oliver, and B. H. Ponczak, *J. Process Control* (2006). Available online (July 2006).
- [32]. R. C. Smith, N. Hoilien, J. Roberts, S. A. Campbell, and W. L. Gladfelter, Combinatorial chemical vapor deposition of metal dioxides using anhydrous metal nitrates, *Chem. Mater.* (2002) **14**, 474-476.
- [33]. B. Xia, R. C. Smith, T. L. Moersch, and W. L. Gladfelter, Balancing reactor fluid dynamics and deposition kinetics to achieve compositional variation in combinatorial chemical vapor depositions, *Appl. Surf. Sci.* (2004) **223**, 14-19.
- [34]. Q. Wang, J. Perkins, H. M. Branz, J. Alleman, C. Duncan, and D. Ginley, Combinatorial synthesis of solid state electronic materials for renewable energy applications, *Appl. Surf. Sci.* (2002) **189**, 271-276.
- [35]. Q. Wang, Combinatorial hot-wire CVD approach to exploring thin-film Si materials and devices, *Thin Solid Films*, (2003) **430**, 78-82.

- [36]. Q. Wang, F. Liu, and D. Han, High-throughput chemical vapor deposition system and thin-film silicon library, *Macromol. Rapid Commun.* (2004) **25**, 326-329.
- [37]. C. J. Taylor and S. Semancik, Use of microhotplate arrays as microdeposition substrates for materials exploration, *Chem. Mater.* (2002) **14**, 1671-1677.
- [38]. R. Sreenivasan, R. A. Adomaitis, G. W. Rubloff, *J. Vac. Sci. Technol.* (2006) B **24**, 2706.
- [39]. <http://www.redwoodmicro.com/>
- [40]. Hand, A., "Industry Begins to Embrace ALD", *Semiconductor International* 2003.
- [41]. Osborne, M., "Critical Component requirements for ALD technology" *Semiconductor Fabtech*, 21st edition, website :
<http://www.uct.com/products/publications.html>
- [42]. J.W. Elam, Z.A. Sechrist and S.M. George, "ZnO/Al₂O₃ Nanolaminates Fabricated by Atomic Layer Deposition: Growth and Surface Roughness Measurements", *Thin Solid Films* **414**, 43-55 (2002).
- [43]. <http://www.colorado.edu/chem/DEC/people/georges.html>